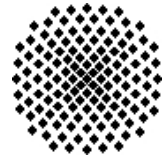


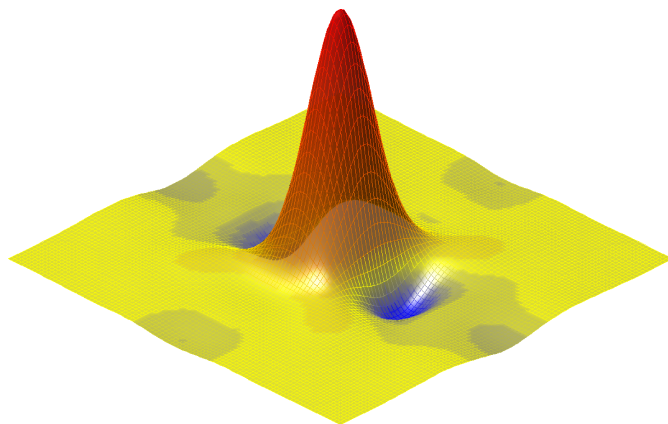
Universität Stuttgart

Geodätisches Institut



---

# Applying stochastic constraints on time-variable GRACE data



Diplomarbeit im Studiengang  
**Geodäsie und Geoinformatik**  
an der Universität Stuttgart

Christof Lorenz

Stuttgart, Januar 2009

---

**Betreuer:** Prof. Dr.-Ing. Nico Sneeuw  
Universität Stuttgart

M. Sc. Balaji Devaraju  
Universität Stuttgart



---

# **Selbstständigkeitserklärung**

Hiermit erkläre ich, Christof Lorenz, dass ich die von mir eingereichte Diplomarbeit zum Thema

## **Applying stochastic constraints on time-variable GRACE data**

selbstständig verfasst und ausschließlich die angegebenen Hilfsmittel und Quellen verwendet habe.

Datum, Ort: \_\_\_\_\_

Unterschrift: \_\_\_\_\_  
(Christof Lorenz)



---

# Abstract

Since its launch in the year 2002, the space satellite mission GRACE provides spherical harmonic coefficients, which can be used to observe the time-variable part of the Earth's gravity field. It was initially assumed that the derived gravitational quantities from these coefficients are of high accuracy and would thus deliver reliable large scale mass estimates. However, the provided coefficients of higher harmonic degree and order turned out to be seriously contaminated with noise, yielding an unrealistic signal of mass variations in form of massive north-south stripes.

In this work, two methods are investigated, which add stochastic constraints to time-variable GRACE coefficients. It is assumed that these techniques are able to reduce the noise level in the monthly datasets by assimilating the GRACE coefficients with more reliable data. Both approaches need prior estimates of a signal and error covariances. Hence, the signal covariance of the time-variable gravity field is assumed to be of isotropic nature and is thus computed as a Kaula-type power law, which is fit into the part where the signal degree variances of the GRACE solutions linearly attenuate. The error covariance is estimated according to the energy balance approach which allows the simulation of a fully populated GRACE covariance matrix.

Stochastic constraining in the spectral domain combines both signal and error covariance estimates in a Bayesian type regularization procedure, which constrains the monthly GRACE solutions with the modelled signal covariance. It is shown that Bayesian type regularization can be used to build a spectral filter kernel. Furthermore, the weight between both GRACE coefficients and the regularization term is estimated by a variance component estimation. Tests with a full, block diagonal and diagonal covariance matrix are performed, as it is widely believed that full covariance information can be sufficiently approximated by a block diagonal matrix. Furthermore, the Bayesian type regularization filter is tested with three different monthly GRACE solutions and compared with other widely used filtering techniques.

The second approach constrains the time-variable GRACE coefficients with hydrological observations, which are provided as monthly precipitation and run-off values on basin scale. Both the GRACE and hydrological observation group are assimilated in one linear model, which is solved by sequential least squares estimation, yielding an agreement between mass estimates from GRACE and observed hydrology.

**Keywords:** Sequential estimation, time-variable gravity field, Bayesian type regularization, hydrological constraints, stochastic filters



---

# Zusammenfassung

Seit ihrem Start im Jahr 2002 liefert die Satellitenmission GRACE Kugelfunktionskoeffizienten, welche zur Untersuchung des zeit-variablen Anteils des Schwerefeldes der Erde genutzt werden können. Ursprünglich wurde angenommen, dass die von solchen Koeffizienten abgeleiteten Schweregrößen hochgenau sind und somit verlässliche grossflächige Masseschätzungen erlauben. Jedoch stellte sich heraus, dass vor allem die Koeffizienten höheren Grades und höherer Ordnung einen hohen Rauschanteil aufweisen, welcher sich in einem unrealistischem Signal der Massevariationen in Form von Nord-Süd-Streifen äußert.

Diese Arbeit beschreibt zwei Methoden, welche die zeit-variablen GRACE-Koeffizienten mit stochastischen Bedingungsgleichungen kombinieren. Es wird angenommen, dass diese Techniken den Rauschanteil in den monatlichen Datensätzen durch Angleichung mit genauerem Datenmaterial reduzieren können. Beide Ansätze benötigen vorausgehende Informationen über die Signal- und Fehler-Kovarianzen. Daher wird hier angenommen, dass die Signal-Kovarianz des zeit-variablen Schwerefeldes isotrop ist und somit als eine Art Kaula'sches Potenzgesetz berechnet werden kann, welches in linear abnehmende Gradvarianzen des Signals der GRACE-Koeffizienten geschätzt wird. Die Fehler-Kovarianz ergibt sich anhand des *energy balance approach* berechnet, der die Simulation einer voll besetzten Kovarianzmatrix ermöglicht.

Das Hinzuziehen von stochastischen Bedingungsgleichungen im Frequenzbereich kombiniert Signal- und Fehler-Kovarianzen in einer Bayes'schen Regularisierung, welche die modelliere Signal-Kovarianz als Bedingungsgleichung hinzuzieht. Es wird gezeigt, dass die Bayes'sche Regularisierung als spektraler Filter verwendet werden kann. Das Gewicht zwischen den GRACE Koeffizienten und dem Regularisierungsterm wird durch eine Varianzkomponentenschätzung bestimmt. Es werden Tests mit einer vollen, block-diagonalen und diagonalen Fehlermatrix durchgeführt, da allgemein angenommen wird, dass eine voll besetzte Kovarianzmatrix ausreichend durch eine Block-Diagonalmatrix genähert werden kann. Des Weiteren wird der Bayes'sche Regularisierungsfilter mit drei weiteren Monatslösungen von GRACE getestet und mit anderen weit verbreiteten Filtern verglichen.

Der zweite Ansatz benutzt Beobachtungen von monatlichen Niederschlags- und Oberflächenabflusswerten als zusätzliche hydrologische Bedingungsgleichungen. Sowohl die GRACE-Koeffizienten als auch die hydrologischen Beobachtungen werden in einem linearen Modell zusammengeführt, welches durch eine sequentielle Kleinste-Quadrat-Ausgleichung gelöst wird. Dadurch wird eine Übereinstimmung zwischen Masseschätzungen von GRACE und den hydrologischen Beobachtungen erzwungen.

**Schlüsselwörter:** Sequentielle Ausgleichung, zeit-variables Schwerefeld, Bayes'sche Regularisierung, hydrologische Bedingungsgleichungen, Stochastische Filter



---

# Contents

<b>1</b>	<b>Introduction</b>	<b>1</b>
<b>2</b>	<b>GRACE and time-variable gravity</b>	<b>5</b>
2.1	The Gravity Recovery And Climate Experiment . . . . .	5
2.2	Computation of time-variable GRACE coefficients and their connection to derived mass variations . . . . .	6
2.2.1	Relation between the geoid shape and mass variations . . . . .	6
2.2.2	Numerical differentiation of gravitational quantities . . . . .	8
2.3	The unfiltered GRACE monthly solutions . . . . .	10
<b>3</b>	<b>Stochastic and deterministic filtering of time-variable GRACE data</b>	<b>13</b>
3.1	Spatial averaging: 2-D convolution on a sphere . . . . .	13
3.2	Deterministic averaging . . . . .	15
3.2.1	The isotropic and anisotropic Gaussian filter . . . . .	15
3.2.2	The correlated error filter . . . . .	18
3.3	Stochastic averaging . . . . .	20
3.3.1	The Wiener filter . . . . .	20
3.3.2	The Bayesian type regularization as a spectral filter . . . . .	22
<b>4</b>	<b>Constraining GRACE coefficients with a Kaula-type rule</b>	<b>29</b>
4.1	Estimation of a Kaula rule for time-variable gravity . . . . .	29
4.2	Simulation of a full covariance matrix for time-variable GRACE coefficients	33
4.3	Using a Kaula-type rule as stochastic constraint in a sequential estimation	35
4.4	The efficiency of the regularization with estimated weight factors . . . . .	38
4.4.1	The impact of different power laws as stochastic constraints . . . . .	38
4.4.2	The regularization filter with different covariance matrix struc- tures of the GRACE solutions . . . . .	45
4.4.3	Regularization of different monthly GRACE solutions . . . . .	52
<b>5</b>	<b>Comparison of stochastic and deterministic averaging operators</b>	<b>57</b>
5.1	Filtering performance in the spectral domain . . . . .	57
5.2	Filtering performance in the spatial domain . . . . .	60
5.3	Comparison with modeled and observed hydrology . . . . .	62
<b>6</b>	<b>Constraining monthly GRACE solutions with hydrological mass estimates</b>	<b>69</b>
6.1	Continental hydrology and GRACE . . . . .	69
6.2	Assimilating the GRACE solutions with hydrological mass estimates . . . . .	75
6.2.1	A linear model for the hydrologic constraints . . . . .	75
6.2.2	Combination of hydrologic storage changes and GRACE solutions	76
6.2.3	Sequential estimation and variance component estimation . . . . .	77
6.3	Numerical experiments . . . . .	79

---

<b>7 Summary and outlook</b>	<b>93</b>
<b>Bibliography</b>	<b>96</b>
<b>A Mathematical description of the geoid</b>	<b>101</b>
<b>B Error propagation</b>	<b>107</b>
<b>C Methods for a spherical harmonic error analysis</b>	<b>109</b>
C.1 Eigenvalue analysis for measuring ill-possessness . . . . .	109
C.2 Spectral error analysis . . . . .	110
C.2.1 Absolute Error Measures . . . . .	110
C.2.2 Relative Error Measures . . . . .	110
C.2.3 Redundancy Contribution . . . . .	111
<b>D List of MATLAB programs and output data</b>	<b>113</b>

---

# List of Figures

1.1	Spatial and temporal resolution of CHAMP, GRACE and GOCE . . . . .	2
2.1	Signal and error degree variances of unfiltered GRACE coefficients . . . . .	11
2.2	Derived maps from unfiltered GRACE coefficients . . . . .	11
3.1	Spectral averaging coefficients of the isotropic and anisotropic Gaussian filter . . . . .	17
3.2	Derived maps from Gaussian filtered GRACE coefficients . . . . .	18
3.3	Derived maps from decorrelated error filtered GRACE coefficients . . . . .	19
3.4	Kernel of the decorrelated error filter, propagated to the spatial domain .	19
4.1	Power laws of different data series . . . . .	31
4.2	Comparison of different approximation methods of power laws . . . . .	32
4.3	Simulated full covariance matrix for time-variable GRACE coefficients . .	34
4.4	Degree variances of regularized GRACE coefficients . . . . .	36
4.5	Spectral redundancy contribution of a regularization matrix . . . . .	37
4.6	Derived maps from regularized GRACE coefficients . . . . .	38
4.7	Regularization parameter after each iteration for different regularization terms . . . . .	40
4.8	Comparison of regularized signal and error variances with and without estimated variance components . . . . .	40
4.9	Signal, noise and modelled degree variances of regularized GRACE coefficients	41
4.10	Spectral redundancy contribution of the regularization matrix with estimated variance components . . . . .	42
4.11	GRACE coefficients before and after regularization . . . . .	42
4.12	Derived maps from regularized GRACE coefficients, using VCE . . . . .	44
4.13	Spatial difference between weighted and unweighted regularization . . .	45
4.14	Covariance matrix of the cos-coefficients with $l, m = 0, 1, 2, \dots, 21$ . . . . .	46
4.15	Regularization parameter after each iteration for different covariance matrix structures . . . . .	46
4.16	Spectral redundancy contribution of the regularization matrix, using different covariance matrix structures of GRACE coefficients . . . . .	47
4.17	Signal and error degree variances of regularized GRACE solution, using different covariance matrix structures . . . . .	47
4.18	Cross section of the regularization kernel . . . . .	48
4.19	Propagated regularization filter kernel . . . . .	49
4.20	Derived maps from regularized solutions, using different covariance matrix structures . . . . .	51
4.21	Spectral redundancy contribution of the regularization term, using GRACE data from different months . . . . .	53
4.22	Degree variances for different regularized monthly GRACE solutions . . .	53

---

4.23	Propagated regularization filter kernels from different monthly GRACE solutions . . . . .	54
4.24	Cross sections of the regularization kernel, computed from different monthly GRACE solutions . . . . .	55
4.25	Derived maps from different regularized monthly GRACE solutions . . . . .	56
5.1	Degree RMS of different spectral filter operators . . . . .	58
5.2	Filtered GRACE coefficients for January 2003 . . . . .	59
5.3	Degree variances of filtered monthly GRACE solutions . . . . .	60
5.4	Cross sections of different filter kernels . . . . .	61
5.5	Propagated filter kernels . . . . .	62
5.6	Mass variations derived from GLDAS and filtered GRACE coefficients . . . . .	64
5.7	Catchments for validation of the filtered fields with the GLDAS . . . . .	66
5.8	Catchments for validation of the filtered fields with observed hydrology . . . . .	67
6.1	Hydrologic cycle (source: <a href="http://www.ucmp.berkeley.edu">http://www.ucmp.berkeley.edu</a> ) . . . . .	70
6.2	Precipitation and run-off of selected catchments . . . . .	73
6.3	Catchments with negligible evapotranspiration during January 2003 . . . . .	73
6.4	Eigenvalues of the constrained and unconstrained normal matrices . . . . .	80
6.5	Degree variance before and after constraining GRACE solutions . . . . .	82
6.6	Spectral redundancy contribution of the hydrologic constraints . . . . .	83
6.7	Constrained and unconstrained spherical harmonic coefficients . . . . .	83
6.8	Propagated redundancy contribution of the hydrologic constraints . . . . .	84
6.9	Derived maps from constrained and unconstrained GRACE coefficients . . . . .	85
6.10	Propagated errors of the constrained GRACE coefficients . . . . .	87
6.11	Estimated storage changes in water equivalent heights per month . . . . .	88
6.12	Catchments which are removed for cross validation . . . . .	89
6.13	Derived maps from constrained monthly GRACE solutions with varying constraining catchments . . . . .	90
6.14	Differences between the derived maps in figure 6.13 . . . . .	91
6.15	Estimated storage changes in water equivalent heights per month . . . . .	92
A.1	zonal, sectorial and tesseral surface spherical harmonics . . . . .	102
C.1	Triangular scheme of spherical harmonic coefficients . . . . .	110

# Introduction | 1

Since the year 2000, a new generation of space satellite missions like CHAMP (CHAllenging MISSION Payload), GRACE (Gravity Recovery And Climate Rxperiment) and GOCE (Gravity field and steady-state Ocean Circulation Explorer) allow observations of the earth's gravity field with unprecedented spatial and temporal resolution. Thereafter, the data, delivered by the satellites, became the focus of many scientific tasks, e.g. climatology, oceanography and hydrology, as it allows the study of time dependent changes in the dynamic system of the Earth. Such changes are mainly caused by large scale mass relocations in the hydrosphere, which extends about 15 km up into the atmosphere and about 1 km down into the lithosphere, the crust of the earth (Chow et al., 1988). Some of the origins of these changes and their spatial dimension are summarized in figure 1.1, where their possible detection is assigned to the three satellite missions CHAMP, GRACE and GOCE.

It is shown, that GRACE delivers the highest temporal resolution and is thus able to observe monthly mass variations with a spatial resolution of less than 1000 km. Besides variations in the atmosphere, oceans and land masses, such effects mainly come from hydrological phenomena like changes in the groundwater, soil moisture or changes in large scale continental water basins. In (Wahr et al., 1998) it was predicted that GRACE would be able to measure these effects with an accuracy of about 2 mm of water equivalent heights.

Unfortunately, the initially considered accuracy could not yet be achieved for the time-variable gravity field (Wahr et al., 2004), which is due to a very high noise content in the coefficients of short-wavelength, delivered by GRACE. Thus, it is essential to apply certain filtering techniques. But it is a matter of common knowledge, that filtering not only reduces the noise content, but good signal as well. This is especially the case for so called *deterministic* averaging operators, which smooth the gravity field without consideration of the signal itself. Such filters are widely used to smooth the derived quantities from GRACE solutions.

Since the launch of these new space gravity missions, modern tailor-made filters for smoothing gravitational satellite data were presented (e.g. Han et al., 2005; Swenson & Wahr, 2006; Sasgen et al., 2006; Kusche, 2007), which take e.g. the errors of the signal into account or use information about correlations in the spectral domain in

order to reduce the noise level in the output signal. The filtering process mainly happens by constraining the noisy signal to tend to a desired output signal, which can be done in the spatial or the spectral domain.

In this work, two methods will be discussed, which add stochastic constraints in form of *a priori* information to time-variable GRACE solutions, based on a desired output signal in the spectral and the spatial domain. In the first case, the spectrum of GRACE data is constrained with fundamental characteristics of spherical harmonic coefficients, which are mainly based on the well known Kaula's rule. A similar approach was already investigated in (Kusche, 2007), where the constraints are based on geophysical models. This work will discuss an alternative, which uses GRACE-data only to reduce the noise-content in the GRACE coefficients.

The second approach is based on the fact, that even after filtering, mass estimates from GRACE show differences to observed values. As such observed data is obviously more reliable than some mathematical models, the second method tries to constrain the GRACE-coefficients with hydrological observations, yielding an output signal, which is not only consistent with models, but with observed hydrological data as well.

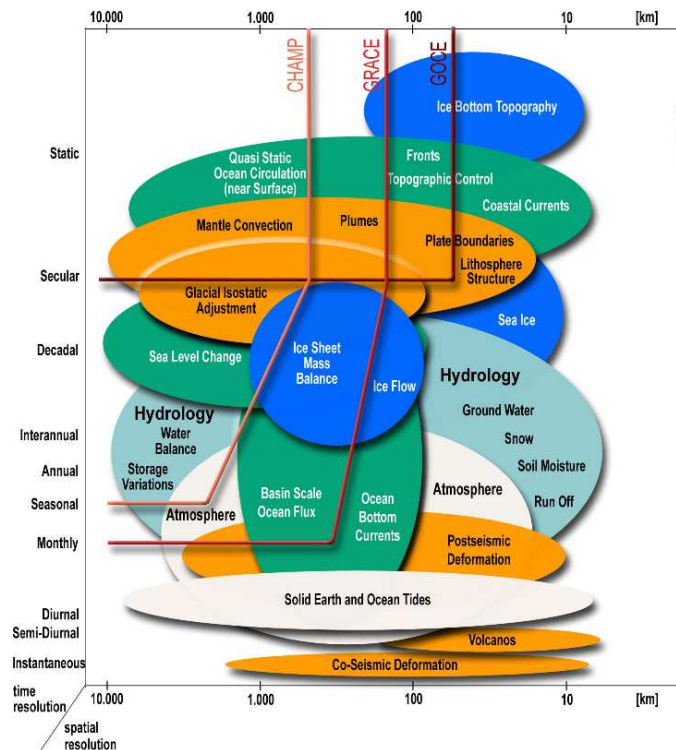


**Figure 1.1:** Temporal and spatial scales of geoid signals associated to solid Earth (orange), ocean (green) , ice (dark blue) and continental hydrology (light blue) processes. The red lines show the spatial and temporal resolution limits of the CHAMP, GRACE and GOCE missions (Flury & Rummel, 2004).

This work is divided into the following sections:

- Chapter 2 contains a short review of the space gravity mission GRACE and discusses the relationship between gravity and surface mass. Additionally, the problems of monthly unfiltered GRACE coefficients are discussed.
- In chapter 3, an overview and a short analysis of modern spherical harmonic filtering techniques is presented, which consists of the Gaussian, Wiener and decorrelated error filter. Additionally, a method which is frequently used for stabilizing ill-posed systems of normal equations, the regularization, and its application to filtering spherical harmonic coefficients is derived.
- Chapter 4 discusses the estimation of a signal variance model from monthly GRACE solutions, which is needed for the stochastic filters. Additionally, as these filters allow the consideration of a full covariance matrix, a method to simulate such a matrix for GRACE coefficients is presented. Afterwards, the signal variance model and the simulated covariance matrix is used as input in the regularization. The chapter will further discuss the impact of different covariance matrix structures as well as the time-dependency of the presented regularization filter.
- In chapter 5, the regularization filter is compared with the other discussed filters from chapter 3. Therefore, the filtering performance is analyzed in the spectral and spatial domain. Additionally, the filtered GRACE solutions are validated with observed and modeled hydrological data.
- In chapter 6 the method of assimilating monthly GRACE solutions with observed hydrological data is discussed, which can be seen as spatially constraining the GRACE coefficients. This approach is tested with unfiltered and regularized GRACE-coefficients and the results are analyzed in the spatial and spectral domain.
- Chapter 7 provides a brief summary and highlights the important results of this thesis. It also talks about the possible extensions to this work in the future.



## 2.1 The Gravity Recovery And Climate Experiment

The Gravity Recovery And climate Experiment (GRACE) satellite mission was launched on the 17<sup>th</sup> of March in 2002 as a joint partnership between the National Aeronautics and Space Administration (NASA) and the Deutsches Zentrum für Luft- und Raumfahrt (DLR). Furthermore, it is the second mission under the NASA Earth System Science Pathfinder (ESSP) program. The mission was originally intended to last for five years, but is still in orbit.

The space segment consists of two identical satellites, which are fundamentally based on the CHAMP satellite. These two satellites fly about 220 km apart in a near circular, near porlar orbit ( $i = 89^\circ$ ) with an altitude of about 500 km. Both satellites are equipped with a high-accuracy K-band distance measuring unit, yielding a low-low satellite-to-satellite tracking constellation. This system detects the distance between the satellites with an accuracy of about  $1 \mu\text{m}$ . The absolute position, altitude and orientation of each space-craft is determined by a GPS-receiver and a twin star camera, whereas non-gravitational accelerations are detected by a precise accelerometer and can thus be removed from the integral sum of the observed gravity yielding a signal that is dominated by the Earth's gravity field.

As variations in the gravity field impacts on both satellites at different times, such deviations cause a change in the inter-satellite range, which is measured with very high accuracy from the K-band measurement unit. The measured inter-satellite range can be transformed into changes in the Earth's gravity field (Han, 2003), which is described with the Stokes coefficients  $\tilde{C}_{lm}$  and  $\tilde{S}_{lm}$ .

The virtue of the GRACE satellites is the temporal resolution, as every 30 days a complete set of such coefficients is delivered which can be used to estimate a model of the geoid. Initially, it was assumed that the gravity field estimates from GRACE would have a spatial resolution of about 150 km of half wavelength with a maximal degree of expansion being  $l_{\max} = 120$  (Reigber et al., 2002). This was truly realized in e.g. (Mayer-Gurr, 2007), where a static gravity field model was computed until degree and order 180 from 57 monthly GRACE solutions. On the other hand, the time variable part used only spherical harmonic coefficients up to degree and order 40.

The GRACE coefficients can be obtained from four different institutes: the Geo Forschungs Zentrum (GFZ) in Potsdam, Germany, the Center of Space Research (CSR) in Austin, Texas, the Centre National D'Etudes Spatiales (CNES) in Toulouse, France and the Jet Propulsion Laboratory (JPL) in Pasadena, California. A detailed discussion about the differences between the monthly solutions is given in e.g. (Zenner, 2006). In this thesis, all computations were done with the fourth release of the GRACE coefficients from the CSR. In agreement with the computations which were done by the CSR (Bettadpur, 2007), the degree 0 and degree 1 coefficients were removed during the following computations.

## 2.2 Computation of time-variable GRACE coefficients and their connection to derived mass variations

### 2.2.1 Relation between the geoid shape and mass variations

The shape of the geoid, i.e. the distance between the reference ellipsoid and the geoid surface  $N$ , can be expanded in a sum of spherical harmonics:

$$N(\theta, \lambda) = R \sum_{l=0}^{\infty} \sum_{m=0}^l \tilde{P}_{lm}(\cos \theta) (\tilde{C}_{lm} \cos m\lambda + \tilde{S}_{lm} \sin m\lambda) \quad (2.2.1)$$

where

$N(\theta, \lambda)$	geoid height at a point with the spherical coordinates $(\theta, \lambda)$
$R$	radius of the Earth (i.e. 6378.137 km)
$\tilde{P}_{lm}$	normalized associated Legendre functions of degree $l$ and order $m$
$\tilde{C}_{lm}, \tilde{S}_{lm}$	normalized Stokes coefficients

As the only time-variable parameters in the upper equation are the spherical harmonic coefficients  $\tilde{C}_{lm}$  and  $\tilde{S}_{lm}$ , a time-dependent change in the geoid heights  $\Delta N$  is reflected by a difference between these coefficients. This difference can be obtained by subtracting two sets of coefficients from different dates to determine e.g. a change in the geoid heights over a certain period, by subtracting one set from a temporal mean or by forming any other reasonable kind of difference. One has to keep in mind that this only expresses the difference of the geoid heights between two points in time. Thus, it actually gives no information about the rate, with which these variations happen. In either case, equation (2.2.1) then reads as

$$\Delta N(\theta, \lambda; t) = R \sum_{l=0}^{\infty} \sum_{m=0}^l \tilde{P}_{lm}(\cos \theta) (\Delta \tilde{C}_{lm}(t) \cos m\lambda + \Delta \tilde{S}_{lm}(t) \sin m\lambda) \quad (2.2.2)$$

By assuming that  $\Delta N(\theta, \lambda; t) \neq 0$ , it becomes clear that there had to be a change in the Earth's gravity field. Such a change is caused by mass fluctuations in, on and above the Earth's surface and is thus denoted as a change in the Earth's density distribution  $\Delta \rho(r, \theta, \lambda, t)$ . Wahr et al. (1998) found a connection between this quantity and its representation in the spherical harmonic coefficients  $\tilde{C}_{lm}$  and  $\tilde{S}_{lm}$ :

$$\begin{aligned} \left\{ \frac{\Delta \tilde{C}_{lm}(t)}{\Delta \tilde{S}_{lm}(t)} \right\} &= \frac{3}{4\pi R \rho_{\text{ave}} (2l+1)} \int \int \Delta \rho(r, \theta, \lambda; t) \tilde{P}_{lm}(\cos \theta) \\ &\times \left( \frac{r}{R} \right)^{l+2} \left\{ \begin{array}{l} \cos m\lambda \\ \sin m\lambda \end{array} \right\} \sin \theta d\theta d\lambda \end{aligned} \quad (2.2.3)$$

where  $r$  is the distance of the computation point from the center of the Earth and  $\rho_{\text{ave}}$  is the average density of the Earth (i.e. 5.515 g/cm<sup>3</sup>). However, an accurate determination of  $\Delta\rho(r, \theta, \lambda; t)$  is nearly impossible, as it requires prior knowledge about the inner density distribution of the Earth. But on the other hand, all short-periodic mass variations, which might be detectable by the GRACE satellites, can be assumed to happen only in a thin layer, which is located on the Earth's surface. This layer has to be thick enough to include those portions of the atmosphere, oceans, ice caps, and groundwater storage with significant mass fluctuations. Thus the thickness is mostly determined by the thickness of the atmosphere and is of the order of 10–15 km (Wahr et al., 1998). Moreover, this thin-layer assumption allows one to obtain surface mass changes from geoid changes and vice versa.

The change in the so called *surface density*  $\Delta\rho_S$  is defined as the radial integral of  $\Delta\rho$  through this layer:

$$\Delta\rho_S(\theta, \lambda; t) = \int_{\text{thin layer}} \Delta\rho(r, \theta, \lambda; t) dr \quad (2.2.4)$$

As the layer is thin enough that  $(r/R)^{l+2} \approx 1$ , equation (2.2.3) can be simplified to

$$\begin{aligned} \left\{ \begin{array}{l} \Delta\tilde{C}_{lm}(t) \\ \Delta\tilde{S}_{lm}(t) \end{array} \right\}_{\text{surf mass}} &= \frac{3}{4\pi R\rho_{\text{ave}}(2l+1)} \int \int \Delta\rho_S(\theta, \lambda; t) \\ &\quad \times \tilde{P}_{lm}(\cos\theta) \left\{ \begin{array}{l} \cos m\lambda \\ \sin m\lambda \end{array} \right\} \sin\theta d\theta d\lambda \end{aligned} \quad (2.2.5)$$

which connects the density redistribution in this layer  $\Delta\rho_S(\theta, \lambda; t)$  with the spherical harmonic coefficients  $\Delta\tilde{C}_{lm}(t)$  and  $\Delta\tilde{S}_{lm}(t)$ . Thus, it describes the contribution to the geoid from the direct gravitational attraction of the surface mass (Wahr et al., 1998). But mass fluctuations on the surface also deform the underlying Earth, which implicates a change in the gravitational potential, and thus a change in the geoid shape, as well. This effect is considered by the so called *Love numbers*  $k_l$ , which were derived from Han & Wahr (1995). They are based on the Preliminary Reference Earth Model (PREM) by Dziewonski & Anderson (1981). The contribution from the deformed solid earth may then be written as

$$\begin{aligned} \left\{ \begin{array}{l} \Delta\tilde{C}_{lm}(t) \\ \Delta\tilde{S}_{lm}(t) \end{array} \right\}_{\text{solid Earth}} &= \frac{3k_l}{4\pi R\rho_{\text{ave}}(2l+1)} \int \int \Delta\rho_S(\theta, \lambda; t) \\ &\quad \times \tilde{P}_{lm}(\cos\theta) \left\{ \begin{array}{l} \cos m\lambda \\ \sin m\lambda \end{array} \right\} \sin\theta d\theta d\lambda \end{aligned} \quad (2.2.6)$$

The total geoid change is obtained by adding equations (2.2.5) and (2.2.6):

$$\left\{ \begin{array}{l} \Delta\tilde{C}_{lm}(t) \\ \Delta\tilde{S}_{lm}(t) \end{array} \right\} = \left\{ \begin{array}{l} \Delta\tilde{C}_{lm}(t) \\ \Delta\tilde{S}_{lm}(t) \end{array} \right\}_{\text{surf mass}} + \left\{ \begin{array}{l} \Delta\tilde{C}_{lm}(t) \\ \Delta\tilde{S}_{lm}(t) \end{array} \right\}_{\text{solid Earth}} \quad (2.2.7)$$

Inserting (2.2.7) into (2.2.2) leads to the so called *isotropic transfer coefficients*, which define the quantity of a spherical harmonic series expansion. In the case of a surface mass density [kg/m<sup>2</sup>], they are simply defined as

$$\Lambda_l = \frac{R\rho_{\text{ave}}}{3} \frac{2l+1}{1+k_l} \quad (2.2.8)$$

If these coefficients are multiplied with the right-hand side of the spherical harmonic synthesis formula (A.8) in the appendix, an expression for the surface mass density in terms of the spherical harmonic coefficients is received:

$$\Delta\rho_S(\theta, \lambda) = \frac{R\rho_{ave}}{3} \sum_{l=0}^{\infty} \frac{2l+1}{1+k_l} \sum_{m=0}^l \tilde{P}_{lm}(\cos\theta) (\Delta\tilde{C}_{lm} \cos m\lambda + \Delta\tilde{S}_{lm} \sin m\lambda) \quad (2.2.9)$$

However, it is usual to convert the surface mass density into *water equivalent heights*, which are commonly used in many other scientific areas. These heights assume the Earth's surface to be covered with a thin layer of water, which reacts to changes in the gravity field. The relation between the water equivalent heights on the surface mass density is given through

$$h_W(\theta, \lambda) = \frac{\Delta\rho_S(\theta, \lambda)}{\rho_W} \quad (2.2.10)$$

$$(2.2.11)$$

where  $\rho_W$  is the average density of water (i.e.  $\rho_W = 1 \text{ g/cm}^3$ ) and thus

$$h_W(\theta, \lambda; t) = \frac{R\rho_{ave}}{3\rho_W} \sum_{l=0}^{\infty} \frac{2l+1}{1+k_l} \sum_{m=0}^l \tilde{P}_{lm}(\cos\theta) \quad (2.2.12)$$

$$\times (\Delta\tilde{C}_{lm}(t) \cos m\lambda + \Delta\tilde{S}_{lm}(t) \sin m\lambda) \quad (2.2.13)$$

This means a change in the surface mass density of  $1 \text{ kg/m}^2$  is equal to 1 mm in water equivalent heights. For the sake of simplicity, the intricate formulation (2.2.12) can be eased to

$$\begin{aligned} \frac{R\rho_{ave}}{3\rho_W} \frac{2l+1}{1+k_l} &= \Lambda_l && \text{isotropic spectral transfer coefficients} \\ \tilde{P}_{lm}(\cos\theta) (\cos m\lambda \quad \sin m\lambda)^T &= \tilde{Y}_{lm}(\theta, \lambda) && \text{normalized surface spherical harmonics} \\ (\Delta\tilde{C}_{lm}(t) \quad \Delta\tilde{S}_{lm}(t))^T &= \Delta\tilde{K}_{lm}(t) && \text{normalized Stokes coefficients} \end{aligned}$$

Equation (2.2.12) reads now as

$$h_W(\theta, \lambda; t) = \sum_{l=0}^{\infty} \Lambda_l \sum_{m=0}^l \tilde{Y}_{lm}(\theta, \lambda) \Delta\tilde{K}_{lm}(t) \quad (2.2.14)$$

This formulation could be used to observe deviations from a monthly or annual mean value in terms of water equivalent heights, which is often used to validate GRACE data with hydrological models. However, this work will compare the estimated mass variations with observed hydrological data, which is given as rate of change of water storage in specific catchments. This would require differentiation of the quantity (2.2.14) with respect to time, which can be done by applying numerical differentiation.

## 2.2.2 Numerical differentiation of gravitational quantities

If the expansion of a function  $f(\theta, \lambda; t)$  in terms of Legendre functions and spherical harmonic coefficients on the sphere is regarded, it becomes clear that the only time-dependant parameters are the Stokes coefficients  $\tilde{K}_{lm}(t)$ , as the Legendre functions and the isotropic transfer coefficients are obviously constant in time:

$$f(\theta, \lambda; t) = \sum_{l=0}^{\infty} \sum_{m=0}^l f_{lm} \tilde{Y}_{lm}(\theta, \lambda) \tilde{K}_{lm}(t) \quad (2.2.15)$$

and thus

$$\dot{f}(\theta, \lambda; t) = \frac{df(\theta, \lambda; t)}{dt} = \sum_{l=0}^{\infty} \sum_{m=0}^l f_{lm} \tilde{Y}_{lm}(\theta, \lambda) \dot{K}_{lm}(t) \quad (2.2.16)$$

An approximate time derivative of the Stokes coefficients (i.e. the GRACE monthly solutions) can be computed according to the numerical differentiation by a three-point mid-point formula:

$$\begin{aligned} \dot{\tilde{K}}_{lm} &= \frac{\tilde{K}_{lm}(t + \Delta t) - \tilde{K}_{lm}(t - \Delta t)}{2\Delta t} \\ &= \frac{1}{2} (\tilde{K}_{lm}(t + 1) - \tilde{K}_{lm}(t - 1)) \text{ for } \Delta t = 1 \end{aligned} \quad (2.2.17)$$

However, this formula needs values before and after the instant of differentiation  $t$ , in fact  $\tilde{K}_{lm}(t + \Delta t)$  and  $\tilde{K}_{lm}(t - \Delta t)$ . If the derivative needs to be evaluated at the beginning or the end of an interval, where no left and right values exist, one can use the methods of forward- and backward-differences:

- Forward difference:  $\dot{\tilde{K}}_{lm} = \frac{\tilde{K}_{lm}(t + \Delta t) - \tilde{K}_{lm}(t)}{\Delta t}$
- Backward difference:  $\dot{\tilde{K}}_{lm} = \frac{\tilde{K}_{lm}(t) - \tilde{K}_{lm}(t - \Delta t)}{\Delta t}$

which use the function value before and after the instant of differentiation  $t$  respectively. If this method of numerical differentiation is applied to the expression for water equivalent heights from the last section, one obtains a rate of mass variations in terms of water equivalent heights

$$\dot{h}_W(\theta, \lambda; t) = \sum_{l=0}^{\infty} \Lambda_l \sum_{m=0}^l \tilde{Y}_{lm}(\theta, \lambda) \dot{\tilde{K}}_{lm}(t) \quad (2.2.18)$$

which can be re-written in matrix-notation:

$$\dot{\mathbf{h}}_W = \mathbf{Y} \boldsymbol{\Lambda} \dot{\mathbf{K}} \quad (2.2.19)$$

where

- |                               |                                                                                                 |
|-------------------------------|-------------------------------------------------------------------------------------------------|
| $\dot{\mathbf{h}}_W$          | $k \times 1$ vector containing the rate of change of water equivalent heights of $k$ datapoints |
| $\tilde{\mathbf{Y}}$          | $k \times (L + 1)^2$ vector (or matrix) with associated normalized Legendre functions           |
| $\boldsymbol{\Lambda}$        | $(L + 1)^2 \times (L + 1)^2$ matrix with isotropic transfer coefficients                        |
| $\dot{\tilde{\mathbf{K}}}(t)$ | $(L + 1)^2 \times 1$ vector with normalized time-variable Stokes coefficients                   |

The computation of the area weighted rate of change of water equivalent heights for one particular region  $\chi$ , defined by a set of  $k$  grid cell centers  $(\theta_j, \lambda_j), j = 1, \dots, k$ , can be done according to

$$\dot{h}(\chi, t) = \sum_{j=1}^k \frac{a(\theta_j, \lambda_j)}{a(\chi)} \sum_{l=0}^{\infty} \Lambda_l \sum_{m=0}^l \bar{Y}_{lm}(\theta_j, \lambda_j) \dot{\tilde{K}}_{lm}(t) \quad (2.2.20)$$

where

$\dot{h}_W(\chi, t)$	rate of mass change in catchment $\chi$
$k$	number of data points in the catchment
$a(\theta_j, \lambda_j)$	area of the grid cell $j$
$a(\chi)$	total area of the catchment $\chi$

The area of a grid cell depends on the latitude of the grid center in the following way:

$$\begin{aligned} a(\theta_j, \lambda_j) &= \int_{\theta_j - \frac{n}{2}}^{\theta_j + \frac{n}{2}} \int_{\lambda_j - \frac{n}{2}}^{\lambda_j + \frac{n}{2}} R^2 \sin \theta d\lambda d\theta \\ &= nR^2 \int_{\theta_j - \frac{n}{2}}^{\theta_j + \frac{n}{2}} \sin \theta d\theta \\ &= nR^2 (\cos(\theta_j - \frac{n}{2}) - \cos(\theta_j + \frac{n}{2})) \end{aligned} \quad (2.2.21)$$

where  $n$  is the spherical side length of a grid cell. Then

$$a(\chi) = \sum_{j=1}^k a(\theta_j, \lambda_j) \quad (2.2.22)$$

It is more common, though, to write (2.2.20) in matrix notation as well:

$$h_W(\chi, t) = \mathbf{S} \mathbf{Y} \boldsymbol{\Lambda} \mathbf{K} \quad (2.2.23)$$

where  $\mathbf{S}$  is a  $1 \times k$  vector which contains the ratios  $\frac{a(\theta_j, \lambda_j)}{a(\chi)}$

However, it should be mentioned that the time-derivative of water equivalent heights is not a completely different quantity than equation (2.2.14). It is just an other representation of spherical harmonic coefficients in the spatial domain (cf. figure 2.3). Thus, even if the discussed methods are only tested with differentiated GRACE coefficients, they can be adopted to e.g. the deviations from a mean as well.

## 2.3 The unfiltered GRACE monthly solutions

The space satellite mission GRACE delivers spherical harmonic coefficients  $\tilde{C}_{lm}$  and  $\tilde{S}_{lm}$  up to degree and order 120, depending on the used dataset. For instance, the Center for Space Research (CSR) provides coefficients and their standard deviations up to degree and order 60. However, a major problem in the determination of gravitational quantities from time-variable GRACE data is the noise level in the coefficients with high degree and order, i.e. the coefficients of short-wavelength. It was shown in various studies with true and simulated GRACE data (e.g. Zenner, 2006; Becker, 2004) that the noise level in these monthly GRACE solutions increases with increasing degree. Kaula (1966) already showed that the signal strength should theoretically attenuate with increasing degree. However, the Stokes coefficients from GRACE paint a different picture.

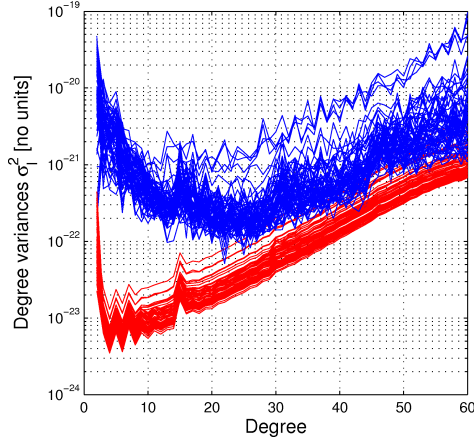


**Figure 2.1:** Signal (blue) and error (red) degree variances of 71 monthly GRACE solutions

In figure 2.3, the degree variances (i.e. the total spectral power of the signal per degree, cf. (C.2)) of 71 monthly solutions from the fourth CSR-dataset release are presented. The signal strength increases for degrees larger than 25. However, such a characteristic is not reasonable for spherical harmonic coefficients from satellite gravity missions. The satellites are less sensitive to short-wavelength mass variations on the Earth. Conversely, the measurable signal strength of such variations decreases with increasing distance from the Earth's surface. As such variations are represented by spherical harmonic coefficients with large degree and order (i.e. higher-frequency coefficients), the spectral signal strength should theoretically attenuate with increasing degree, whis was already stated by Kaula (1966).

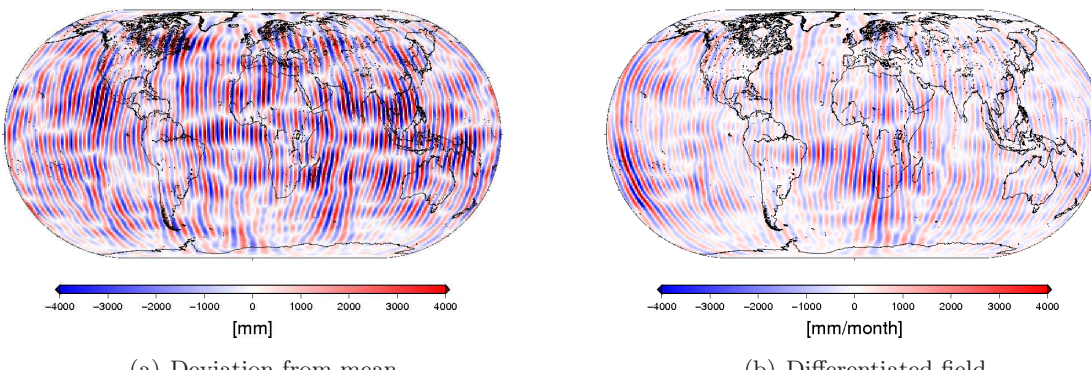


**Figure 2.2:** Water equivalent heights (left) and rate of change of water equivalent heights (right) for January 2003, derived from unfiltered GRACE data

Using unfiltered spherical harmonic coefficients from GRACE yields unrealistic gravity estimates, which can easily be told from the very high signal strength and the spatial characteristic of the derived field (fig. 2.3). The map shows massive north-south stripes with a maximal amplitude of more than 4000 mm and 4000 mm/month respectively, yield-

ing a signal of alternating sign and amplitude in longitude direction. These stripes have their maximal amplitude in near equatorial and equatorial regions, whereas the near polar regions show a rather small signal strength.

The origins of these artifacts are, amongst others, the reduced observability of the sectorial and near-sectorial coefficients from GRACE's polar orbit configuration (Klees et al., 2008) and uncertainties in the atmospheric and oceanic dealiasing models. These models were assumed to be error-free, which is not true. This issue is investigated by Zenner & Gruber (2008) and it has been stated that uncertainties in these models have a direct impact on the monthly GRACE solutions. Furthermore, the true content of good signal or noise in the GRACE coefficients is still not known yet, which makes it necessary to postprocess the satellite data with low-pass filter techniques in order to attenuate the contribution of the noisy higher frequency coefficients.

# Stochastic and deterministic filtering of time-variable GRACE data

3

## 3.1 Spatial averaging: 2-D convolution on a sphere

The spatial average  $\bar{f}(\theta, \lambda)$  of a function is obtained by spatially convolving the unfiltered signal  $f(\theta, \lambda)$  (e.g. water equivalent heights computed from GRACE monthly solutions) with an averaging function on a sphere:

$$\begin{aligned}\bar{f}(\theta, \lambda) &= f(\theta, \lambda) * w(\theta, \lambda) = (f * w)(\theta', \lambda') \\ &= \int_{\Omega} f(\theta', \lambda') w(\theta, \lambda, \theta', \lambda') d\Omega\end{aligned}\tag{3.1.1}$$

where

- $(\theta, \lambda), (\theta', \lambda')$  spherical colatitude and longitude of two points
- $w(\theta, \lambda, \theta', \lambda')$  averaging function
- $f(\theta', \lambda')$  input signal
- $\bar{f}(\theta', \lambda')$  output signal, averaged

and  $\int_{\Omega} d\Omega$  denotes integration over a sphere.

The representation of the spatial input and output signal respectively in terms of a spectral function and spherical harmonics reads as

$$\left\{ \frac{f(\theta, \lambda)}{\bar{f}(\theta, \lambda)} \right\} = \sum_{l=0}^{\infty} \sum_{m=0}^l \left\{ \frac{F_{lm}}{\bar{F}_{lm}} \right\} \tilde{Y}_{lm}(\theta, \lambda)\tag{3.1.2}$$

where

- $F_{lm}$  input signal
- $\bar{F}_{lm}$  output signal, averaged
- $\tilde{Y}_{lm}$  surface spherical harmonics

The spatial averaging procedure is usually performed by multiplicating the function itself with a so called *averaging kernel*  $w_{l'm'}^{lm}$ , in the following also referred as averaging operator, averaging function or simply filter, in the spectral domain:

$$\bar{f}(\theta, \lambda) = \sum_{l=0}^{\infty} \sum_{m=0}^l \sum_{l'=0}^{\infty} \sum_{m'=0}^{l'} w_{l'm'}^{lm} F_{lm} \tilde{Y}_{lm}(\theta, \lambda) \quad (3.1.3)$$

Equation (3.1.3) can be rewritten in matrix notation for a more simple computation:

$$\bar{\mathbf{f}} = \mathbf{Y} \mathbf{W} \mathbf{F} \quad (3.1.4)$$

where

- $\bar{\mathbf{f}}$   $M \times 1$  vector of the filtered signal with  $M$  being the number of data points
- $\mathbf{Y}$   $M \times (L+1)^2$  matrix of spherical harmonics
- $\mathbf{W}$   $(L+1)^2 \times (L+1)^2$  matrix with filter coefficients
- $\mathbf{F}$   $(L+1)^2 \times 1$  vector with the input signal in the spectral domain

The averaging kernel  $w_{l'm'}^{lm}$  is initially of anisotropic nature and thus adept to the geographical latitude and therefore to the data density of a satellite mission (Kusche, 2007). This means that it considers correlations between the spherical harmonic coefficients or, conversely, depends on the position of two points in space in the spatial domain. Its transformation from the spectral to the spatial domain reads as

$$\begin{aligned} w(\theta, \lambda, \theta', \lambda') = & \sum_{lm} \sum_{l'm'} \tilde{P}_{lm} \tilde{P}_{l'm'} [(w_{l'm'}^{lmc} \cos m' \lambda' + w_{l'm'}^{lms} \sin m' \lambda') \cos m \lambda \\ & + (w_{l'm'}^{lms} \cos m' \lambda' + w_{l'm'}^{lmc} \sin m' \lambda') \sin m \lambda] \end{aligned} \quad (3.1.5)$$

Such averaging functions are called *anisotropic vector filters*, the appropriate filter matrix  $\mathbf{W}$  is fully populated. However, most filters neglect the correlations between the spherical harmonic coefficients, i.e.  $w_{l'm'}^{lmc} = w_{l'm'}^{lms} = 0$  and  $w_{l'm'}^{lmc} = w_{l'm'}^{lms} = 0$  if  $l \neq l'$  and  $m \neq m'$ , yielding a diagonal filter matrix with degree and order dependent filter coefficients. Such operators are called *anisotropic scalar filters*. Their propagation to the spatial domain reads as

$$w(\theta, \lambda) = \sum_{l=0}^{\infty} \sum_{m=0}^l \tilde{P}_{lm}(\cos \theta) (w_{lm}^c \cos m \lambda + w_{lm}^s \sin m \lambda) \quad (3.1.6)$$

where the spectral filter coefficients are given through

$$\begin{Bmatrix} w_{lm}^c \\ w_{lm}^s \end{Bmatrix} = \frac{1}{4\pi} \int_{\Omega} w(\theta, \lambda) \tilde{P}_{lm}(\cos \theta) \begin{Bmatrix} \cos m \lambda \\ \sin m \lambda \end{Bmatrix} d\Omega \quad (3.1.7)$$

Such a propagated kernel in the spatial domain still depends on both longitude and latitude of a single point in space. However, most simple averaging operators are of isotropic nature, i.e. *isotropic filters*. This means that they do not depend on a specific position, but on the spherical distance between two points in space:

$$w(\theta, \lambda, \theta', \lambda') = w(\alpha) \quad \text{with} \quad \cos \alpha = \cos \theta \cos \theta' + \sin \theta \sin \theta' \cos(\lambda - \lambda') \quad (3.1.8)$$

An expansion of such a function in terms of Legendre polynomials reads as

$$w(\alpha) = \sum_{l=0}^{\infty} \frac{2l+1}{2} w_l P_l(\cos \alpha) \quad (3.1.9)$$

Thus, such an operator is of isotropic nature, as it only depends on its the degree  $l$  and is thus independent of the position in the spatial domain. Its spectrum is defined as

$$w_l = \int_0^{\pi} w(\alpha) P_l \cos(\alpha) \sin \alpha d\alpha \quad (3.1.10)$$

Such averaging functions can be normalized and thus vary from values between 1 at the computation point (e.g.  $w(\alpha = 0) = 1$ ) and 0 at a point with a greater spherical distance than the maximal smoothing radius. This maximal distance depends on the used averaging kernel. However, the function  $\bar{f}(\theta, \lambda)$ , filtered with an isotropic filter, can be seen as an average over a spherical cap, centered at the point  $(\theta, \lambda)$  (Becker, 2004), whereas the shape of the anisotropic filter kernels in the spatial domain might change with latitude and longitude.

These basic formulae for spatial averaging of spherical harmonic coefficients hold for each presented filter in this work. This allows one to easily compare the efficiency of isotropic, anisotropic scalar and anisotropic vector filters.

The covariance of a filtered signal is given via the covariance propagation law

$$\mathbf{Q}_{\bar{f}} = \mathbf{W} \mathbf{Q}_F \mathbf{W}^T \quad (3.1.11)$$

where  $\mathbf{Q}_F$  is the covariance-variance matrix of the function in the spectral domain and  $\mathbf{W}$  is an arbitrary filter matrix.

## 3.2 Deterministic averaging

### 3.2.1 The isotropic and anisotropic Gaussian filter

The Gaussian filter is widely used for noise reduction in digital image processing. It smoothes a signal by attenuating the power of high-frequencies, which results in a soft-focused image. This characteristic is also used in physical geodetic problems, where the gravity signal is represented by a set of degree and order dependent Stokes coefficients  $\tilde{C}_{lm}$  and  $\tilde{S}_{lm}$ . The high frequency coefficients from GRACE, i.e. these coefficients with large degree and order, are highly contaminated with noise, yielding a higher signal strength than the low frequency coefficients (cf. figure 2.3). Thus, the Gaussian filter attenuates the influence of these coefficients with degree dependent weight factors  $w_l$ . These weights are computed without any knowledge about the gravity signal itself. This means that the filter coefficients are easily computable, but do not take any information about the signal or its stochastics into account. They only depend on an *averaging radius*  $r$ , which defines the smoothing level.

The spectral ( $w_l$ ) and spatial ( $w(\alpha)$ ) filter coefficients are computed according to the formulae proposed in (Jekeli, 1981):

$$w(\alpha) = \frac{b}{2\pi} \frac{e^{-b(1-\cos\alpha)}}{1 - e^{-2b}} \quad (3.2.1)$$

$$\text{with } b = \frac{\ln(2)}{1 - \cos(r_{\frac{1}{2}}/R)}$$

Equation (3.2.1) is the spatial representation of the filter with  $r_{\frac{1}{2}}$  being the distance on the Earth's surface at which  $w(\alpha)$  has dropped to half its value at  $\alpha = 0$ . Thus, the averaging radius is also called *halfwidth radius* and is used to describe the Gaussian averaging operator. In the spectral domain, the Legendre spectrum of the averaging function can be calculated recursively:

$$\begin{aligned} w_0 &= \frac{1}{2\pi} \\ w_1 &= \frac{1}{2\pi} \left[ \frac{1 + e^{-2b}}{1 - e^{-2b}} - \frac{1}{b} \right] \\ w_{l+1} &= -\frac{2l+1}{b} w_l + w_{l-1} \end{aligned} \quad (3.2.2)$$

By choosing a large or small averaging radius, one can choose the level of smoothing. As the previous averaging coefficients (3.2.2) are isotropic, i.e. they depend only on their degree and are thus independent from the position in the spatial domain, Han et al. (2005) presented an anisotropic filter, based on the Gaussian type averaging method. The operator basically depends on an averaging radius as well, but in both longitude and latitude direction. Thus, it also depends on the order  $m$ , which explains its anisotropic characteristic. The formulae for its computation read as

$$\begin{aligned} w_{lm} &= w_l(r_{\frac{1}{2}}(m)) \\ \text{with } r_{\frac{1}{2}}(m) &= \frac{r_1 - r_0}{m_1} m + r_0 \end{aligned} \quad (3.2.3)$$

Here, the parameters  $r_0$  and  $r_1$  respectively are the averaging radii, applied for zonal harmonics ( $m = 0$ ) and for order  $m_1$  harmonics ( $m = m_1$ ), and  $w_l$  are the isotropic averaging coefficients from (3.2.2). Obviously, if  $r_0 = r_1$ , one obtains the isotropic Gaussian smoothing operator. The spatial resolution of the averaging function depends on

- $r_0$  in latitude and
- $r_1$  and  $m_1$  in longitude direction

where  $r_1$  is usually chosen to be  $r_1 = 2r_0$ , which yields a better resolution in latitude direction than the isotropic Gaussian filter. In contrast to its isotropic counterpart, the anisotropic Gaussian filter passes the higher degree and lower order coefficients and rejects undesired higher order coefficients (Han et al., 2005). In figure 3.1 the filter coefficients of both isotropic and anisotropic Gaussian averaging operators are presented.

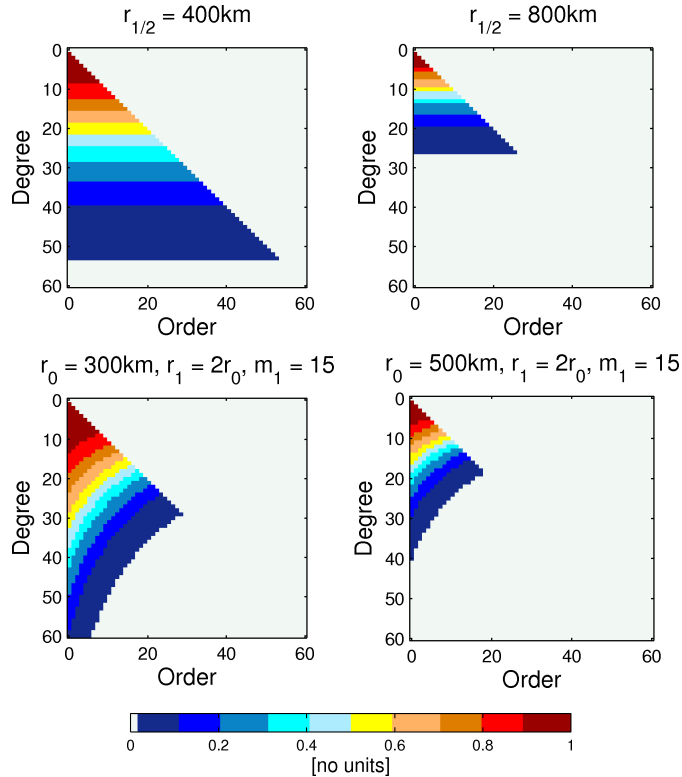


**Figure 3.1:** Filter coefficients in the spectral domain of the anisotropic and isotropic Gaussian averaging operator

In either case, the larger the chosen  $r_{\frac{1}{2}}/(r_0 \text{ and } r_1)$ , the less the weight is given to the high frequency coefficients.

The Gaussian averaging operator indeed reduces the noise level of the time-variable gravity signal, and delivers usable results, depending on the averaging radius. However, one of its disadvantages is the dependency of this radius. If the maps in figure 3.2 are compared, it becomes clear that the filter also reduces the power of the good signal and thus reduces the spatial resolution, which is obvious e.g. in the Amazon basin. There, all four maps show a large continuous basin, but the observed mass variations are different. On the other hand, the filter has theoretically no impact on the erroneous north-south-stripes. Swenson & Wahr (2006) found out that correlations in the spherical harmonic coefficients with  $m > 7$  cause spatial correlations, i.e. the stripy artifacts. The Gaussian filter attenuates the contribution of high frequency coefficients, yielding a significantly reduced signal strength of these erroneous stripes.

Thus, the right choice of the averaging radius is a bit tricky, as a large radius results in a heavily filtered field, which indeed possesses less noisy artifacts, but has a very limited spatial resolution. On the flipside, averaging with a too small radius would deliver a field with a still unrealistic magnitude of mass variations (cf. figure 3.2a, c)

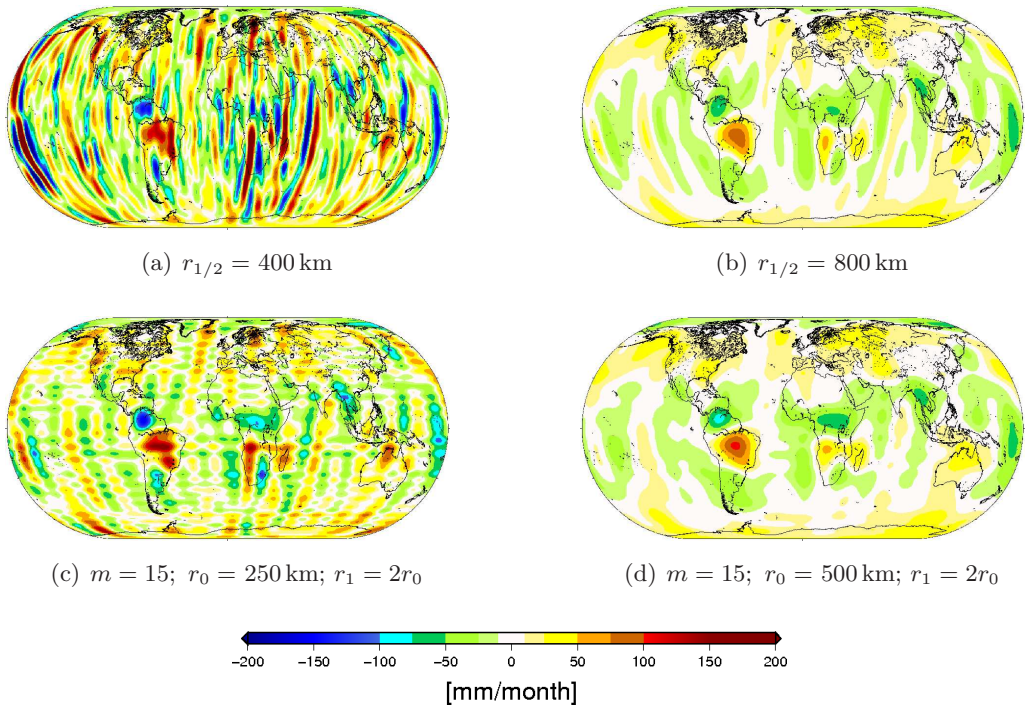


**Figure 3.2:** Derived maps from time variable GRACE solutions smoothed with anisotropic (bottom row) and isotropic (top row) Gaussian averaging operators

Like in the isotropic case, the anisotropic Gaussian averaging operator needs a minimal filter radius to successfully remove the noisy artifacts from the GRACE-derived maps. But filtering with  $r_0 = 500$  km already shows results, which could be used without any further modifications. However, through its deterministic origin, the quality and the reliability of filtered Stokes coefficients depend on a careful choice of the averaging radii, whereas the anisotropic Gaussian filter yields a generally higher spatial resolution, combined with a bigger signal strength than its isotropic counterpart.

### 3.2.2 The correlated error filter

As mentioned before, Gaussian filtering indeed reduces the noise level in maps of geophysical quantities, but removes the erroneous north-south stripes only for large averaging radii, which yields an attenuation of the good signal as well. However, Swenson & Wahr (2006) found out that these stripes come from correlations in the high-frequency Stokes coefficients. It was stated that coefficients of even or odd parity with the same order are highly correlated. On the other hand, this characteristic could not be observed with coefficients with the same degree. Thus, they designed a filter, which isolates and removes smoothly varying coefficients of like parity (Swenson & Wahr, 2006) by smoothing the Stokes coefficients for a particular order  $m$  with a quadratic polynomial in a moving window centered about degree  $l$ :

$$\bar{K}_{lm} = \sum_{i=0}^p \sum_{\omega=-w}^w Q_{(l+2\omega),m;i} (l+2\omega)^i \quad (3.2.4)$$

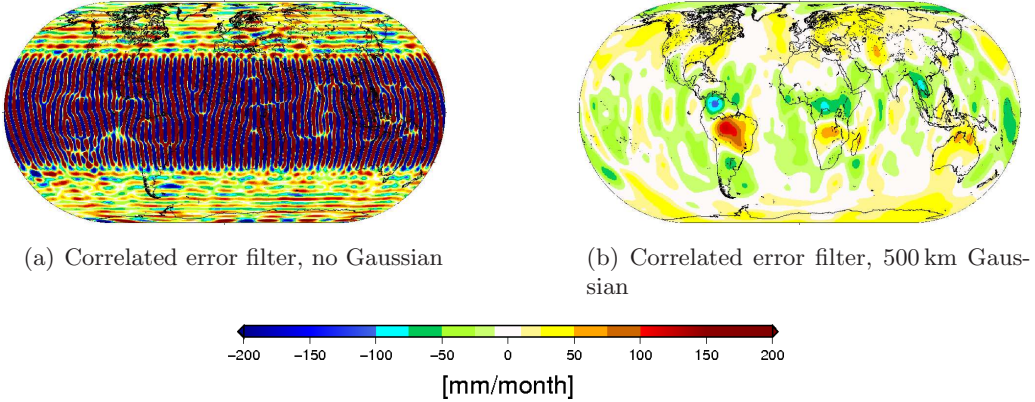


**Figure 3.3:** GRACE derived maps of water equivalent heights per month, filtered with a correlated error filter with  $m_0 = 8$ ;  $m_1 = 60$ ;  $l_0 = 8$ ;  $l_1 = 60$ ;  $p = 2$

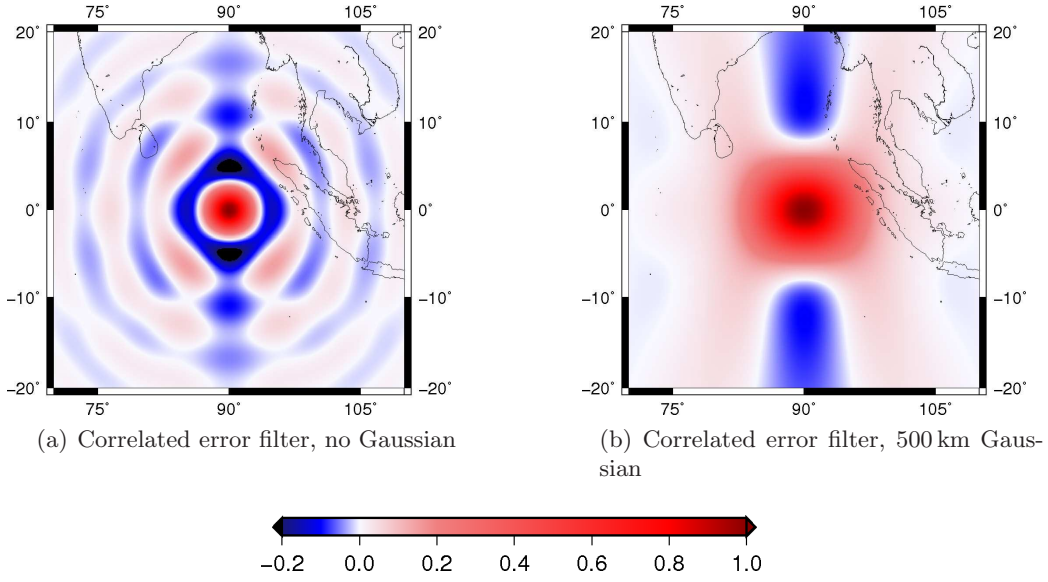


**Figure 3.4:** Propagated averaging functions at  $\theta = 90^\circ, \lambda = 90^\circ$

where

$\bar{K}_{lm}$	filtered sh-coefficient
$w$	window size
$Q_{(l+2\omega),m;i}$	degree $i$ coefficient of the polynomial fit
$p$	order of the polynomial (here: $p = 2$ )
$l, m$	degree and order

Applying this filter and transforming the smoothed coefficients in the spatial domain yields a field with massive north-south artifacts around the equator. Thus, such a derived field must be further filtered with e.g. a Gaussian filter (cf. figure 3.3).

The effect of this filter is clearly recognizable when the operator is propagated to the spatial domain (cf. figure 3.4). The averaging function is evaluated at the location  $\theta = 90^\circ, \lambda = 90^\circ$  and presented before and after the convolution with the Gaussian

filter. The correlated error filter weighs the regions north and south of the kernel negatively, while increasing the contribution of the eastern and western regions. If one thinks about the north-south stripes in the maps from unfiltered GRACE coefficients, it becomes obvious that the signal in the stripes with the same phase is seriously attenuated, while the signal in stripes which are out-of-phase is increased. The successful removal of the north-south stripes emphasizes the assumption of the spherical harmonic coefficients with the same order and parity being correlated. Thus, one speaks of *decorrelation* or *destriping* in this context.

### 3.3 Stochastic averaging

#### 3.3.1 The Wiener filter

The Wiener filter, named after its inventor Norbert Wiener, is widely used to reduce the noise level in signal processing tasks. The basic idea behind this operator is to minimize the deviations between the filtered signal and a desired output signal in a least squares sense. Therefore, the filter takes the errors of the measured signal into account, which yields the term stochastic (in contrast to the deterministic filter, which only depends on an averaging radius). However, the filter needs prior knowledge about the desired signal, which is not the case for the spherical harmonic GRACE coefficients. But on the other hand, Sasgen et al. (2006) designed a filter, which uses certain characteristics of spherical harmonic coefficients to roughly approximate a desired output signal. In this work, it has the form of a power law and is also referred to as a Kaula-type rule for time-variable gravity (cf. section 4.1).

A degree variance model for GRACE data is approximated in such way that the spectral signal power attenuates with increasing degree. This attenuation comes from the lower sensitivity of the satellites on variations of short wavelength in the gravity field, yielding a lower spectral power of the appropriate high frequency spherical harmonic coefficients. The deviations of the measured signal degree variances from such a model are assumed to be noise.

The Wiener filter basically minimizes these deviations in a least squares sense:

$$\bar{f}_{lm} : \min \|\bar{f}_{lm} - s_{lm}\| \quad (3.3.1)$$

where

$\bar{f}_{lm}$  filtered output signal  
 $s_{lm}$  desired output signal

The unfiltered input signal  $f_{lm}$  is assumed to consist of the uncontaminated desired signal  $s_{lm}$  and an additive noise  $n_{lm}$

$$f_{lm} = s_{lm} + n_{lm} \quad (3.3.2)$$

In the case of filtering spherical harmonic coefficients, the desired signal is assumed to be an estimated degree variance model, and the additive noise are the deviations of the mean spectral power from this model:

$$n_l^2 = \sum_{m=0}^l \left( \sqrt{\frac{\langle \sigma_l^2 \rangle}{2l+1}} - \sqrt{\frac{s_l^2}{2l+1}} \right)^2 \quad (3.3.3a)$$

$$n_{lm} = \sqrt{\frac{n_l^2}{2l+1}} \quad (3.3.3b)$$

where

- $n_l^2$  degree variances of deviations
- $n_{lm}$  RMS of deviations
- $\langle \sigma_l^2 \rangle$  mean power of a time series (e.g. annual, monthly, etc.)
- $s_l^2$  degree variance model

However, it was shown from Devaraju & Sneeuw (2007) that using a combination of the estimated errors and their deviations as noise yields a better resolution:

$$\epsilon_{lm} = \sqrt{\frac{n_l^2}{2l+1} + \varepsilon_{lm}^2}, \quad \epsilon_l^2 = n_l^2 + \varepsilon_l^2 \quad (3.3.4)$$

where  $\varepsilon_{lm}^2$  are the variances of the simulated GRACE covariance matrices in the anisotropic case or their error degree variances  $\varepsilon_l^2$  in the isotropic case respectively.

Considering the minimal deviations from the filtered signal and the desired signal (equation (3.3.1)), the Wiener filter kernels are defined as follows:

- isotropic Wiener filter, assuming the same weight for all coefficients with the same degree

$$W_l = \frac{s_l^2}{s_l^2 + \varepsilon_l^2} \quad (3.3.5)$$

- anisotropic scalar Wiener filter, assuming different weights for each degree and order

$$W_{lm} = \frac{\frac{s_l^2}{2l+1}}{\frac{s_l^2}{2l+1} + \varepsilon_{lm}^2} \quad (3.3.6)$$

- anisotropic vector Wiener filter, assuming correlations between the filter coefficients

$$\mathbf{W}_Q = \frac{\mathbf{Q}_S}{\mathbf{Q}_S + \mathbf{Q}_\epsilon} \quad (3.3.7)$$

with  $\mathbf{Q}_S = \text{diag}[s_{lm}], m = 0, 1, \dots, L; l = m, m+1, \dots, L$  and  $\mathbf{Q}_\epsilon = \mathbf{n} + \mathbf{Q}_\varepsilon$  where  $\mathbf{Q}_\varepsilon$  is a simulated full covariance matrix and  $\mathbf{n} = \text{diag}[n_{lm}^2], m = 0, 1, \dots, L; l = m, m+1, \dots, L$

Thus, the numerator of these operators is always the signal covariance, whereas the denominator is defined as the sum of this signal covariance and the noise covariance.

### 3.3.2 The Bayesian type regularization as a spectral filter

#### Introduction

This section deals with an averaging method, which is similar to the presented filter in (Kusche, 2007). The fundamental idea is to use prior information to constrain the noisy GRACE coefficients within a least squares estimation procedure. However, the concept of the so-called *Bayesian type regularization* (Koch & Kusche, 2002) is usually applied to stabilize an ill-posed system of normal equations by adding prior stochastic information about the yet unknown parameters as constraint. Usually, this information is stored in a positive definite diagonal matrix. In (Kusche, 2007) it was found out that such a filter bears very promising results. However, the filter itself uses stochastic data from geophysical models. But the following derivations will show that such an averaging operator works as well with stochastics, derived from GRACE data.

#### Regularized least squares estimation

The fundamental linear model for the presented method reads as

$$E\{\mathbf{y}\} = \mathbf{Ax} \quad D\{\mathbf{y}\} = \sigma^2 \mathbf{Q} = \mathbf{P}^{-1} \quad (3.3.8)$$

where

- $\mathbf{y}$   $m \times 1$  vector of observations
- $\mathbf{A}$   $m \times n$  design matrix
- $\mathbf{x}$   $n \times 1$  vector of unknowns
- $\sigma^2$  scalar variance component
- $\mathbf{Q}$   $m \times m$  covariance matrix of the observations

It is usual, though, to write equation (3.3.8) as an observation equation:

$$\mathbf{y} + \mathbf{e} = \mathbf{Ax} \quad \text{with } E\{\mathbf{e}\} = \mathbf{0} \quad \text{and } D\{\mathbf{e}\} = D\{\mathbf{y}\} = \sigma^2 \mathbf{Q} = \mathbf{P}^{-1} \quad (3.3.9)$$

where  $\mathbf{e}$  is a  $m \times 1$  vector of the observation errors. The unknowns are usually estimated by minimizing the squared residuals

$$\mathbf{x} : \min \|\mathbf{Ax} - \mathbf{y}\|_P^2 \quad (3.3.10)$$

which is achieved by the unbiased least squares estimator

$$\hat{\mathbf{x}} = (\mathbf{A}^\top \mathbf{P} \mathbf{A})^{-1} \mathbf{A}^\top \mathbf{P} \mathbf{y} \quad (3.3.11)$$

with the parameter covariance

$$\mathbf{Q}_{\hat{\mathbf{x}}} = (\mathbf{A}^\top \mathbf{P} \mathbf{A})^{-1} \quad (3.3.12)$$

However, many geodetic problems, especially the determination of the gravity field (Bouman & Koop, 1998; Xu, 1992), are ill-posed problems due to a bad condition of the normal matrix

$$\mathbf{N} = \mathbf{A}^\top \mathbf{P} \mathbf{A} \quad (3.3.13)$$

which is due to the following four characteristics of gravity data from space satellite missions.

- irregular data distribution due to polar gaps or non-continuous data tracking
- insufficient information about the gravity field in the observable itself
- downward continuation
- bad condition due to stochastic model (e.g. the instrument is unable to measure in the whole spectral domain)

Such an ill-conditioned matrix denies a stable solution of the minimization problem. In other words, the normal matrix has information about the unknowns, but not enough for inversion. A widely used method is to regularize the ill-posed system of normal equations (Bouman & Koop, 1998; Xu, 1992; Koch & Kusche, 2002). This happens by adding prior information about the unknown parameters. Such data is of stochastic nature and is thus defined through its expectation value and dispersion:

$$E\{\mathbf{x}_0\} = \mathbf{x} \quad D\{\mathbf{x}_0\} = \sigma_K^2 \mathbf{K} = \mathbf{P}_K^{-1} \quad (3.3.14)$$

where  $\mathbf{x}_0$  is a vector with prior information and  $\mathbf{K}$  its appropriate covariance.  $\sigma_K^2$  is again a yet unknown variance component, which is discussed later. This modifies the minimization problem (3.3.10) to

$$\mathbf{x} : \min \|A\mathbf{x} - \mathbf{y}\|_P^2 + \lambda \|\mathbf{x} - \mathbf{x}_0\|_{P_K}^2 \quad (3.3.15)$$

where  $\lambda$  is a positive real number, defined as the ratio between the variance components of the observation groups. It thus describes the compromise between the constraint and the minimization of the observation error (Bouman & Koop, 1998).

$$\lambda = \frac{\sigma^2}{\sigma_K^2} \quad (3.3.16)$$

Obviously, the parameters are estimated under the constraint that the squared residual between the *a priori* values and the estimated parameters is minimal. However, it is common to assume the observations  $\mathbf{x}_0$  to be zero and their appropriate weight matrix  $\mathbf{P}_K$  to be a positive definite diagonal matrix with its elements being inversely proportional to a degree variance model (Koch & Kusche, 2002). Additionally, it is assumed in this work that this degree variance model is considered as independent observation, which allows to combine expectancy value and dispersion of (3.3.8) and (3.3.14) in a sequential estimation scheme:

$$E\left\{\begin{pmatrix} \mathbf{y} \\ \mathbf{x}_0 \end{pmatrix}\right\} = \begin{pmatrix} \mathbf{A} \\ \mathbf{I} \end{pmatrix} \mathbf{x}; \quad (3.3.17)$$

$$D\left\{\begin{pmatrix} \mathbf{y} \\ \mathbf{x}_0 \end{pmatrix}\right\} = \begin{pmatrix} \sigma^2 \mathbf{Q} & 0 \\ 0 & \sigma_K^2 \mathbf{K} \end{pmatrix} \quad (3.3.18)$$

$$(3.3.19)$$

which is solved by minimizing the squared residuals

$$\mathbf{x} : \min \|A\mathbf{x} - \mathbf{y}\|_P^2 + \lambda \|\mathbf{x}\|_{P_K}^2 \quad (3.3.20)$$

Such a regularization constrains the unknown Stokes coefficients to be minimal (i.e. equal to zero) and to vary according to the *a priori* variance matrix  $\mathbf{K}$  and is solved by the unbiased estimator

$$\hat{\mathbf{x}} = (\mathbf{A}^T \mathbf{P} \mathbf{A} + \lambda \mathbf{P}_K)^{-1} (\mathbf{A}^T \mathbf{P} \mathbf{y}) \quad (3.3.21)$$

with the parameter covariance

$$\mathbf{Q}_{\hat{x}} = (\mathbf{A}^T \mathbf{P} \mathbf{A} + \lambda \mathbf{P}_K)^{-1} = \mathbf{N}^{-1} \quad (3.3.22)$$

A widely used method to improve the condition for static gravity field determinations is to use the Kaula rule (Kaula, 1966) as *a priori* degree variance model, which constrains the coefficients to attenuate with increasing degree according to a power law:

$$\hat{\sigma}_l^2 \approx \frac{10^{-10}}{l^4} (2l + 1) \quad (3.3.23)$$

This method differs from the so called *Tikhonov-regularization* (Tikhonov & Arsenin, 1977), which is often used to improve the stability of an ill-posed system of normal equations as well. There, the basic idea is to constrain the solution of the least squares estimation to be finite, which is achieved by strengthen the main diagonal of the normal matrix, e.g. by adding an identity matrix. Here, prior information in form of modelled signal variances is added as constraint, which allows unbiased sequential estimation. However, the term unbiased estimation needs a bit of discussion in this context. In (Xu, 1992; Bouman & Koop, 1998; Bouman, 2000) it was mentioned that regularization must be considered as biased estimation, as the solution seriously depends on the quality of the prior information  $\mathbf{K}$ . The regularization matrix  $\mathbf{K}$  is filled with elements from a signal variance model (e.g. Kaula's rule) and not with error variances. But according to (Sneeuw, 2000), this would lead to too optimistic error estimates. Moreover, this variance model is introduced as an independent observation group, which assumes the time-variable Stokes coefficients to be equal to zero with their appropriate variance. This might sound a bit confusing but can be explained with gravity potential theory. According to equation A.10 the gravity potential consists of a constant part, the normal field, and the disturbing potential. The influence of the normal field is usually removed from spherical harmonic coefficients, as it is known by its definition. The remaining disturbing potential is normal distributed with an expectation value of zero. This means conversely that the time-variable spherical harmonic coefficients have an expectation value equal to zero as well, as they are the only stochastic factor in the series expansion of a gravitational quantity in terms of Legendre functions. Their errors, i.e. their variances, are given through a model, where the spectral signal power of the error degree variances usually attenuate with increasing degree. Furthermore, the Tikhonov-regularization would not allow to estimate the yet unknown variance components. Using an identity matrix with a regularization parameter as regularization term can not be assumed to be a separate observation group and thus does not allow the combination in one linear model by setting up a sequential estimation scheme.

### Using the regularization as spectral filter for time-variable grace coefficients

However, the task in this work is not to solve an ill-posed system of normal equation, but such a degree variance model can used to constrain the GRACE solutions as well, as it provides an upper bound on the uncertainties in spherical harmonic coefficients at high degrees. Thus, equation (3.3.11) can be rewritten as a spectral filter, if it is used to re-estimate a set of spherical harmonic coefficients. Then,  $\mathbf{A}$  becomes the identity matrix,

$\mathbf{P}_G$  the inverse covariance matrix of the spherical harmonic coefficients (e.g. a simulated full covariance matrix for GRACE coefficients) and  $\mathbf{y}$  the coefficients themselves:

$$\begin{aligned}\hat{\mathbf{x}} &= \left( \mathbf{A}^\top \mathbf{P}_G \mathbf{A} + \lambda \mathbf{P}_K \right)^{-1} \mathbf{A}^\top \mathbf{P}_G \mathbf{y} \\ &= (\mathbf{I} \mathbf{P}_G \mathbf{I} + \lambda \mathbf{P}_K)^{-1} \mathbf{A}^\top \mathbf{P}_G \mathbf{y} \\ &= (\mathbf{P}_G + \lambda \mathbf{P}_K)^{-1} \mathbf{P}_G \mathbf{y}\end{aligned}\quad (3.3.24)$$

The covariance matrix of the regularized parameters is the inverse normal matrix:

$$\mathbf{Q}_{\hat{\mathbf{x}}} = (\mathbf{P}_G + \lambda \mathbf{P}_K)^{-1} \quad (3.3.25)$$

Obviously, the structure of this filter operator is similar to the Wiener filter from chapter 3.3.1. But the filtering characteristics are different, as the Wiener filter minimizes the deviations of the filtered signal degree variances (i.e. the measured signal) and a desired output signal (i.e. an estimated degree variance model) in a least squares sense. The operator 3.3.24, on the other hand, constrains the signal power to decrease with increasing degree by using the measured signal  $\mathbf{y}$  as observations and a degree variance model  $\mathbf{K}$  as constraints, based on a least squares estimation procedure. However, both averaging operators allow the consideration of a full covariance matrix of the GRACE coefficients.

### Variance component estimation

It was already mentioned that the regularization parameter  $\lambda$  is defined as the ratio between the variance components  $\sigma_G^2$  and  $\sigma_K^2$  of the observation groups. But these variance components are initially unknown and must be estimated by a so called *Variance Component Estimation* (VCE). This step is not allowed if one uses the Tikhonov-type regularization, as the regularization matrix does not necessarily contain observed or modeled prior information. It simply strengthens the stability of a normal matrix by constraining the least squares solution to be finite. In this case here, the regularization matrix contains a degree variance model, which is assumed to be a separate observation group. Thus, one is able to compute the weight factors between these groups by the VCE.

Variance components can be estimated through different approaches. A few of them are

- Minimum norm quadratic unbiased estimator (MINQUE)
- Best invariant quadratic unbiased estimator (BIQUE)
- Least squares variance component estimator (LS-VCE)
- Restricted maximum likelihood estimator (REML)
- Bayesian approach to VCE

A detailed review of each of these methods would go beyond the scope of this work. Thus, the reader is referred to further literature (e.g. Fotopoulos, 2003). In this thesis, only the least squares variance component estimator is discussed, or rather the modified version from (Koch & Kusche, 2002), which is proposed for estimating weight factors within a regularization procedure. Here, the inverse weight factors (i.e. the variance components) of the different observation groups are defined as the ratio between their mean squared error and their contribution to the overall redundancy. Thus, an observation group gets a bigger weight if

- the corresponding observations are very accurate, which results in a small mean squared error and/or
- it has only little contribution to the result, which is reflected by a large redundancy number.

In section 3.3.2 the contribution of an observation group to the estimated parameters was only defined by their inverse *a priori* covariance; their particular variance component was assumed to be one (which is often done in least squares estimation). But the weight matrices  $\mathbf{P}_G$  and  $\mathbf{P}_K$  consist more precisely of a known part, which actually is the inverse *a priori* covariance and a yet unknown variance component, which describes how a particular observation group fits into the linear system. This was already formulated in equation (3.3.8) and (3.3.14), but not further discussed. If the estimator (3.3.24) is modified in such way, it reads as

$$\hat{\mathbf{x}} = \left( \frac{1}{\sigma_G^2} \mathbf{P}_G + \frac{1}{\sigma_K^2} \mathbf{P}_K \right)^{-1} \frac{1}{\sigma_G^2} \mathbf{P}_G \mathbf{y} \quad (3.3.26)$$

which is actually the same as (3.3.24), if one assumes that  $\lambda = \sigma^2/\sigma_K^2$ . However, this point is a bit delicate. The conversion from equation (3.3.24) to (3.3.26) reads as follows:

$$\begin{aligned} \hat{\mathbf{x}} &= (\mathbf{P}_G + \lambda \mathbf{P}_K)^{-1} \mathbf{P}_G \mathbf{y} \\ &= \left( \mathbf{P}_G + \frac{\sigma_G^2}{\sigma_K^2} \mathbf{P}_K \right)^{-1} \mathbf{P}_G \mathbf{y} \\ &= \left( \frac{1}{\sigma_G^2} \mathbf{P}_G + \frac{\sigma_G^2}{\sigma_G^2 \sigma_K^2} \mathbf{P}_K \right)^{-1} \frac{1}{\sigma_G^2} \mathbf{P}_G \mathbf{y} \\ &= \left( \frac{1}{\sigma_G^2} \mathbf{P}_G + \frac{1}{\sigma_K^2} \mathbf{P}_K \right)^{-1} \frac{1}{\sigma_G^2} \mathbf{P}_G \mathbf{y} \end{aligned} \quad (3.3.27)$$

Thus, there is a difference in the normal matrix, as both versions  $(\mathbf{P}_G + \lambda \mathbf{P}_K)^{-1}$  and  $\left( \frac{1}{\sigma_G^2} \mathbf{P}_G + \frac{1}{\sigma_K^2} \mathbf{P}_K \right)^{-1}$  actually differ by the factor  $\frac{1}{\sigma_G^2}$ . This divergence does not play a role if one assumes the variance components to be one. In the case of estimated variance components, the normal matrix  $(\mathbf{P}_G + \lambda \mathbf{P}_K)^{-1}$  must be divided by  $\sigma_G^2$  to obtain the true *a posteriori* error level. Otherwise the errors would be biased, depending on the variance component  $\sigma_G^2$ . Thus, it is recommended to use the parameter  $\lambda$  only for comparison purposes, but consider both variance components for the computation of the covariance matrix of the estimated parameters:

$$\mathbf{Q}_{\hat{\mathbf{x}}} = \left( \frac{1}{\sigma_G^2} \mathbf{P}_G + \frac{1}{\sigma_K^2} \mathbf{P}_K \right)^{-1} \quad (3.3.28)$$

The estimation of the variance components is an iterative process, in which the unknown weight factors are estimated with respect to the *a posteriori* errors and the redundancy number of the different observation groups. This is achieved by the four following steps, which are repeated until the variance components converge:

1. Estimation of the unknown parameters according to equation (3.3.26)
2. Computation of the residuals in the different observation groups

$$\hat{\mathbf{e}} = \hat{\mathbf{x}} - \mathbf{y}; \quad \hat{\mathbf{e}}_K = \hat{\mathbf{x}} \quad (3.3.29)$$

3. Computation of the partial redundancies, i.e. the contributions of the observations and prior information to the overall redundancy (Koch & Kusche, 2002)

$$r_G = u - \text{tr} \left( \frac{1}{\sigma_G^2} \mathbf{P}_G \mathbf{N}^{-1} \right) \quad (3.3.30a)$$

$$r_K = u - \text{tr} \left( \frac{1}{\sigma_K^2} \mathbf{P}_K \mathbf{N}^{-1} \right) \quad (3.3.30b)$$

In equation (3.3.30a) and (3.3.30b)  $u$  is the number of observations, which is in this case the number of available GRACE coefficients, i.e.  $u = (L_{\max} + 1)^2 - 4$ , as the degree 0 and 1 coefficients were removed. The values  $\text{tr} \left( \frac{1}{\sigma_G^2} \mathbf{P}_G \mathbf{N}^{-1} \right)$  and  $\text{tr} \left( \frac{1}{\sigma_K^2} \mathbf{P}_K \mathbf{N}^{-1} \right)$  respectively are the sum of the single redundancy elements from the redundancy contribution (cf. section C.2.3). They are a measure for the amount of information (from the corresponding observation group) which contributes to the result  $\hat{x}$

4. Computation of the variance components for each observation group

$$\hat{\sigma}_G^2 = \frac{\hat{\mathbf{e}}_G^T \mathbf{P}_G \hat{\mathbf{e}}_G}{r_G} \quad (3.3.31a)$$

$$\hat{\sigma}_K^2 = \frac{\hat{\mathbf{e}}_K^T \mathbf{P}_K \hat{\mathbf{e}}_K}{r_K} \quad (3.3.31b)$$

In the first iteration, it is assumed that  $\sigma_G = \sigma_K = 1$ . Thus, the estimated parameters  $\hat{x}$  of the first iteration equal the regularized parameters without variance component estimation. The number of iterations until the results converge are a measure of the compatibility of the observations and the mathematical model. In other words, if the *a posteriori* errors in an observation group are still too large after few iterations, or the observation group does not significantly contribute to the least squares solution, the process might need many iterations, yielding a mis-modelled linear system.

**Note:** The estimation of the variance components is a time-consuming process. The normal matrix usually has a size of  $(L_{\max} + 1)^2 \times (L_{\max} + 1)^2$ , which would be in the case of the CSR dataset a  $3721 \times 3721$  matrix, if one uses the GFZ dataset a  $14641 \times 14641$  matrix, as the GFZ provides coefficients up to degree and order 120. Its iterative inversion and the computation of the redundancy numbers might thus need quite long, if e.g. a few iterations are not enough for the variance components to converge. In (Koch & Kusche, 2002), a method is discussed which avoids the inversion of  $\mathbf{N}$  and uses a stochastic trace estimation for the computation of the variance components. But such an approach is not further discussed in this work. As the following results are based on the fourth release of the CSR datasets, the maximal degree and order of the coefficients  $L_{\max} = 60$ , yielding a  $3721 \times 3721$  normal matrix. Thus, it was decided to use the straightforward method, which was discussed in this chapter.

An other often used method for an iterative update in the variance component estimation is to use an updated weight matrix  $\mathbf{P}_{i+1} = \frac{1}{\sigma_i^2} \mathbf{P}_i$  in every iteration step instead of the product of the basic weight matrix and the inverse variance component. Then, one

would iterate until the single variance components are equal to one. But as the weight factors are a good measure for the quality of the observation groups and their contribution to the overall redundancy, the upper method gives an “on the fly” impression during the computation process, as to how the different observation groups fit together and is thus preferred in this work.

## Constraining GRACE coefficients with a Kaula-type rule

4

### 4.1 Estimation of a Kaula rule for time-variable gravity

The Wiener filter and the Bayesian type regularization showed that stochastic filters need prior information about the unfiltered coefficients. In the case of a Wiener filter, such information is used as a desired output signal, whereas the regularization constrains the amplitude of the errors of spherical harmonic coefficients with an upper bound. However, it was already said that such data actually does not exist in the case of GRACE coefficients. Thus, various approaches were made in order to determine such an *a priori* signal variance (e.g. Klees et al., 2008; Kusche, 2007), which is often based on geophysical models (e.g. Seo et al., 2006; Kusche, 2007). In (Klees et al., 2008), a method was discussed which uses solely GRACE data for building the *a priori* signal variance.

A similar approach is discussed here. In (Kaula, 1966) it was mentioned that the degree variances of a spherical harmonic signal spectrum can be roughly approximated by a power law and thus decrease linearly in the logarithmic scale. This knowledge is used as stochastic *a priori* data in ill-posed systems of normal equations for static gravity field determinations, and thus constraining the solution of such a regularized least squares parameter estimation to have a finite total signal power (Bouman & Koop, 1998). Unfortunately, the Kaula rule is only defined for the static gravity field. But its power law behaviour allows a simple estimation of a fitting power law (i.e. a degree variance model) for other kinds of spherical harmonic coefficients, e.g. the time derivative of the monthly GRACE solutions. The basic equation for such a power law reads as

$$\sigma_l^2 = 10^a l^b \quad (4.1.1)$$

where

- $\sigma_l^2$  Signal degree variances
- $a, b$  unknown parameters of the power law

A power law is represented by a straight line in a log-log-graph, i.e. a first-order polynomial. Thus, (4.1.1) is transformed into the equation of a line:

$$\log(\sigma_l^2) = a + b \log(l) \quad (4.1.2)$$

Equation (4.1.2) can be used for fitting a power law to the time-variable gravity field. In order to minimize the influence of erroneous monthly solutions or random errors, it is common to approximate not the degree variances of a single monthly solution, but the mean of a time series, which can be the same month in different years (cyclostationary) or all available GRACE data (stationary):

$$\langle \sigma_l^2 \rangle = \frac{1}{N} \sum_{n=1}^N \sigma_l^2(n) \quad (4.1.3)$$

where

$N$	length of the time series
$\sigma_l^2(n)$	degree variances

The parameters of the power law are estimated by a least squares estimation:

$$\mathbf{y} = \mathbf{Ax} + \mathbf{e} \quad (4.1.4)$$

where

$\mathbf{y}$	$= \log(\langle \sigma_l^2 \rangle)$	observation vector
$\mathbf{A}$	$= [A_l] = [1 \ \log(l)]$ , $l = 2 : L_{\text{reg}}$	design matrix
$\mathbf{x}$	$= [a \ b]$	parameters of the power law
$\mathbf{e}$		residuals

and thus

$$\hat{\mathbf{x}} = (\mathbf{A}^\top \mathbf{A})^{-1} \mathbf{A}^\top \mathbf{y} \quad (4.1.5)$$

The parameter  $L_{\text{reg}}$  is the highest degree of approximation. The signal degree variances from unfiltered GRACE coefficients usually attenuate until a certain degree, after which they amplify again. Choosing  $L_{\text{reg}}$  too large would result in a only meagerly attenuating degree variance model, which would assume a too high spectral power of the higher degree coefficients. Thus, the degree variances of the signal must be approximated in the band where the signal power linearly attenuates. The upper limit of this band is given by the degree, where the signal degree variances stop decaying and start to amplify. This becomes clear, if figure 4.1 is regarded, where the maximal degree of approximation is marked with a black dashed vertical line. The lowest degree of approximation is often set to 2, as the degree 0 and 1 coefficients are defined to be zero, which is done in this work as well. On the basis of the derived formulae, power laws for different time series of 70 months of time-variable CSR-4 GRACE coefficients (see (2.2.18)) were computed, which are shown in figure 4.1. Their appropriate parameters are presented in table 4.1. It must be mentioned that the coefficients of April 2004 were excluded, as they showed completely different spectral characteristics. In figure 4.1a, the power law was estimated with coefficients from January 2003 only, whereas the other two consider the mean over a certain time period, which is the mean of all available monthly solutions for January (figure 4.1b) and the mean of all available GRACE solutions (figure 4.1c).

In figure 4.1, the degree variances of the single dataset of January 2003 differ clearly from the mean. The signal power already rises from degree 12 and, compared to the monthly and annual mean respectively, is much higher in the high frequency coefficients.

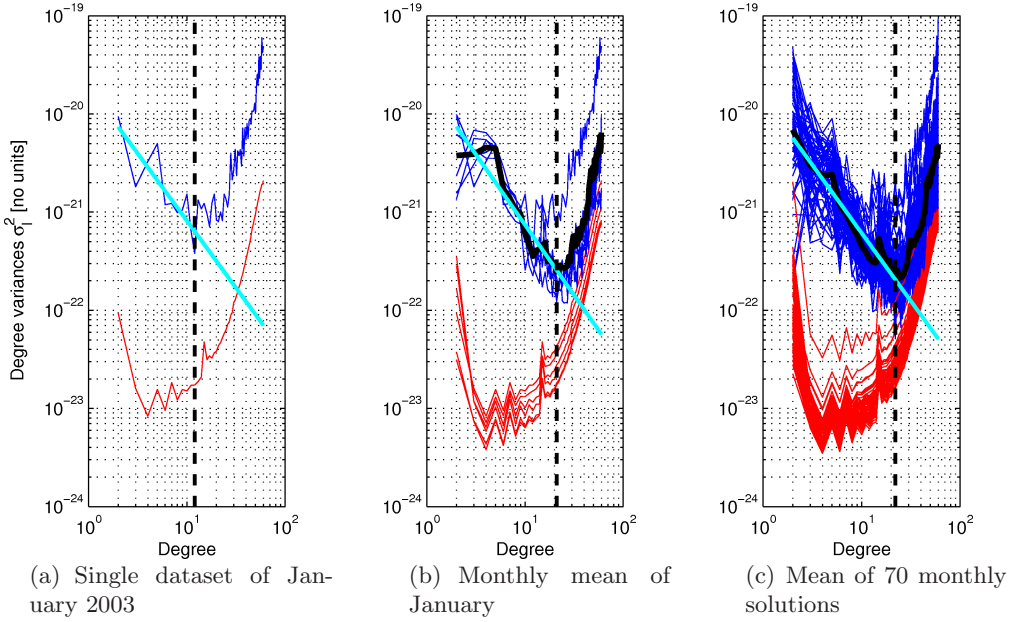


**Figure 4.1:** Signal (blue), noise (red), mean (black) and power law (cyan) degree variances of the CSR-4 coefficients

**Table 4.1:** Parameters of fitted power laws from different time series, where  $L_{\text{reg}}$  is set to the point of inflection of the signal degree variances

Data	$L_{\text{reg}}$	$a$	$b$
mean of all available data	22	-19.8283	-1.3847
monthly mean of January	21	-19.6989	-1.4311
single dataset of January 2003	12	-19.7209	-1.3670
single dataset of January 2005	26	-19.7946	-1.3740
single dataset of January 2007	28	-19.7961	-1.3580
annual mean of 2003	21	-19.9131	-1.2164
annual mean of 2005	21	-19.7097	-1.5724
annual mean of 2007	24	-19.7897	-1.4445

The other two show a decreasing power until degree 21 (monthly mean) and 22 (annual mean) respectively. An analysis of all available GRACE datasets from the fourth CSR dataset showed that these large signal degree variances are typical for coefficients from the years 2002 and 2003. This is even more obvious, if figure 4.1a and 4.1b are compared. The signal power from January 2003 is higher than the other months, especially in the high frequency coefficients. This leads to the assumption that the noise level in time-variable GRACE coefficients is not constant. From this it should follow that the estimation of a mean power law must not hold for all available monthly solutions, but

only for the regarded time series. This means that even a mean power law could change, if new data is added. But on the other hand, the parameters of the estimated power laws (see table 4.1) paint a different picture. One has to keep in mind that the power law is only defined by the parameters  $a$  and  $b$ . An approximation up to the point of inflection of the degree variances results in very similar coefficients, no matter which data is used, which agrees with the three presented power laws in figure 4.2a and table 4.1. This is actually an important effect, as the theoretical signal strength, defined by the estimated power laws, seems to be stationary, yielding a more or less constant signal strength in each single monthly GRACE solution.

However, a further interesting point would be the impact of a varying maximal degree of approximation. This would mean that the power law is mis-modelled, as it assumes a too low or too high spectral signal power. Thus, two further power laws were estimated with their maximal degree of approximation being  $L_{\text{reg}} = 12$  and  $L_{\text{reg}} = 32$  respectively, using the mean of 70 monthly CSR-4 solutions. The results are presented in figure 4.2b and table 4.2.

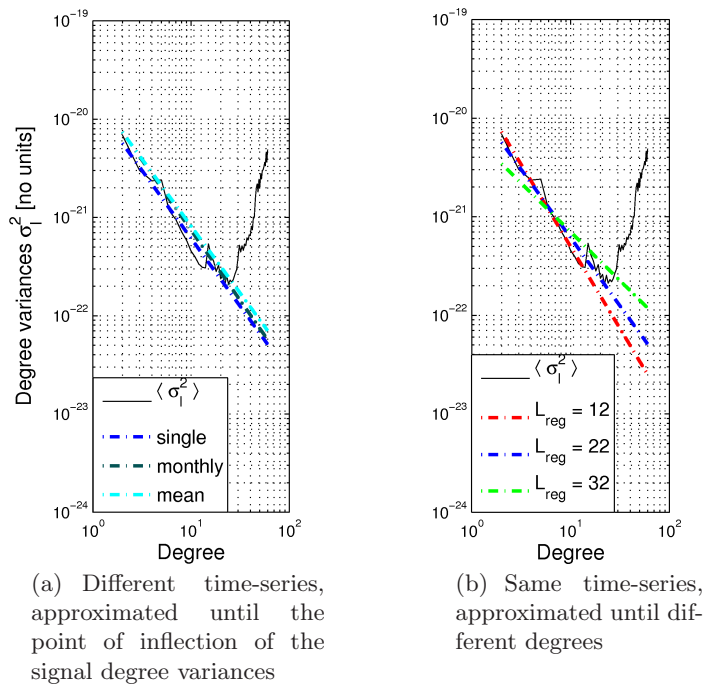


**Figure 4.2:** Comparison of different power laws

According to figure 4.2b the slope of the power law obviously changes if it is estimated within the same power spectrum, but different maximal degrees of approximation. The green power law crosses the mean signal variances after the point of inflection, assuming a too high signal power in the coefficients with high degrees. On the other side, it shows a lesser power in the low degree signal variances, which actually do not agree with the mean variances. This actually means that such a power law would constrain the low-degree coefficients with a too low signal power, whereas obviously allows a little contribution of noise in the higher degree coefficients. On the other hand, the red power law, which is only approximated until degree 12, assumes a lower signal power than

the blue power law, which was approximated until the point of inflection. This means that one would eliminate usable signal by considering it as noise (through its deviation from the power law). Thus, the following analysis will concentrate on the impact of a varying maximal degree of approximation of a mean power law. The models which were approximated until degree 12 and 32 respectively should not be considered as realistic estimates, as they would constrain the GRACE coefficients with a too smooth or too noisy power spectra, respectively.

**Table 4.2:** Parameters of fitted power laws with a varying maximal degree of approximation

Data	$L_{\text{reg}}$	$a$	$b$
mean of all available data	12	-19.6361	-1.6669
mean of all available data	22	-19.8283	-1.3847
mean of all available data	32	-20.1641	-0.9904

## 4.2 Simulation of a full covariance matrix for time-variable GRACE coefficients

The stochastic filters, both the Wiener filter and Bayesian type regularization, require a full covariance matrix of GRACE coefficients. The data centers usually provide only formal and calibrated standard deviations of the GRACE data. But it is assumed that correlations between the coefficients, represented by a full or at least block diagonal covariance matrix, have a serious impact on the filtering procedures. It was shown in different papers, (e.g. Kusche, 2007; Devaraju et al., 2008) that a full covariance matrix can be simulated according to the *energy balance approach*.

$$\begin{aligned}
 W_A - W_B &= \Delta T_{AB} \\
 \Delta T_{AB} &= \sum_{l,m}^{L,l} \Lambda_l \tilde{Y}_{lm}(\theta_A, \lambda_A) \tilde{K}_{lm} - \sum_{l,m}^{L,l} \Lambda_l \tilde{Y}_{lm}(\theta_B, \lambda_B) \tilde{K}_{lm} \\
 &= \sum_{l,m}^{L,l} \Lambda_l \left( \tilde{Y}_{lm}(\theta_A, \lambda_A) - \tilde{Y}_{lm}(\theta_B, \lambda_B) \right) \tilde{K}_{lm} \\
 &= \sum_{l,m}^{L,l} \Lambda_l \Delta \tilde{Y}_{lm} \tilde{K}_{lm} \\
 \Delta T_{AB} &= \mathbf{Y} \Lambda \mathbf{K} \Rightarrow \mathbf{Q}_S = (\Lambda^T \mathbf{Y}^T \mathbf{Y} \Lambda)^{-1}
 \end{aligned} \tag{4.2.1}$$

where

- $W_{(.)}$  Potential observed by the satellites GRACE A and B
- $\Delta T_{AB}$  Difference in disturbing potential

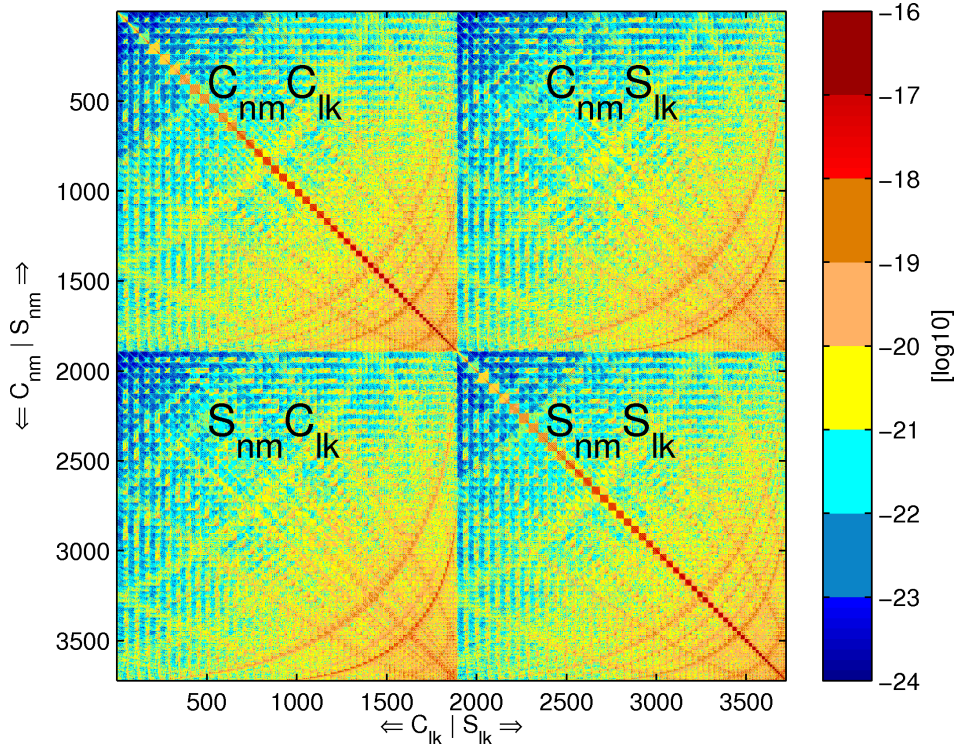


**Figure 4.3:** Simulated full covariance matrix for GRACE coefficients

- $\tilde{Y}_{lm}, \mathbf{Y}$  Surface spherical harmonics,  $\mathbf{Y}$  contains  $\Delta\tilde{Y}_{lm}$
- $\tilde{K}_{lm}, \mathbf{K}$  Spherical harmonic coefficients
- $\Lambda_l, \Lambda$  Isotropic transfer coefficients, and
- $\mathbf{Q}_S$  Simulated covariance matrix

One has to keep in mind that  $\mathbf{Q}_S$  represents the covariance matrix for pure monthly GRACE coefficients, but in this work, the simulated covariance matrix must be differentiated as well. This happens again according to the presented formula of central differences introduced in section 2.2.2, but with consideration of the covariance propagation law:

$$\mathbf{Q}_G = \frac{1}{4}(\mathbf{Q}_S(t+1) + \mathbf{Q}_S(t-1)) \quad (4.2.2)$$

The presented full covariance matrix in figure 4.2 is simulated with data for January 2003. It is arranged orderwise for an easier computation process. Obviously, it has a very strong block diagonal characteristic. Thus, there are indeed strong correlations within the blocks, i.e. the coefficients with the same order. On the other hand, coefficients with the same degree and different order are less correlated. These characteristics agree with the assumption from Han (2003) that the block diagonal structure approximates a full covariance matrix with satisfactory accuracy, especially in the case of spherical harmonic coefficients from GRACE. Kusche (2007) found the maximum correlation of 0.89 in a block for order  $m = 34$  (degrees 38 and 40), whereas the maximum correlation across the order blocks is much less with 0.07 for degree/order 18/15 and 61/61.

However, there are obviously correlations between tesseral coefficients. Thus, in this thesis the presented methods are tested with different kinds of covariance matrix structures to observe the impact of correlations. On the basis of these formulae, full covariance matrices for January 2003, May 2005 and September 2006 are simulated. In order to use such a matrix in the computation process, the magnitudes of the simulated matrix and the coefficients from the data centers themselves must agree. Therefore, the simulated covariance matrices are scaled by multiplying  $\mathbf{Q}_G$  with the ratios of the outer products of the formal errors from the data centers and the standard deviations from the simulated matrices (i.e. the square root of their main diagonal elements).

### 4.3 Using a Kaula-type rule as stochastic constraint in a sequential estimation

It was mentioned in section 3.3.2 that a degree variance model can be used as *a priori* information about Stokes coefficients, which is usually done in the context of regularization of ill-posed systems of normal equations in satellite geodesy. In this work, such a model, which was estimated according to the formulae in section 4.1, is used as a stochastic constraint for an upper limit of the errors in monthly time-variable GRACE solutions. Thus, the squared inverse RMS-values of such a power law are stored in a diagonal matrix for both cos- and sin-part of the spectrum:

$$K_{lm}^C = \frac{\sigma_l^2}{2l+1}, \quad l = m, m+1, \dots, L, \quad m = 0, 1, \dots, L \quad (4.3.1a)$$

$$K_{lm}^S = \frac{\sigma_l^2}{2l+1}, \quad l = m, m+1, \dots, L, \quad m = 1, 2, \dots, L \quad (4.3.1b)$$

**Remark:** The signal variances  $\sigma_l^2$  in equations (4.3.1a) and (4.3.1b) should not be mistaken for the pure signal degree variances from the GRACE coefficients, which are denoted by  $\sigma_l^2$  as well. In this context here, the values are given by the estimated power laws from section 4.1.

Afterwards, these submatrices are combined in a diagonal  $(L+1)^2 \times (L+1)^2$  *a priori* variance matrix:

$$\mathbf{Q}_K = \begin{pmatrix} \mathbf{K}^C & 0 \\ 0 & \mathbf{K}^S \end{pmatrix} \quad (4.3.2)$$

The inverse of this matrix  $\mathbf{P}_K = \mathbf{Q}_K^{-1}$  is used as regularization term in the derived formulae from section 3.3.2:

$$\hat{\mathbf{x}} = (\mathbf{P}_G + \lambda \mathbf{P}_K)^{-1} \mathbf{P}_G \mathbf{y} \quad (4.3.3)$$

where  $\mathbf{P}_G$  is the inverse of the simulated covariance matrix from section 4.2 and  $\mathbf{y}$  is a vector of monthly GRACE coefficients. In a first step the regularization parameter  $\lambda = 1$ , giving both observation groups an *a priori* weight defined by  $\mathbf{P}_G$  and  $\mathbf{P}_K$  respectively.

### Spectral domain

The regularized spectra are analyzed first, as the regularization of the time-variable GRACE coefficients happens in the spectral domain. Here, the degree variances of signal and error are introduced as a measure of the total signal and noise content per degree in the regularized coefficients.

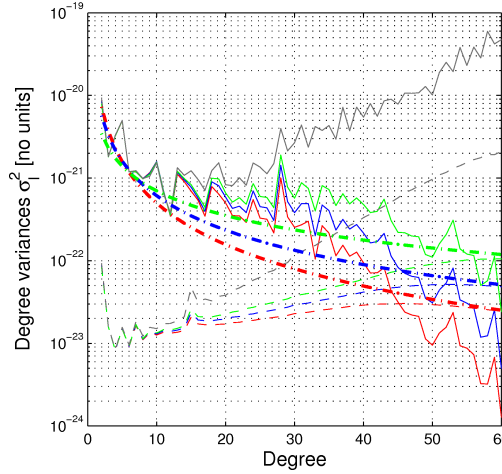


**Figure 4.4:** Degree variances of signal (thin solid line), noise (dashed line) and power law (bold dash dotted line), where the power law was approximated until  $L_{\text{reg}} = 12$  (red),  $L_{\text{reg}} = 22$  (blue) and  $L_{\text{reg}} = 32$ . The GRACE coefficients and errors before regularization (grey) are plotted as reference.

Figure 4.4 shows that regularization successfully forces the spectral signal power to decrease with increasing degree. Moreover, it holds that the coefficients until degree 13 are not influenced by the regularization term, as the signal degree variances agree in this band with the approximated power law. Additionally, it shows an important characteristic of the regularized spectrum. The relative magnitude of the degree variances is not influenced, which means that information about small scale features, which are hidden in high frequency coefficients, are not eliminated by regularizing, but the signal power of the appropriate coefficients is drastically decreased. This happens differently, depending on the used power law. The green power law, which was approximated until a degree after the point of inflection of the mean signal variances results in a higher spectral power of signal and noise. Moreover, the degree variance curves diverge with increasing degree, which means that the regularized Stokes coefficients differ especially in the high frequency part of the spectrum.

Unfortunately, figure 4.4 also shows that even if the regularized error spectrum tends to converge with the power law, the signal degree variances possess a spectral power still too high, which is most obvious for degree 28. This indicates that the influence of the regularization term on the noisy GRACE coefficients was not strong enough to reduce the signal strength to a realistic level.

The spectral redundancy contribution (see equation (C.6) in the appendix) in figure 4.5 yields the percentage impact of the regularization term on each single regularized Stokes coefficient. It becomes clear that the regularization term mainly influences the

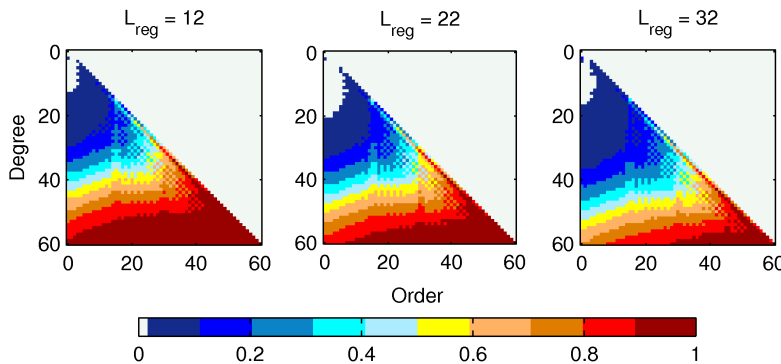


**Figure 4.5:** Redundancy contribution of the regularization term in the spectral domain

high frequency coefficients, as the unfiltered coefficients with small degree and order agree with the estimated power law. Furthermore, the contribution of the regularization term to the estimated parameters increases with increasing order. The sectorial coefficients are seriously influenced by degree and order 20. This effect comes from the isotropic nature of an estimated degree variance model, which constrains the pure GRACE coefficients in two ways. It primarily makes the spectral signal power to attenuate with increasing degree by keeping the noise degree variances under the upper bound, given by the power law. This happens mainly by decreasing the power in the near sectorial and sectorial part of the spectrum, as unregularized coefficient show a high spectral power density in this section.

### Spatial domain

The high spectral power in the sectorial and near sectorial coefficients caused an unrealistic spatial signal strength, represented by the massive north-south stripes. By attenuating the power of this part of the spectrum, one would theoretically decrease the amplitude of the north-south stripes, which agrees with figure 4.6, where the regularized coefficients were transformed into a rate of change in terms of water equivalent heights according to equation (2.2.18).

It is obvious that regularizing drastically scales down the magnitude of the signal-power in the high frequency coefficients, which was already expected from the signal degree variances in figure 4.4. This agrees with the derived statistics from the maps, presented in table 4.3, as well. Although the north-south stripes are still visible, these artifacts have a much lower amplitude, which makes features visible, if e.g. South America is considered. As the Amazon basin is one of the regions with the largest mass-fluctuations due to hydrological effects, it was assumed that there will be a strong signal, which is clearly visible in all three solutions. But there is a relatively high signal strength in the equatorial regions compared to the overall signal, which is an effect of the high signal power in the sectorial and near sectorial coefficients as well.

The differences of the solutions, visualized in figure 4.6, show that the maximal degree of approximation of the used power law controls the strength of regularization. This becomes clear if figure 4.4 is taken into focus again. A steep power law yields a lesser signal strength after regularizing. This assumption is emphasized by the derived

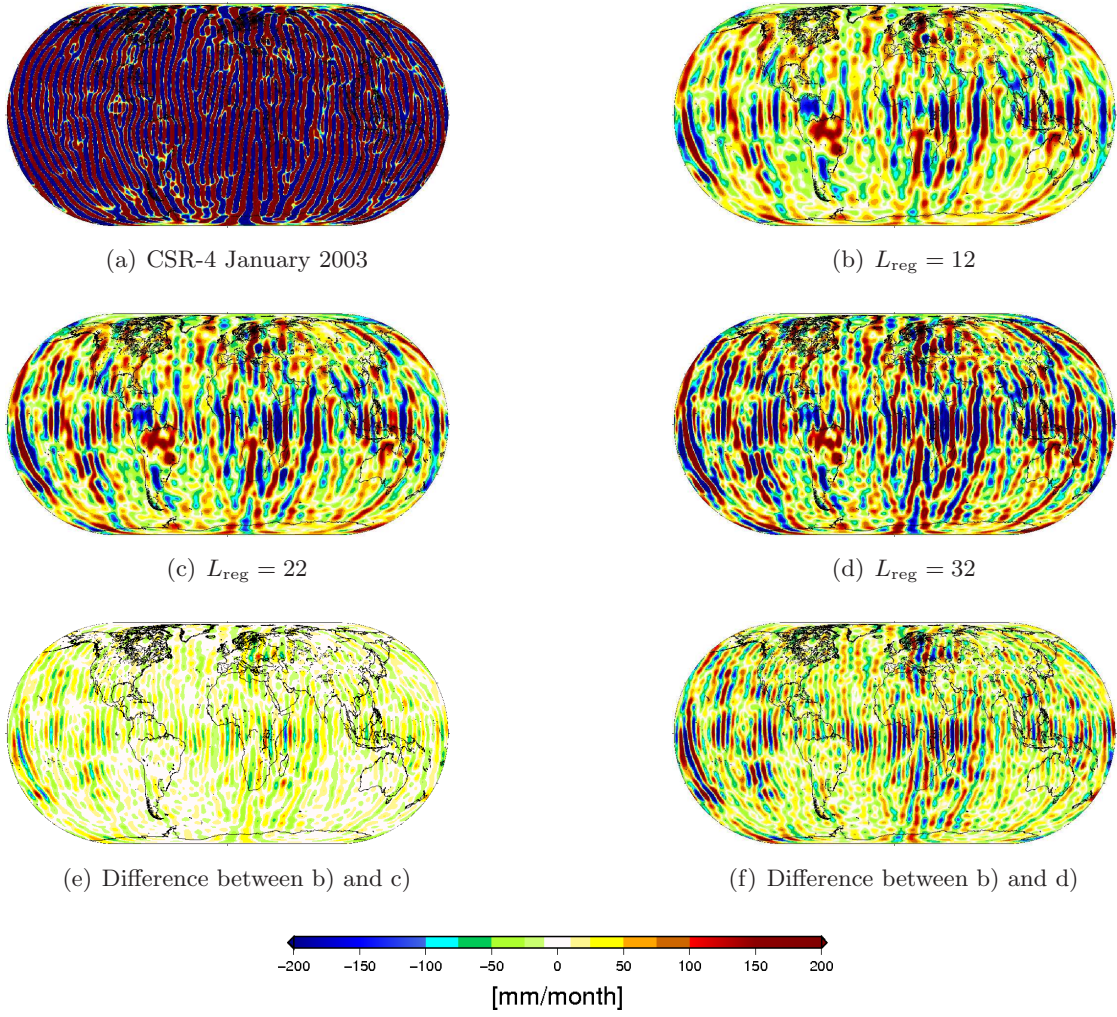


**Figure 4.6:** Derived maps in rate of change equivalent water heights for January 2003, computed from GRACE coefficients before and after regularizing

statistics in table 4.3. Even if the mean values of all three regularized fields are similar, the RMS is drastically reduced if a steep power law is used as constraint. Thus, the power law, used as a regularization term, has a similar function than e.g. the Gaussian averaging radius, but is less illustrative: using a steep power law results in a heavier filtered field, whereas a smoothly attenuating power law is similar to a small Gaussian averaging radius, yielding a less filtered field.

## 4.4 The efficiency of the regularization with estimated weight factors

### 4.4.1 The impact of different power laws as stochastic constraints

The results in section 4.3 were still contaminated with noise, even if the signal strength of the stripes was drastically reduced. However, the variance component estimation from

**Table 4.3:** Statistics of the derived maps from figure 4.6

field	RMS	mean	min	max
[mm/month]				
unfiltered	783.824	2.563	-4982.904	5315.985
filtered with $L_{\text{reg}} = 12$	64.978	2.410	-427.613	424.141
filtered with $L_{\text{reg}} = 22$	82.034	2.404	-601.839	573.938
filtered with $L_{\text{reg}} = 32$	110.823	2.273	-885.387	819.804

section 3.3.2 is a method to increase the contribution of a observation group in a linear model, if it has smaller variances than the other group. Figure 4.4 showed that the signal strength of the GRACE coefficients is still to high, especially in the higher degrees. The variance level of the regularization term is defined by the power law, which assumes in all three cases  $L_{\text{reg}} = 12, 22$  and  $32$ , a lower signal power than the regularized solutions. Thus, estimating variance components should increase the weight of the regularization term.

The convergence criterion was set to

$$\left| 1 - \frac{\sigma^2(i)}{\sigma^2(i-1)} \right| < 10^{-5} \quad (4.4.1)$$

which must hold for both the GRACE coefficients and the regularization term.

### Spectral domain

The variance components converged for all three versions, i.e.  $L_{\text{reg}} = 12$ ,  $L_{\text{reg}} = 22$  and  $L_{\text{reg}} = 32$  respectively, after seventeen ( $L_{\text{reg}} = 12$ ) and sixteen ( $L_{\text{reg}} = 22, 32$ ) iterations. The appropriate weight factors for the GRACE coefficients and the regularizing term are presented in table 4.4 and figure 4.7.

**Table 4.4:** Estimated variance components of the different regularization terms

$L_{\text{reg}}$	$1/\sigma_G^2$	$1/\sigma_K^2$	$\lambda = \sigma_G^2/\sigma_K^2$
12	0.071	1.232	17.275
22	0.071	1.627	22.750
32	0.071	2.061	28.773

The estimated weight factors for both observation groups agree with the assumption that the contribution of the Kaula matrix should be increased through the VCE, as it gained more weight than the GRACE coefficients in all three cases. Moreover, the inverse variance components are very similar for the GRACE coefficients, even if the influence of the Kaula matrix differs. The different weight factors for the regularization matrices

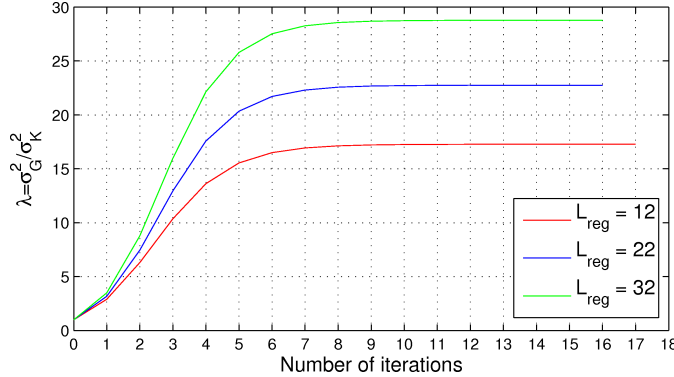


**Figure 4.7:** Value of the regularization parameter  $\lambda$  after each iteration for different regularization terms

come from the characteristics of the used power laws. If  $L_{\text{reg}} = 32$ , the group needs more weight to seriously influence the spectral signal power to attenuate with increasing degree. On the other hand, the power law with  $L_{\text{reg}} = 12$  constrains the GRACE coefficients stronger, and needs thus less weight. One has to keep in mind that the regularization term expects the coefficients to vary around zero. Thus, the steeper the attenuation of the power law, the less the weight is needed to bring the estimated coefficients on that level.

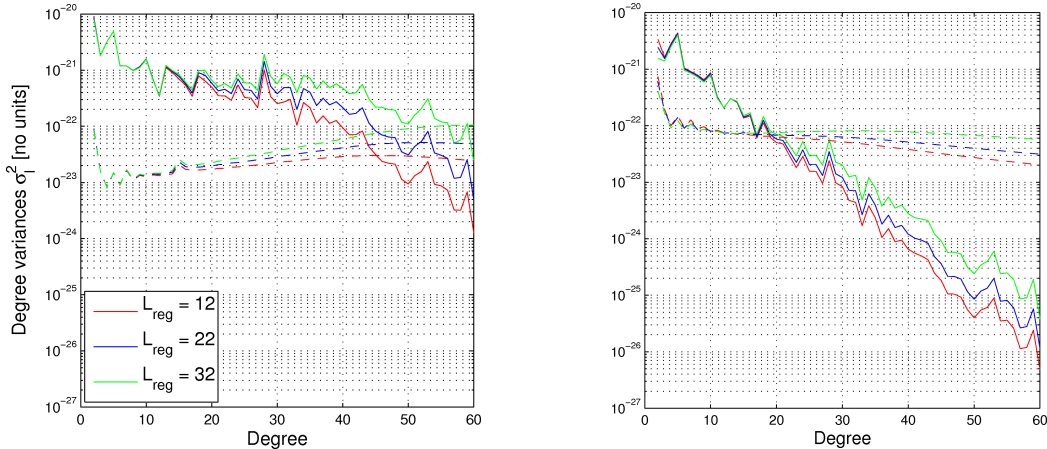


**Figure 4.8:** Comparison of the spectral signal (solid line) and noise power (dashed line) of the regularized coefficients with  $L_{\text{reg}} = 12$  (blue),  $L_{\text{reg}} = 22$  (red),  $L_{\text{reg}} = 32$  (green) before (left) and after (right) VCE

More about the characteristics of the regularized coefficients can be told from the signal and error spectrum, presented in figure 4.8, where all three versions are plotted against their unweighted counterparts. Through the weighting with the estimated variance components the regularization term has attenuated the spectral signal power of the high frequency coefficients. This is trivial as regularization assumes the coefficients to be zero, with respect to the variances from the regularization matrix, which is the expected effect of an unbiased regularization with zero observations. The relative magnitude of the three versions in figure 4.8 show similar characteristics with and without estimated variance components. This again emphasizes that the used power law can be compared

to an averaging radius, which is used for deterministic filters. However, the errors in the regularized solution are bigger than the appropriate signals from degree 20. This is actually an effect of the regularization technique. The *a priori* noise level of the GRACE coefficients, represented by the main diagonal of the simulated covariance matrix, is increased by adding the regularization term. If one thinks of the inverse proportionality of its elements to a degree variance model, it becomes clear that the elements get bigger with increasing degree and order, whereas the elements of the inverse covariance matrix of the GRACE coefficients, i.e. the weight matrix, attenuate with increasing order and degree, which yields usually lesser weight to these coefficients with low accuracy. But through regularization, the errors in the high frequency part of the spectrum gain more influence in the linear model. This effect becomes clearer in figure 4.9.

Initially, the signal strength is overall higher than the errors. This holds even after regularization without estimated variance components (cf. figure 4.8). But as the high frequency errors are increased through regularization, the signal is stronger constrained than the noise. The *a priori* error degree variances cross the modelled degree variances at degree 30. If the spectral redundancy contribution is regarded again, it becomes evident that the regularization term starts to dominate the solution in this part of the spectrum. After regularizing, the noise is bigger than the signal from degree 20, which actually means that, according to Kaula's rule, the signal beyond degree 20 contains a signal-to-noise-ratio  $SNR_l < 1$  and is thus dominated by noise.

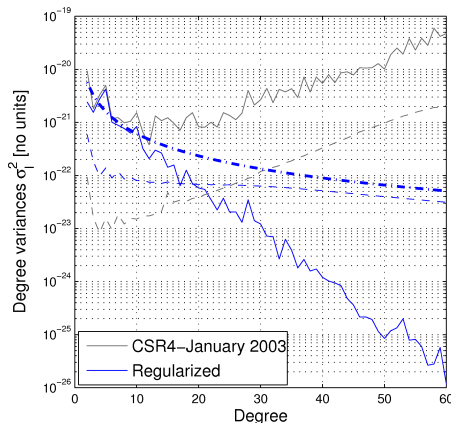


**Figure 4.9:** Signal (solid lines), noise (dashed lines) and modelled (bold dash dotted line) degree variances of the GRACE coefficients before and after regularizing with the mean power law approximated until  $L_{\text{reg}} = 22$

This is a very important effect of the regularization. Kaula's rule is used to roughly approximate an upper bound for the error degree variances of Stokes coefficients. The latter observations showed that the coefficients with  $l > 20$  contain more noise than useable signal. This actually means that GRACE delivers only noisy time-variable information from degree 20, if one uses the estimated power law as degree variance model. This maximal degree yields a spatial resolution of about 1000 km of half wavelength<sup>1</sup>. These findings agree with those found by Klees et al. (2008), as they state that a distinction between true mass variations and errors in areas smaller than  $10^6 \text{ km}^2$  is not possible.

<sup>1</sup>spat. resolution [km]  $\approx U/2L$  where  $U = 2\pi R$  is the circumference of the earth

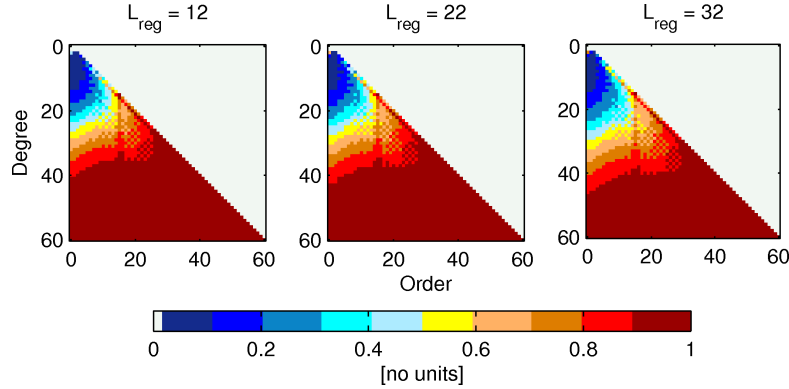


**Figure 4.10:** Spectral redundancy contribution of the regularization term

The spectral redundancy contribution (cf. figure 4.10) agrees with the assumption that the estimation of weight factors increases the influence of the regularization term on the GRACE coefficients. In the first case, where no VCE was applied, the regularization matrix affected only these coefficients with their degree being larger than 40. Now, the power law already has an impact on zonal coefficients with  $l > 25$ . Moreover, the influence increases with increasing order, which is a logical consequence if the spectrum of unfiltered GRACE coefficients is regarded (cf. figure 4.11). The zonal and near zonal coefficients show an almost constant signal power, which seriously increases in the near sectorial and sectorial part. As the regularization technique constrains the signal strength to attenuate with increasing degree, the regularization matrix has to impact exactly on this part of the signal which causes the high signal strength. Additionally, there is a distinct contribution to the near sectorial coefficients with  $m = l - 1$  recognizable, dominating the solutions from degree 8.

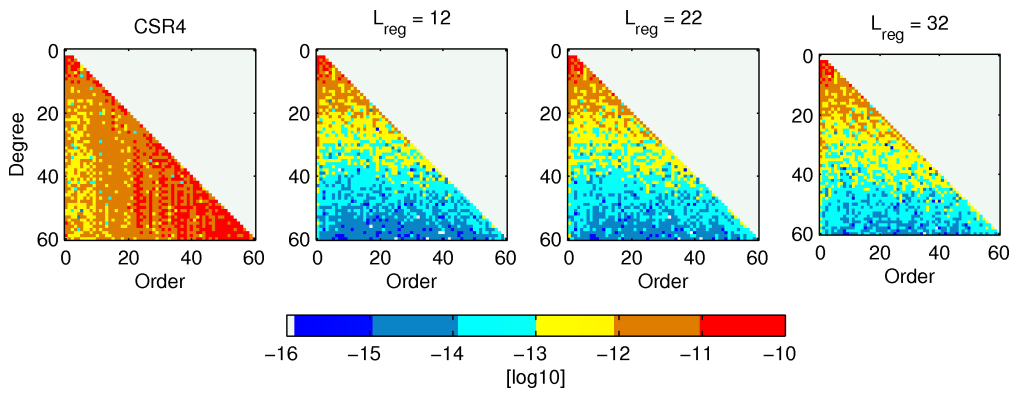


**Figure 4.11:** GRACE coefficients before and after regularization

Figure 4.11 shows the GRACE coefficients before and after the regularization. The unregularized coefficients possess a stronger dependency from their order than from their degree, which is counteracted by the isotropic nature of the constraining power law. Thus, all three regularized spectra show on the one hand a drastically decreased signal power and on the other hand a more or less isotropic characteristic. But the degree variances in figure 4.8 already showed a slight difference in the regularized coefficients,

which is visible here again. The steeper the chosen constraining power law, the lower becomes the signal power in the high frequency coefficients.

### Spatial domain

If these coefficients are used to derive fields of water equivalent heights per month, it becomes obvious that an increased weight of the regularization term eliminated most of the noisy artifacts (cf. figure 4.12). All three maps show distinct areas with a high signal strength in South- and Central America or South and Central Africa. These areas are completely independent from the initially noisy structures, which were spread over the whole globe, as they possess different spatial characteristics. Over the oceans, especially in the northern Pacific, there are slight signals visible, as well as in Northern Africa or Russia. Due to the spatial characteristics of these large-scale signals, one might assume that these do not come from errors in the GRACE coefficients, but should be caused by changes in the earth's gravity field. This holds, even if there are still some stripy artifacts visible, especially in the equatorial regions. In contrast to the signals in the near-polar oceanic regions, the artifacts in the equatorial pacific and northern Indian ocean might come from remaining errors in the GRACE coefficients, as they possess stripy shapes, with their maximal amplitude being near the equator.

However, the statistics in table 4.5 agree with the latter positive findings. The maximal and minimal value can be recognized in Central and South America with a signal strength about  $-130 \text{ mm/month}$  (Venezuela) and  $150 \text{ mm/month}$  (Amazon basin) in all three regularized fields. Thus, figure 4.12 and table 4.5 show another interesting effect of the regularization of time-variable GRACE coefficients. Even if the regularized spectra (cf. figure 4.8) varied in the high frequency part, the derived maps show nearly no visible differences: the deviations in the spectral domain are negligible when propagated to the spatial domain. This can be explained by the fact that remaining differences usually have such a low spectral signal power. The unweighted solutions already showed that the differences between the derived maps are mainly caused by differences in the high frequency part of the spectrum. And exactly this part is now drastically attenuated, which yields the slight deviations between the maps in figure 4.12.

**Table 4.5:** Statistics of the derived maps from figure 4.12

field	RMS	mean	min	max
[mm/month]				
filtered with $L_{\text{reg}} = 12$	25.7	0.3	-129.6	149.8
filtered with $L_{\text{reg}} = 22$	26.2	-0.2	-129.6	151.2
filtered with $L_{\text{reg}} = 32$	27.5	-0.8	-129.6	152.6
Difference between a) and b)	2.3	0.5	-14.9	14.8
Difference between a) and c)	5.8	1.1	-41.1	41.4

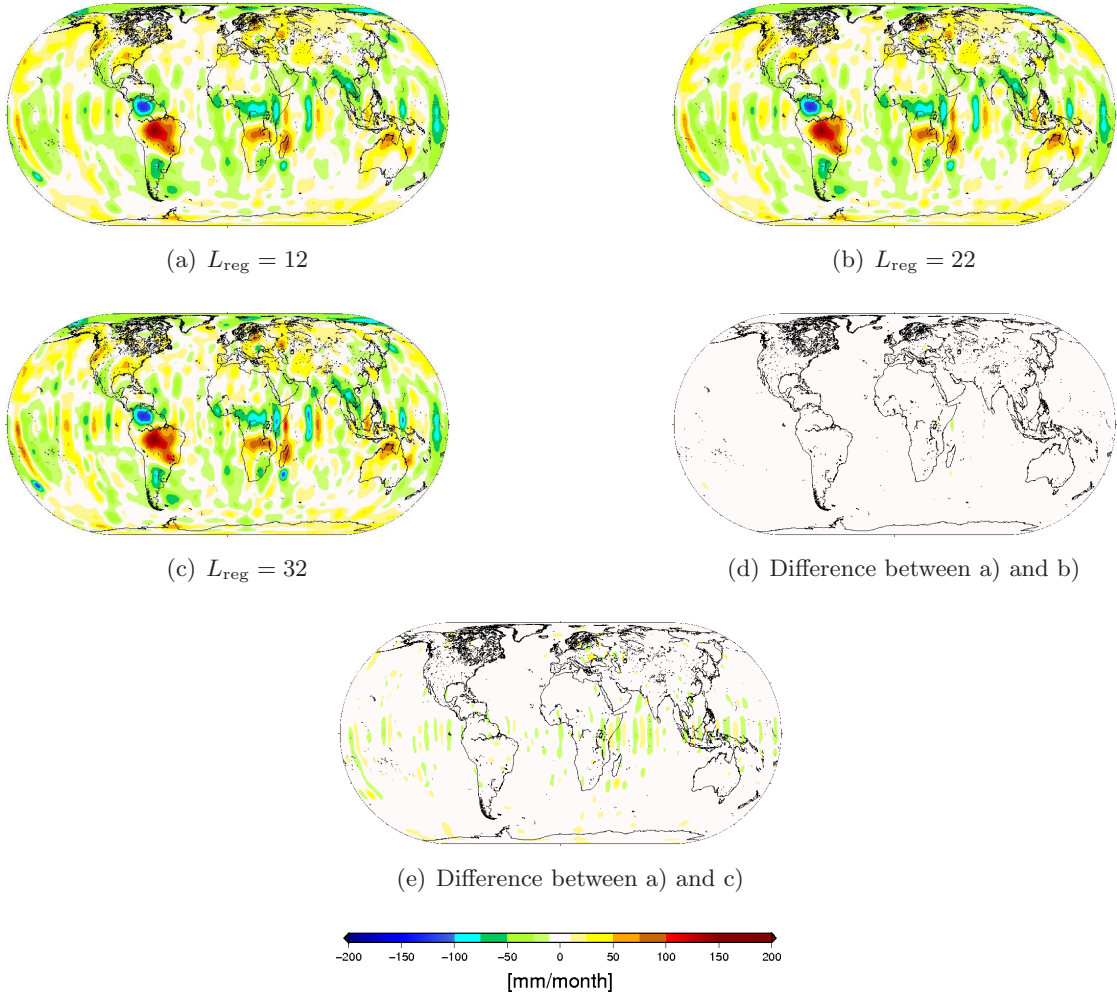


**Figure 4.12:** Regularized coefficients with VCE, transformed to changes in equivalent water heights for January 2003

In figure 4.13 the difference between a derived map with and without estimated variance components is presented. Obviously, the increased weight has its biggest impact on equatorial regions. This is actually again an effect of the power-law regularization. Without the VCE, the regularization term mainly influenced high frequency near sectorial and sectorial coefficients. On the other side, the spectral redundancy contribution after using estimated variance components showed that there is an increased contribution in the higher degree ( $l > 25$ ) zonal and the degree 2 coefficients as well. Such a stronger constraint in these parts of the spectrum explains the decreased signal strength in the equatorial regions.

Figure 4.13 shows another noticeable characteristic of both derived maps. If e.g. the Amazon basin is considered, there is only a slight signal loss after the proper weight factors were applied, even if the overall signal strength in the equatorial regions is drastically reduced. This comes from two effects of increasing the weight of the regularization term. On the one hand, the regularization technique has a decorrelation effect (that will be analyzed in a following section), which successfully removes the north-south stripes.

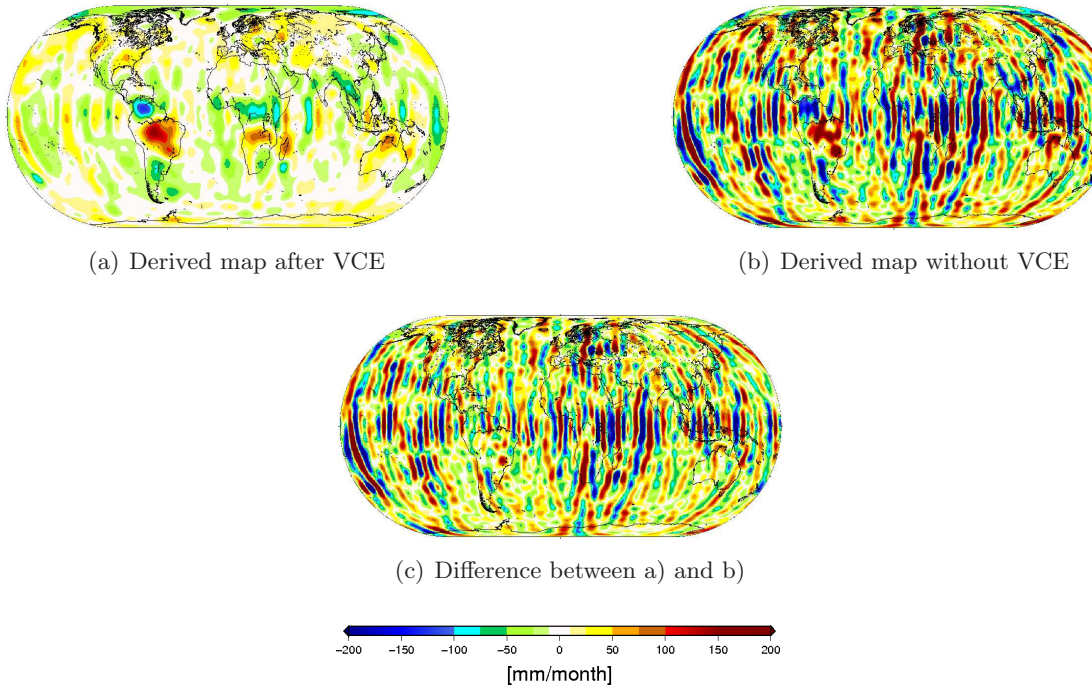


**Figure 4.13:** Visualized difference between the regularized solution with and without estimated variance components

On the other hand, the deviations between both maps are mainly caused by differences in the high frequency part of their appropriate spectrum. This can be told from the spatial characteristics of the differences, as they are mainly narrow north-south stripes which is obvious especially in the equatorial regions.

#### 4.4.2 The regularization filter with different covariance matrix structures of the GRACE solutions

The regularization filter was designed with a full covariance matrix for the spherical harmonic GRACE coefficients. However, it was already discussed in section 4.2 that such a matrix has a strong block diagonal structure. It is widely believed that a full covariance matrix can be well approximated by a block diagonal matrix, which considers correlations between coefficients of the same order, but not of the same degree. This holds especially for spherical harmonic GRACE coefficients. In figure 4.14 the simulated error covariances of the cos-coefficients up to degree and order 21 are presented to emphasize these assumptions. Therefore, a block diagonal matrix and diagonal matrix of GRACE errors are computed according to the already discussed energy balance approach. These matrices are further used as prior error estimates for the time-variable GRACE coefficients. It is assumed that the variance component estimation can be used to perform a quick and reasonable comparison between the impact of different covariance matrix structures.

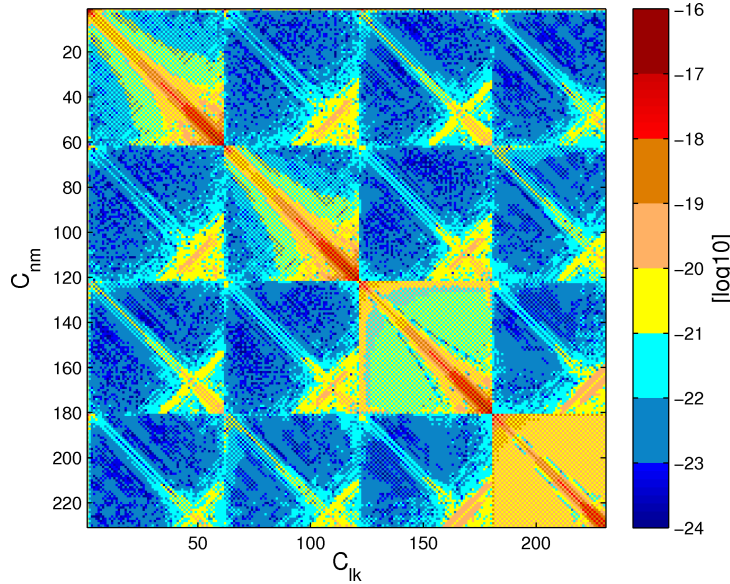


**Figure 4.14:** Covariance matrix of the cos-coefficients with  $l, m = 0, 1, 2, \dots, 21$

### Spectral domain

The VCE converged after 16 iterations for all three covariance matrices. The estimated weight factors are presented in figure 4.15 and table 4.6. Using a full and a block diagonal covariance matrix yields very similar variance components and thus a similar contribution of the regularization term.

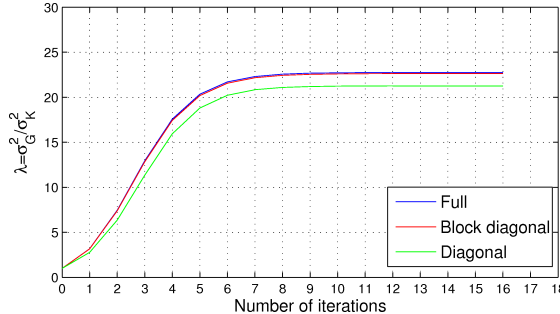


**Figure 4.15:** Convergence of the parameter  $\lambda$  for different covariance matrix structures

**Table 4.6:** Estimated variance components using different covariance matrix structures

Covariance matrix	$1/\sigma_G^2$	$1/\sigma_K^2$	$\lambda = \sigma_G^2 / \sigma_K^2$
full	0.071	1.627	22.750
block diagonal	0.071	1.616	22.630
diagonal	0.072	1.533	21.262

On the other hand, the diagonal variance matrix causes slight differences compared to the other two solutions, giving less weight to the regularization term. But these differences should be negligible when compared with the weight factors in table 4.4.

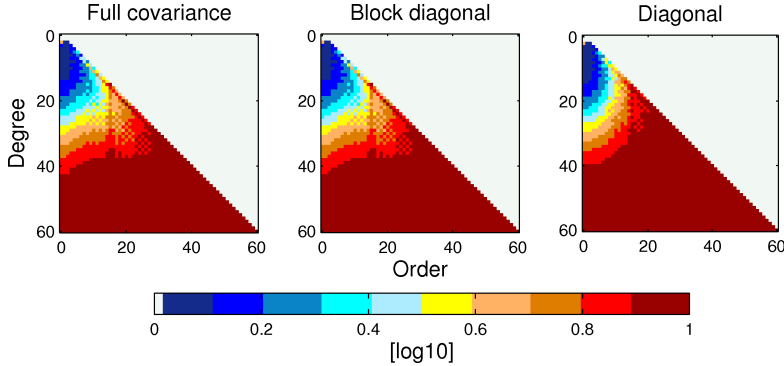


**Figure 4.16:** Spectral redundancy contribution of the regularization term, using different covariance matrix structures of GRACE errors

Again, the contribution of the stochastic constraints is analyzed with the spectral redundancy contribution (cf. figure 4.16). The regularization matrix contributes to the solutions in all three cases especially in the zonal coefficients with  $l > 30$  and  $l = 2$ , even if using only variance information yields a larger contribution from order  $m > 17$ . Moreover, the sectorial coefficients are influenced from degree and order  $l, m > 8$ , which is not the case for the full and block diagonal covariance matrix. However, one has to keep in mind that using variance information about the GRACE coefficients gives less weight to the regularization matrix, whereas its contribution in the spectral domain is larger, compared to the solutions which consider correlations between the coefficients.

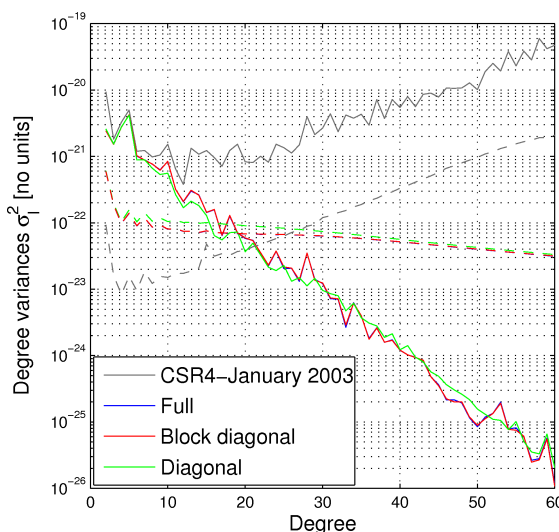


**Figure 4.17:** Signal (solid line) and noise (dashed line) degree variances of unregularized and regularized spectra, using different covariance matrix structures of GRACE errors

The similarities between the consideration of the different covariance matrix structures holds for the regularized signal and error degree variances as well. Again, the full and block diagonal covariance matrices cause equal spectral signal and noise power, both blue and red lines are congruent in figure 4.16. Using only variances result in slightly larger *a posteriori* error degree variances and smoother signal degree variances. These findings indicate that there are indeed correlations between coefficients with the same order. But considering correlations between the coefficients with the same degree does not seem to have any impact.

### Spatial domain

Propagation of the filter operators to the spatial domain yields the averaging characteristics for a certain point in space. As the regularization filter is designed as anisotropic vector operator, such a propagation must be done for different latitudes, as the filtering characteristics might change with their position. The distance from the Kernel center is computed across the  $\lambda = 90^\circ$ -meridian for the north-south sections and across the appropriate parallels  $\theta = 90^\circ, 60^\circ, 30^\circ$  for the east-west sections to maintain a proper scale between both N-S and E-W cross sections.

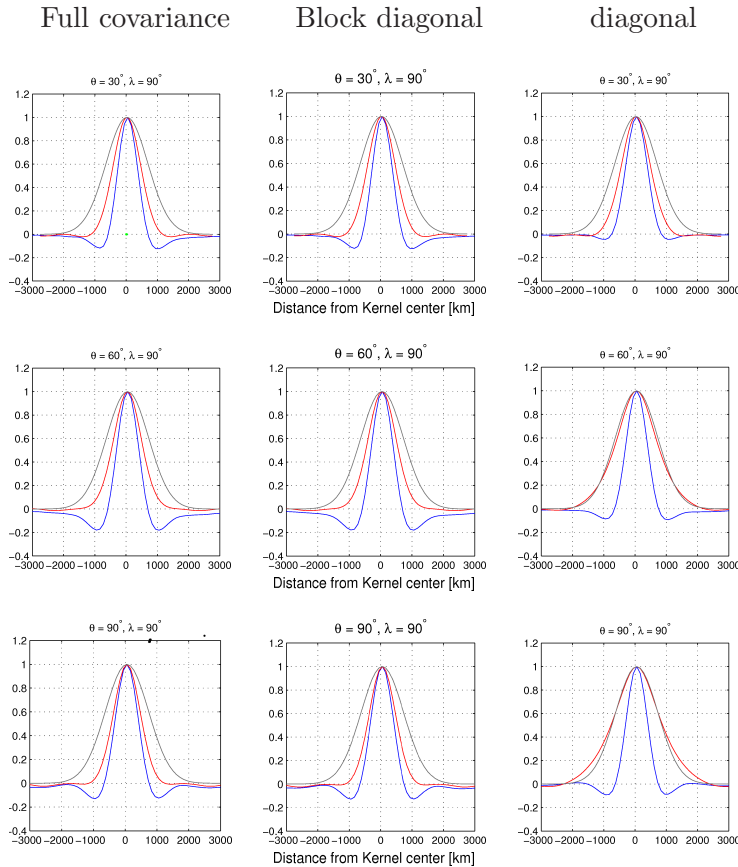


**Figure 4.18:** North-south (blue) and east-west (red) cross sections of the normalized regularization filter kernels, computed at  $\lambda = 90^\circ, \theta = 30^\circ$  (top row),  $\lambda = 90^\circ, \theta = 60^\circ$  (middle row),  $\lambda = 90^\circ, \theta = 90^\circ$  (bottom row). The isotropic 800 km Gaussian filter (gray) is given as reference

According to the cross sections in figure 4.18 all kernels are tighter in longitude direction, yielding lesser smoothing and thus a higher spatial resolution. This effect comes from the error structure in the GRACE covariance matrix (Kusche, 2007). Additionally, they possess more or less distinct negative sidelobes, which gives these regions a negative weight in the convolution process: the field which is correlated in N-S direction due to track direction is decorrelated (Kusche, 2007). This means that both types of the regularization operator remove the erroneous north-south stripes in the unfiltered field. These stripes usually change their phase in east-west direction. A decorrelating kernel smoothes the field in this direction similar to a Gaussian filter, i.e. the off-phase regions, but weight the adjactend in-phase regions negatively. But even if the kernels are based on the regularization filter, they differ especially with changing latitude. Using variances only yields a stronger smoothing in E-W direction in equatorial and mid-latitude regions, while the operator tends to isotropy in near polar regions (i.e. both east-west and north-south cross section are equal). Moreover, the east-west cross section is very similar to the 800 km Gaussian operator. The regularization kernel with full and block diagonal covariance information seems to be more or less independent from its position, as its spatial characteristics change only slightly in the N-S direction.

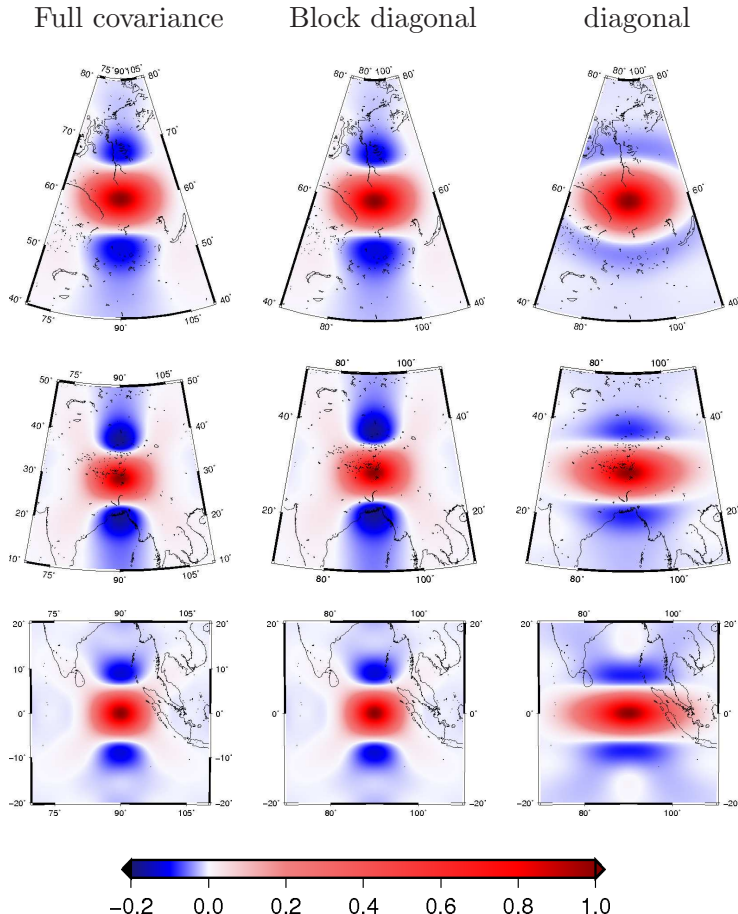


**Figure 4.19:** Propagated regularization filter Kernels at  $\lambda = 90^\circ, \theta = 30^\circ$  (top row),  $\lambda = 90^\circ, \theta = 60^\circ$  (middle row),  $\lambda = 90^\circ, \theta = 90^\circ$  (bottom row), using different covariance matrix structures

A better overview of the discussed kernels is given in figure 4.19, which emphasizes the independence of the full covariance regularization kernel from its position in space, even if the near polar regions are more strongly smoothed in longitude direction. Using variances only results in a latitude dependent kernel, which has a very elliptic shape in the near polar regions.

Moreover, figure 4.19 clearly shows that using a full or block diagonal covariance matrix does not change the filtering characteristics significantly. Both kernels possess similar spatial characteristics, whereas the smoothing radii of the variance matrix kernels are generally larger. This will lead to a heavier filtered field, i.e. the maximal amplitudes will be smaller, compared to the full or block-diagonal matrix kernel. This actually means that using a full and block-diagonal matrix leads to a better spatial resolution of the filtered field. Using only variances reduces the spatial resolution especially in longitude direction due to the elliptic shape of the kernel.

These findings hold for derived maps in terms of rate of change of water equivalent heights as well (cf. figure 4.20). Even if the regularization with full and block-diagonal covariance information yield an equal result, using a variance matrix shows other signal patterns. This holds especially for the equatorial (e.g. eastern Pacific) and near polar oceanic regions (e.g. northern Atlantic). Additionally, the overall signal strength is slightly attenuated. This is obvious in e.g. South and Middle America, where figures 4.20a and 4.20b show a signal of about 150 mm/month in the Amazon basin, which is not reached in 4.20c. However, there are larger artifacts visible in the polar regions, whereas the mid-latitude structures are stretched in longitude direction.

But in spite of these differences, the spatial characteristic of the signal patterns over land are very similar, even if the signal strength in figure 4.20c is lower. This could indicate that the mass variations over the oceans are caused by errors in the GRACE coefficients and are thus assumed to be noise, whereas the signal over continental regions comes from changes in the Earth's gravity field, yielding mass relocations due to hydrological phenomena.

The derived statistics in table 4.7 emphasize these observations. A global RMS of 0.9 mm/month of the differences between the full covariance and block diagonal covariance solution is negligible, whereas the differences between a full and a diagonal covariance-variance matrix reach up to  $\pm 80$  mm/month. However, these maxima are mainly caused by differences in the polar regions, which was already visible in figure 4.20. Moreover, this effect must be caused by a larger contribution of the regularization matrix in the spectral domain, when only variances are considered.

Table 4.7 shows a further interesting effect of the three different kernels. The statistics of the solutions with full and block-diagonal covariance matrices are very similar, whereas the derived values of the diagonal variance solution are generally smaller. This actually means that the appropriate kernel has stronger filtering characteristics, when only variances are considered. This is emphasized by the figures 4.18 and 4.19, as the filter kernel is generally larger when correlations between the coefficients are neglected.

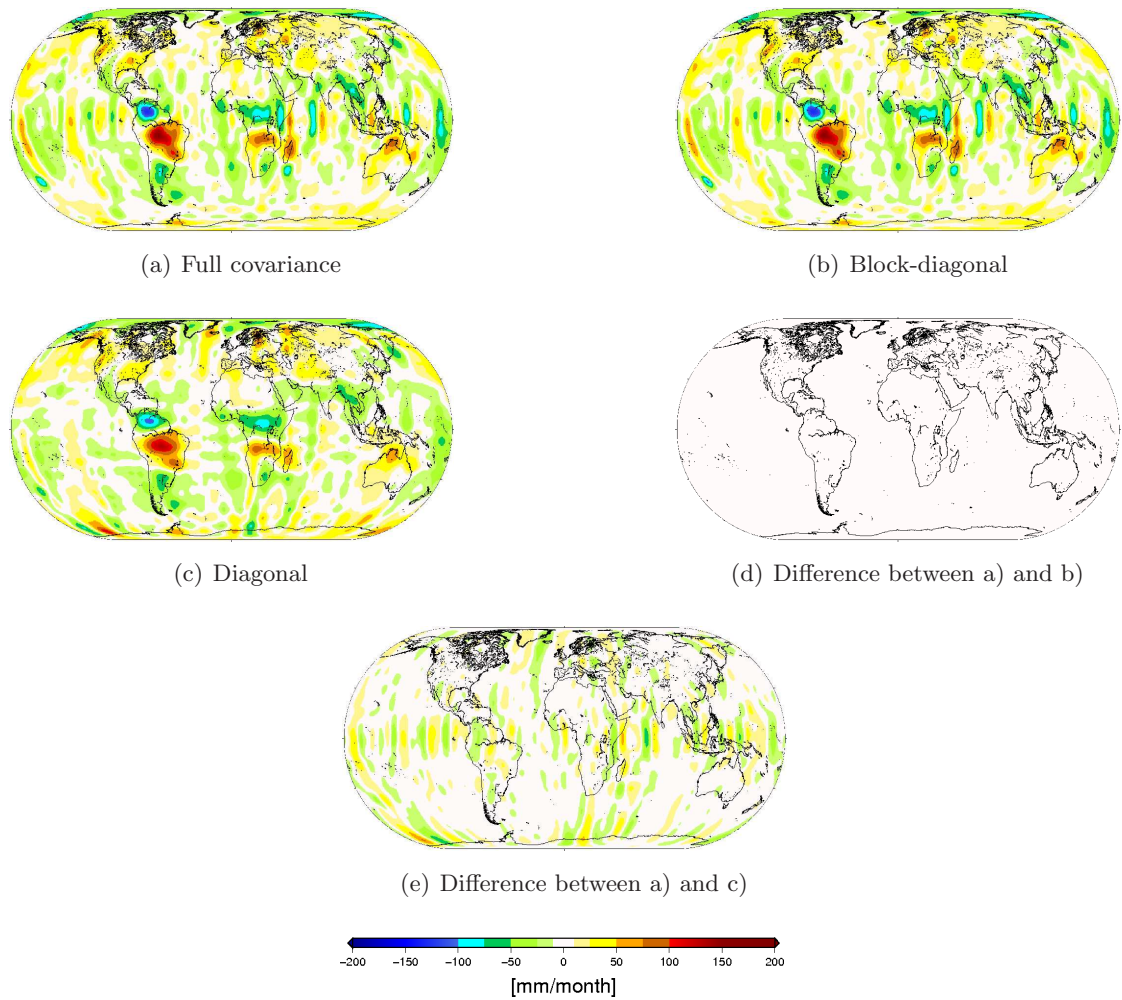


**Figure 4.20:** Visualized difference between the regularized solution, using a full, block-diagonal and diagonal covariance-variance matrix

**Table 4.7:** Statistics of the derived maps from figure 4.20

field	RMS	mean	min	max
	[mm/month]			
unfiltered	783.8	2.6	-4982.9	531.6
full covariance	26.2	-0.2	-129.6	151.2
block diagonal covariance	26.3	-0.2	-129.7	149.5
diagonal variance	25.7	-0.1	-106.6	131.7
Difference between a) and b)	0.9	0.0	-7.5	5.6
Difference between a) and c)	12.2	-0.1	-69.8	79.5

#### 4.4.3 Regularization of different monthly GRACE solutions

The whole method is now tested with data from May 2005 and September 2006 as well. Again, a mean power law of 70 time-variable CSR-4 solutions approximated until degree 22 is used as stochastic constraint and the noise information of the GRACE coefficients is taken from a fully populated simulated and scaled covariance matrix.

##### Spectral domain

The VCE converged already after 12 (May 2005) and 16 (September 2006) iterations. In both cases, the regularization term gained more weight compared to the GRACE coefficients. However, the variance components from January 2003 differ obviously from the other two solutions. Through the lesser weight of the regularization term, one can assume that the coefficients and their appropriate errors of May 2005 and September 2006 show a better agreement with the power law than the dataset from January 2003. This means conversely, that the datasets of May 2005 and September 2006 might be of better quality, as the VCE gives less weight to the regularization matrix, yielding a better agreement between the pure GRACE coefficients and the modelled degree variances.

**Table 4.8:** Estimated variance components of different monthly solutions

month	$1/\sigma_G^2$	$1/\sigma_K^2$	$\lambda = \sigma_G^2/\sigma_K^2$
January 2003	0.071	1.627	22.750
May 2005	0.244	2.910	11.917
September 2006	0.264	3.369	12.737

This lesser weight of the regularization matrix has obviously consequences for the contribution to the regularized Stokes coefficients (cf. figure 4.21). In May 2005 and September 2006, the lesser weight yields lesser influence of the regularization matrix. The solution is only dominated in zonal coefficients with  $l > 49$ . Again, this influence increases with increasing order. The sectorial part of the spectrum has a major contribution of the regularization matrix from degree and order 19, whereas January 2003 showed this contribution from degree and order 8.

These observations indicate that the monthly GRACE solutions possess a high noise content especially in the near sectorial and sectorial coefficients. This was already mentioned, when the unregularized coefficients were considered (cf. figure 4.11). Furthermore, in contrast to January 2003, the solutions from May 2005 and September 2006 show no contribution of the regularization term in the low frequency part of the spectrum.

The reason for the different contribution of the regularization becomes clear from figure 4.22, where the degree variances of the three months are plotted before and after the regularization. It is obvious that the signal strength of the data set from January 2003 is one order of magnitude higher than the other two solutions for coefficients with  $l > 10$ . This holds for the errors as well, even if the deviations are smaller. However, this differ-

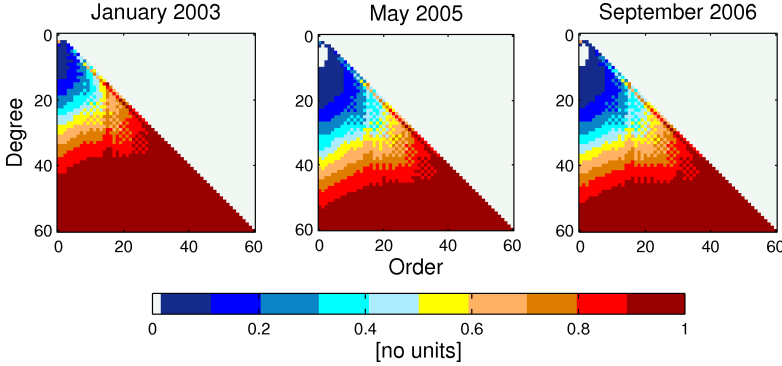


**Figure 4.21:** Spectral redundancy contribution of the regularization term, using GRACE data from different months

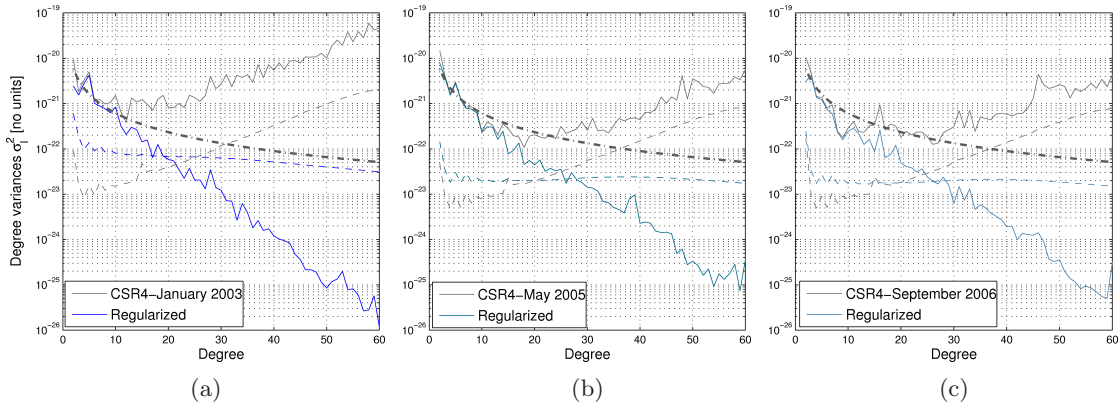


**Figure 4.22:** Signal- (straight lines), error (dashed lines) and modelled (bold dash dotted lines) degree variances before and after regularizing, the power law is approximated until the point of infliction of the signal degree variances of 70 monthly GRACE solutions.

ent signal and noise level leads to interesting effects. In January 2003, the unregularized noise variances curve crosses the signal curve at degree 20, which happens for the other two months at degree 27. If one thinks about the singal to noise ratio in this context, such a characteristic means that the signal of January 2003 is dominated by noise in the spectral part with  $l > 20$ , whereas May 2005 and September 2006 have a  $\text{SNR}_l > 1$  until degree 27.

This indicates that GRACE provides a time-variable signal of varying signal strength. After regularizing, the error variances from January 2003 already cross the signal curve at degree 20. May 2005 and September show a  $\text{SNR}_l > 1$  until degree 27. This means conversely that, if one assumes a power law as degree variance model and zero observations, the data quality of the GRACE coefficients is better in May 2005 and September 2006 and thus changes over time.

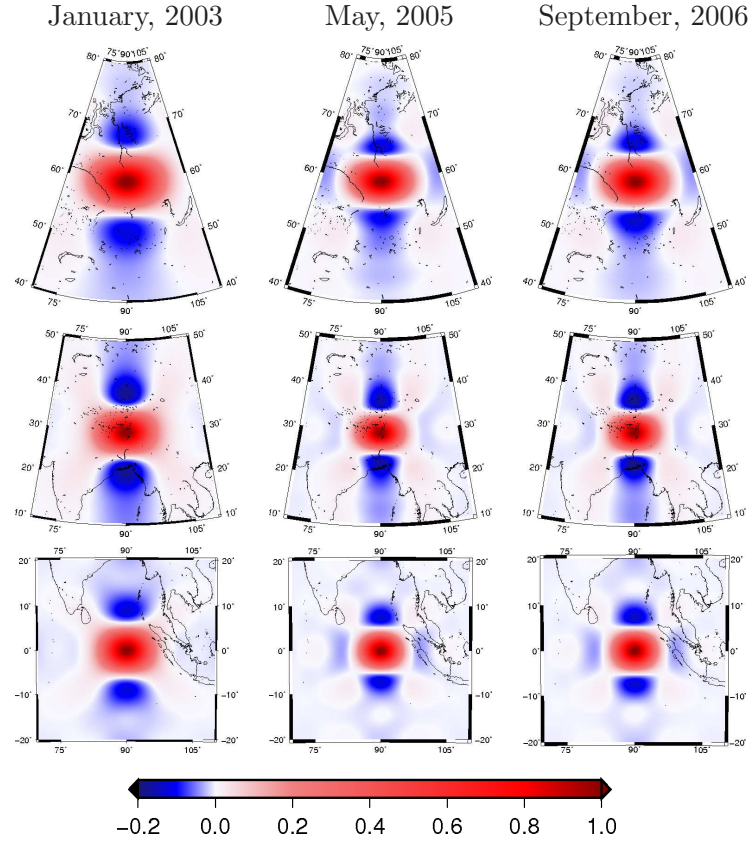


**Figure 4.23:** Propagated regularization filter kernels at  $\lambda = 90^\circ, \theta = 30^\circ$  (top row),  $\lambda = 90^\circ, \theta = 60^\circ$  (middle row),  $\lambda = 90^\circ, \theta = 90^\circ$  (bottom row), using GRACE data from three different months

### Spatial domain

The smoothing characteristics in the spatial domain are again analyzed by propagating the filter function at three points in space with changing latitude (cf. section 4.4.2). Even if using different covariance matrices changed the regularization filter kernel in the spatial domain, figure 4.24 shows that the kernel differs only slightly if GRACE data from other months is used for its construction. The kernels from May 2005 and September 2006 are little tighter than their counterpart from January 2003. Additionally, the sidelobes are less distinct, which actually means that these months needed lesser smoothing to satisfy the constraints, given by the regularization matrix.

The propagated kernels show one deciding characteristic of the regularization technique. Its filtering performance seriously depends on the *a priori* signal strength of the GRACE coefficients. If there is no need for a strong regularization, which means that the regularization matrix gained lesser weight in the linear model, the propagated kernels show smaller patterns in both latitude and longitude direction, yielding a higher spatial resolution than e.g. the kernel from January 2003. However, all three kernels possess similar spatial characteristics. First of all, their size increases with increasing latitude, yielding heavier filtering in near polar regions. The sidelobes show their maximal amplitude in mid-latitude regions, where the shape of the patterns is nearly circular near the equator.

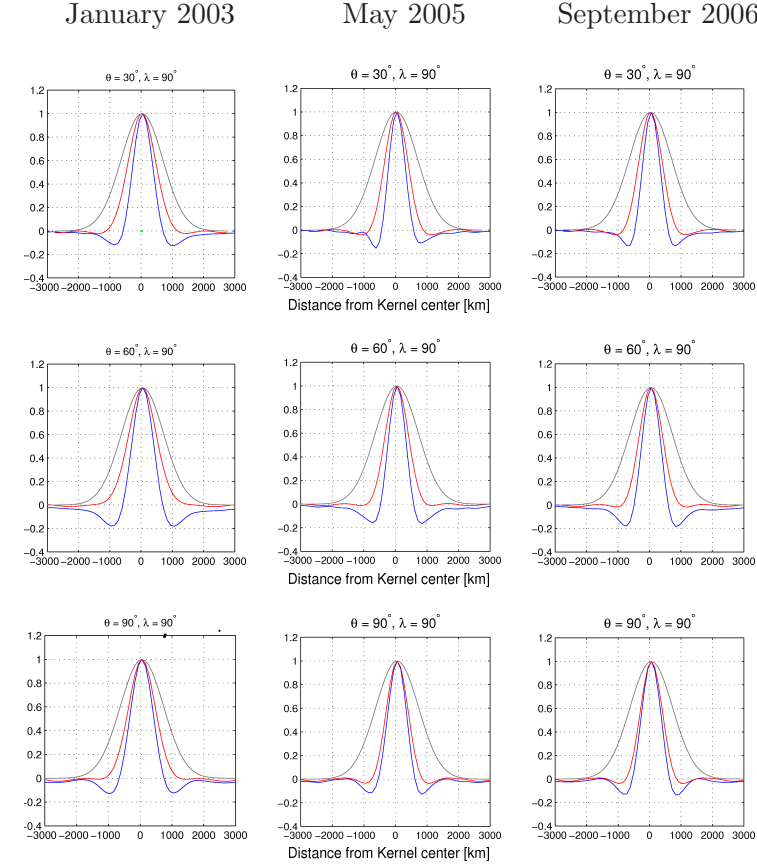


**Figure 4.24:** North-south (blue) and east-west (red) cross sections of the normalized regularization filter kernels from three different months, computed at  $\lambda = 90^\circ$ ,  $\theta = 30^\circ$  (top row),  $\lambda = 90^\circ$ ,  $\theta = 60^\circ$  (middle row),  $\lambda = 90^\circ$ ,  $\theta = 90^\circ$  (bottom row). The isotropic 800 km Gaussian filter (gray) is taken as reference

The smaller kernels of May 2005 and September 2006 theoretically result in a less filtered field. This is a logical consequence of the lesser signal power of these months, as the signal is less constrained. Thus, the deciding factor which impacts on the size of the kernel is the *a priori* signal strength of the pure GRACE coefficients, as the same constraint, i.e. the same power law, is assumed for each month due to the stationarity of the time-variable gravity field. This is actually a very positive finding, as the computation of the filter kernel decides how much weight must be given to the regularization matrix to meet the constraints.

These phenomena gain deciding influence, if the regularized coefficients are used to derive maps in terms of water equivalent heights per month (cf. figure 4.25). A visual statement can immediately be made, if the equatorial regions of the fields of May 2005 and September 2006 are considered. Even if Central and South America as well as Central and South Africa again show a large signal strength, there are more stripes recognizable, compared to January 2003. However, these maps again show noise reduced fields, whose spatial characteristics are assumed to be caused by changes in the Earth's gravity field. Furthermore, the colorscale of the maps in this work is chosen in such

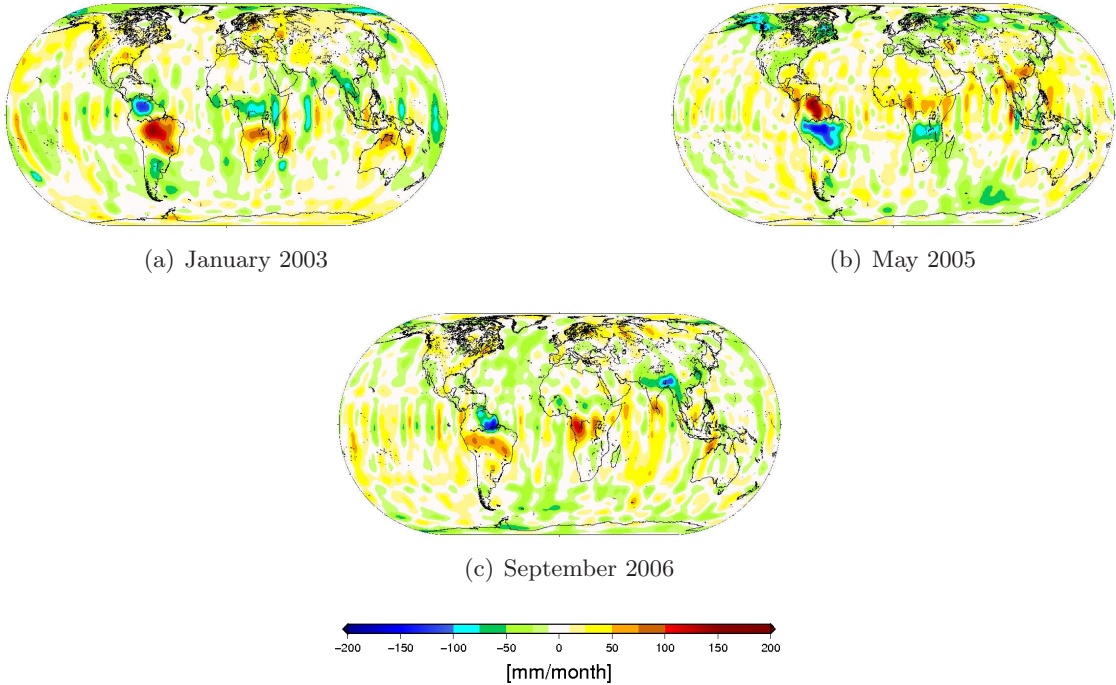


**Figure 4.25:** Results of the regularization filter for different monthly solutions

**Table 4.9:** Statistics of the derived maps from figure 4.25

field	RMS	mean	min	max
[mm/month]				
January 2003	26.2	-0.2	-129.6	151.2
May 2005	25.4	-1.6	-167.5	158.7
September 2006	22.6	-1.2	-163.8	121.6

way, that small variations are visible as well. The stripes generally have an amplitude of  $\pm 25$  mm/month. Other similar publications neglect such variations, yielding a field with subjectively less noise. Thus, one should concentrate on the large continuous signal patterns.

It was already mentioned that the smaller kernels in May 2005 and September 2006 will produce less filtered fields. However, table 4.9 shows a different characteristic. The maximal amplitudes of the three different fields have about the same magnitude, which actually means that the regularization filter attenuates the signal in such way that it agrees with the constraining degree variance model. Thus, the filter is only as strong as needed. Table 4.9 on the other hand supports the assumption of a stationary time-variable field, which was a finding of the comparison of the different power laws. Obviously, the minimal and maximal estimated signal changes from month to month, but the global RMS stays more or less constant, which indicates that the time-variable gravity field is stationary.

# Comparison of stochastic and deterministic averaging operators | 5

It was shown in different publications (see below) that the isotropic and anisotropic Gaussian as well as the decorrelated error filter, convolved with an isotropic Gaussian filter, show promising results when they are used to smooth the time-variable gravity field, derived from GRACE solutions. However, the characteristics of these filters are very different, especially if one considers the Bayesian type regularization and the anisotropic vector Wiener filter as well. Thus, this chapter deals with the comparison of the filtering characteristics in the spatial and spectral domain of the following averaging operators:

- the isotropic Gaussian filter with  $r_{1/2} = 800$  km (Chen et al., 2005)
- the anisotropic Gaussian filter with  $r_0 = 500$  km,  $r_1 = 2r_0$ ,  $m_1 = 15$  (Han et al., 2005)
- the correlated error filter with  $m_0 = 8, m_1 = 60, l_0 = 8, l_1 = 60, p = 2$ , convolved with a 500 km isotropic Gaussian (Swenson & Wahr, 2006)
- the anisotropic vector Wiener filter using a mean power law (4.1.1) with  $a = -19.8283$  and  $b = -1.3847$
- the regularization filter from section 3.3.2, where a mean power law (4.1.1) with  $a = -19.8283$  and  $b = -1.3847$  is used as stochastic constraint.

Furthermore, the results are validated with modelled mass variations, given by the Global Land Data Assimilation System (GLDAS) from the NASA. This model combines satellite- and ground-based observations to provide an accurate global model of e.g. continental water equivalent heights every three hours on a 1-degree grid. This high temporal resolution allows a reasonable validation of the derived fields from smoothed GRACE solutions. One has to mention that the provided data from the GLDAS is absolute, i.e. it must be differentiated with respect to time, if it is used as background model for validation purposes. Therefore, the formula of central differences (2.2.18) is applied here as well.

## 5.1 Filtering performance in the spectral domain

The degree RMS of the averaging functions are here introduced as a rough measure for the weight which is given to coefficients with a certain degree. It must be said that a

presentation of degree RMS of the regularization and the anisotropic vector Wiener filter do not consider correlations between the coefficients. Thus, figure 5.1 should be seen as brief impression of the filtering characteristics in the spectral domain. Moreover, a complete presentation of anisotropic vector filters in the spectral domain is rather difficult due to their pure size. Thus, it was decided to concentrate on the averaging coefficients  $w_{l'm'}^{lm}$  with  $l = l'$  and  $m = m'$ , which actually are the main diagonal elements of a filter matrix.

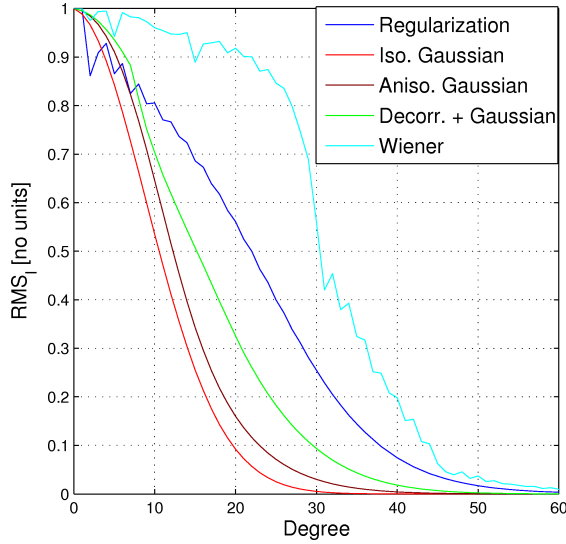


**Figure 5.1:** Degree RMS of the isotropic Gaussian (cyan), anisotropic Gaussian (red), full covariance Wiener (green) and regularization (blue) averaging operators

The coefficients of the Gaussian filters smoothly attenuate and remove the high frequency coefficients completely. The Wiener type filter shows only little attenuation until degree 30. This actually comes from the noise level of the unfiltered GRACE coefficients. In section 4.4.1 it was discussed that the unfiltered noise degree variances cross the modelled signal variance, given by the power law, at degree 30. The coefficients of the Wiener filter suddenly drop to a weight of 0.5 between degree 30 and 32, after which they slowly attenuate until degree 60. However, the coefficients are still larger than these from the other filters, yielding a poorer smoothing effect.

Even if the regularization uses the power law and the simulated error estimates as well, the filter coefficients attenuate similar to the 800 km Gaussian with little deviations in the low-degree part of the spectrum, especially in the degree 2 coefficients. A large contribution of the regularization term in these coefficients was already noticed in section 4.4.1. Additionally, nearly the whole spectrum is used, as only coefficients with  $l > 55$  are removed, which is in contrast to e.g. the Gaussian filter coefficients.

The unfiltered spectrum of the GRACE coefficients usually shows a rapid increase of spectral signal power with increasing order. Furthermore, even the low frequency sectorial coefficients possess a relatively high signal power. This leads to the assumption that the high noise level in the high frequency coefficients is concentrated in the near sectorial, sectorial and high frequency tesseral coefficients. Thus, an averaging operator

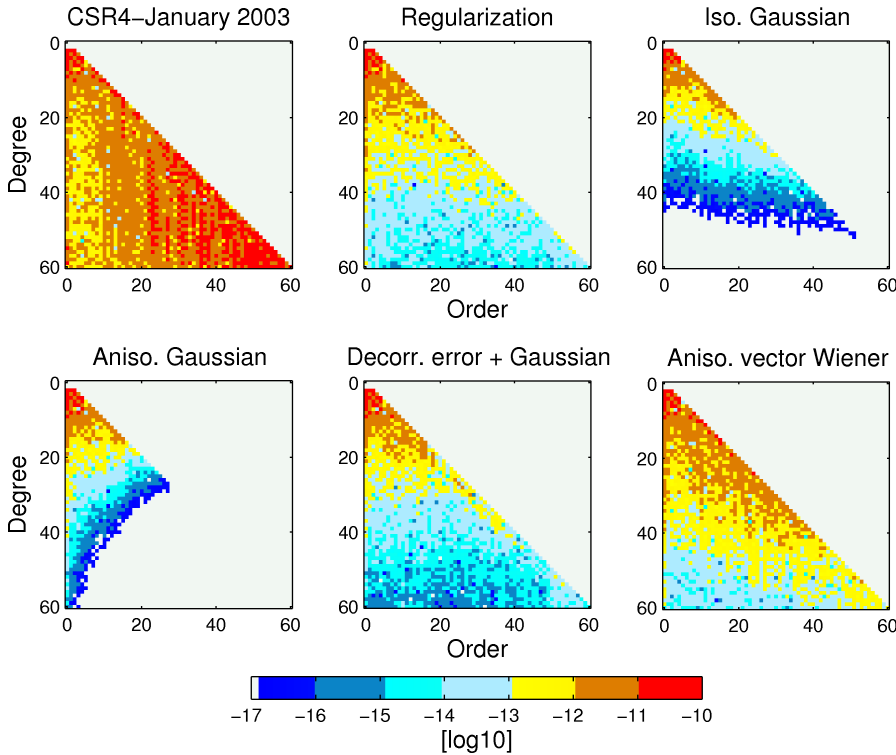


**Figure 5.2:** Filtered GRACE coefficients for January 2003

should remove this characteristic, to seriously decrease the noise-level which is successfully done by all the filters presented in figure 5.2.

All averaging operators attenuate the signal power in the near sectorial and sectorial part of the signal and make distinct boundaries between the degree (isotropic) and order bands clearly visible. However, even the isotropic Gaussian filtered spectrum shows a slight tendency towards anisotropy, as the magnitude of coefficients with the same degree increase with increasing order. This is also the case for the other filtered spectra. Moreover, the regularization and correlated error filter show a further interesting effect. Both allow a higher signal strength in the sectorial part of the spectrum with larger degree and order, yielding more high-frequent information in the filtered spectrum.

The total spectral power of the coefficients is again analyzed with their degree variances, presented in figure 5.3. The degree variances of the Gaussian filtered coefficients show a very rapid attenuation, yielding only slight contribution of the high frequency part of the spectrum to a derived field. Additionally, the anisotropic Gaussian filtered degree variances oscillate heavily with increasing degree. This is actually an unrealistic behavior, as the degree variance spectrum should theoretically decay smoothly (e.g. isotropic Gaussian). On the other hand, the Wiener filter does not successfully constrain the signal power to attenuate with increasing degree, yielding the largest spectral power, compared to the other filtered spectra. The degree variances of the regularized coefficients show similar relative magnitudes, compared to the Wiener and decorrelated error filter, which is obviously not the case for the Gaussian filtered spectra.

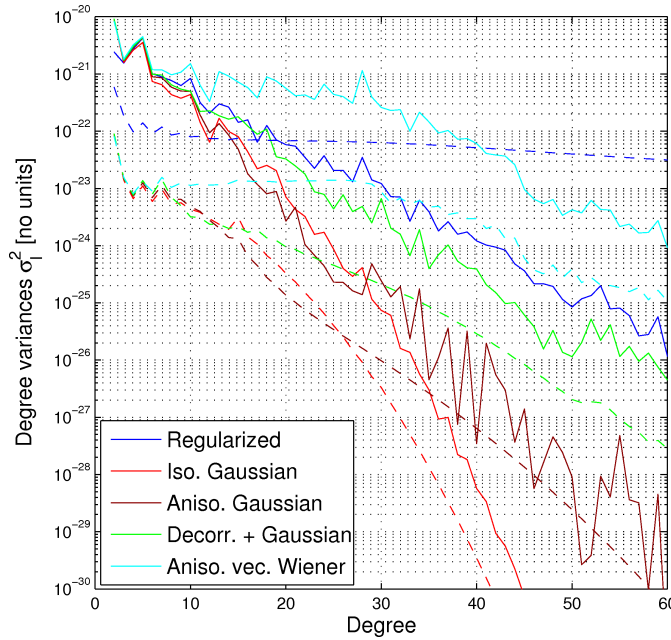


**Figure 5.3:** Degree variances of the the filtered signals (lines) and errors (dashed lines)

The filtered noise shows a different characteristic. The propagated errors usually converge with the attenuating signal, which does not hold for the regularized errors. But it was already mentioned that these errors were the output from a parameter estimation and this effect is a logical consequence of the choice of the degree variance model for regularization. The other filters simply attenuate the spectral power of the errors as well, which causes the smaller noise degree variances. However, in the low frequency part of the spectrum, the degree variances of each filtered signal are very similar.

## 5.2 Filtering performance in the spatial domain

Each filter function is validated along the  $\lambda = 90^\circ$ -meridian at  $\theta = 90^\circ$ ,  $60^\circ$  and  $30^\circ$  respectively, according to the propagation formulae given in the appendix. The cross-sections of the filter kernels are presented in figure 5.4 and a top view in 5.5. The distance from the Kernel center is computed across the  $\lambda = 90^\circ$ -meridian for the north-south-sections and across the appropriate parallels  $\theta = 90^\circ$ ,  $60^\circ$  and  $30^\circ$  for the east-west sections to receive a proper scale between the smoothing radii in both directions. The isotropic 800 km Gaussian kernel is plotted as reference.

In figure 5.4 and 5.5, the anisotropic Gaussian, decorrelated error and regularization filter kernels are tighter in north-south direction, yielding a stronger filtering in the east-west direction. However, the anisotropic Gaussian filter shows the same effect, which is caused by the different averaging radii in both longitude and latitude direction. The Wiener filter shows only slight difference between the N-S and the E-W cross section and a tighter kernel than the other averaging operators. This actually explains its insufficient smoothing effect.

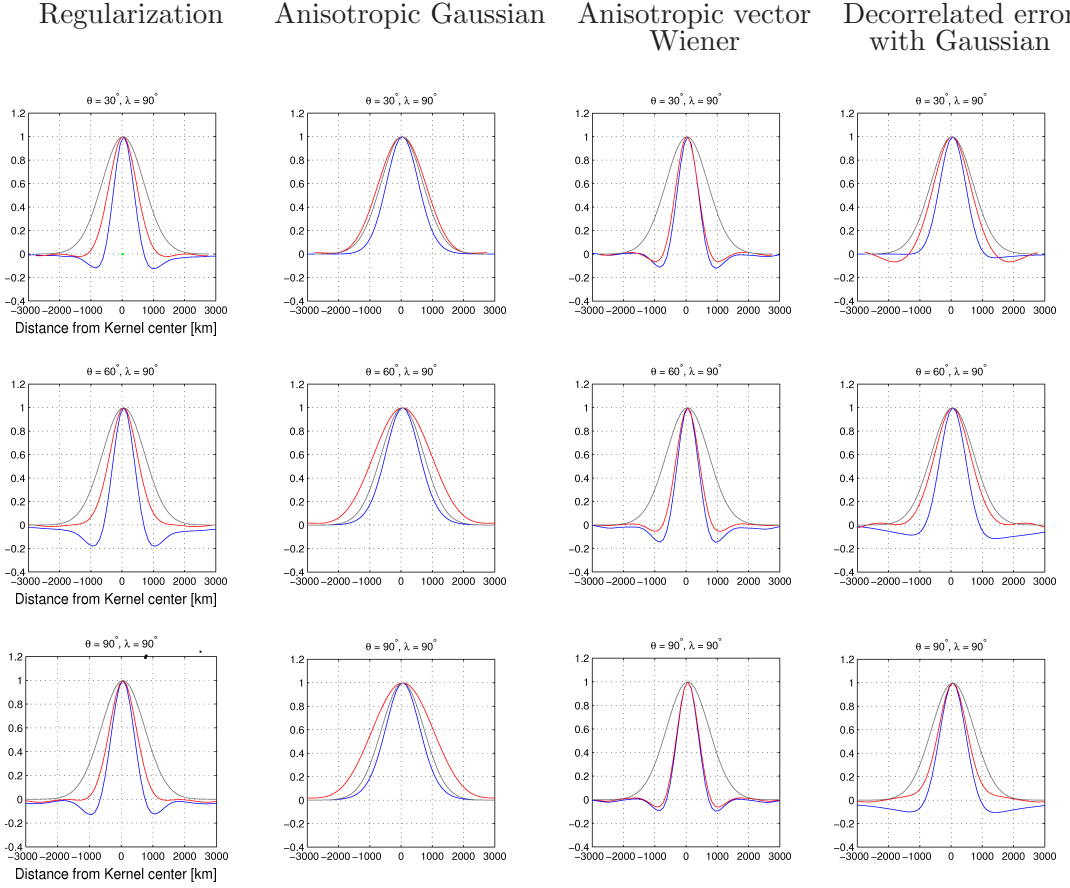


**Figure 5.4:** North-south (blue) and east-west (red) cross sections of the normalized filter kernels, computed at  $\lambda = 90^\circ, \theta = 30^\circ$  (top row),  $\lambda = 90^\circ, \theta = 60^\circ$  (middle row),  $\lambda = 90^\circ, \theta = 90^\circ$  (bottom row). The isotropic 800 km Gaussian filter (gray) is taken as reference

But the decorrelated error, anisotropic vector Wiener and regularization filter respectively show an important difference to the Gaussian filters. All of them possess negative sidelobes in latitude direction, which counteracts the north-south stripes from unfiltered GRACE coefficients. Additionally, the Wiener filter shows a similar effect in east-west direction as well, which indicates isotropic filtering characteristics and is thus independent from the latitude. However, the decorrelation effect attenuates for the correlated error filter with increasing latitude. In the near polar regions, it shows similar characteristics to the anisotropic Gaussian filter.

On the other hand, the regularization has its maximal decorrelating effect in mid-latitude regions. If the Gaussian filters are regarded from the point of view of decorrelation, it becomes clear why it indeed smoothes the gravity signal, but maintains the north-south stripes in the filtered field: the Gaussian averaging functions have no negative side-lobes at all and thus do not decorrelate the field. Its filtering effectiveness comes only from a proper choice of the averaging radii and thus an attenuation of the signal strength of short-wavelength coefficients. However, the anisotropic Gaussian filter yields a better resolution in north-south direction through its smaller averaging radius.

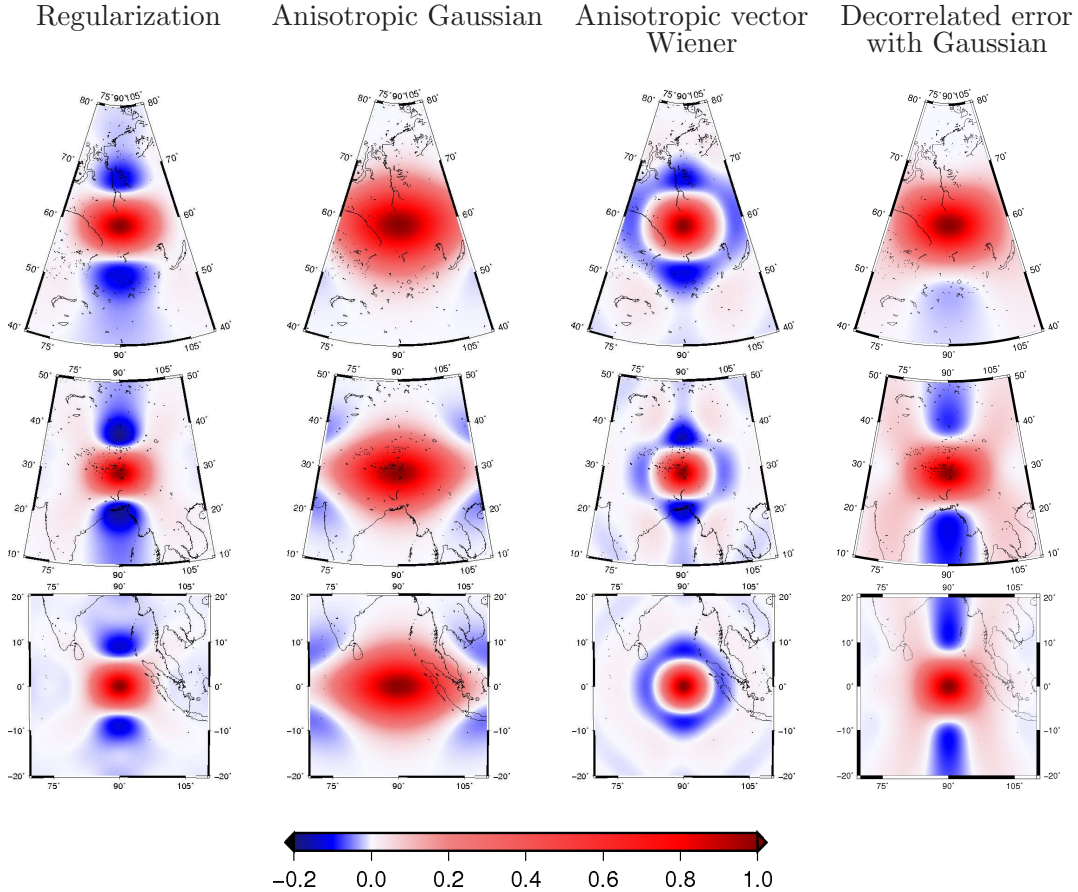


**Figure 5.5:** Propagated filter kernels at  $\lambda = 90^\circ, \theta = 30^\circ$  (top row),  $\lambda = 90^\circ, \theta = 60^\circ$  (middle row),  $\lambda = 90^\circ, \theta = 90^\circ$  (bottom row)

The regularization kernel shows similar characteristics, compared to the decorrelated error filter, even if both averaging functions are based on totally different approaches (stochastic and deterministic filtering). A further effect is the tendency towards isotropy of the full covariance Wiener filter, which agrees with the cross section in figure 5.4. Obviously, the Wiener filter shows isotropic characteristic in the equatorial and near polar regions, as there is only little difference between the N-S and E-W cross sections. The Gaussian kernel clearly shows the effect of a two different averaging radii, as it shows a broader stretch in E-W direction, which yields a better resolution in the latitude direction. However, the size of the Kernel differs completely from the other presented functions, which should lead to an overall lower spatial resolution.

### 5.3 Comparison with modeled and observed hydrology

The filtered coefficients are used to compute fields in terms of water equivalent heights per month for January 2003, May 2005 and September 2006 to validate the latter results with modelled mass variations, derived from the GLDAS. The maps are presented in figure 5.6, the appropriate statistics in table 5.1.

It suddenly catches the eye that all filters successfully reduce the signal strength of the noisy north-south stripes to a level, where the observable signals are assumed to

come from mass relocations mostly due to hydrological phenomena, as each map shows strong similarities to the field, which was derived from the GLDAS, even if the signal strength varies. The Gaussian filters successfully remove the noise structures by attenuating the highly noise-contaminated coefficients. Thus, especially the isotropic Gaussian filter still shows slight stripy artifacts in the equatorial regions. On the other hand, the anisotropic Gaussian filter shows especially in this part of the field only slight stripes. This actually comes from a stronger attenuation of the spectral signal power in near sectorial and sectorial coefficients. The remaining stripes in the decorrelated error filtered field can be ascribed to this characteristic as well through its convolution with an isotropic Gaussian filter.

All filtered maps show similar spatial patterns with a large signal in middle- and South America, in Africa and in northern Australia, which are thus strongly assumed to come from hydrological phenomena. On the other hand, the origin of the signal over the oceans is unknown, as the influence of the oceans is removed from the CSR4-coefficients. Thus, one can assume that such a signal either comes from true mass variations in the oceans, which would indicate uncertainties in the dealiasing model or from residual noise in the GRACE coefficients themselves. This becomes even more complex, if one thinks about the difficult determination of patterns with a size less than  $10^6 \text{ km}^2$  as signal or noise.

Additionally, the estimated signal strength varies, depending on the used filter. The isotropic Gaussian shows a signal with a maximal amplitude of about  $100 \text{ mm/month}$  in the Amazon basin in January 2003, whereas the maximum of its anisotropic counterpart is between  $100$  and  $150 \text{ mm/month}$ , which agrees with the correlated error filter. However, both stochastic filters show a much larger signal of  $150\text{--}200 \text{ mm/month}$  in the Amazon basin. These differences hinder a statement about the magnitude of the true mass variations in these regions.

All filtered fields show similar patterns, compared to the GLDAS field. On the other side, the isotropic and anisotropic Gaussian as well as the decorrelated error filtered fields show only a large area in central Africa with a mass change between  $25$  and  $50 \text{ mm/month}$ . The regularized field shows a larger signal in the near equatorial regions, which is visible in the GLDAS field as well. A similar situation is visible e.g. near the east coast of North America. Moreover, the regularized field shows patterns which are the most consistent with the GLDAS field. This is emphasized by the fields for September 2006, even if the overall signal seems much lower compared to May 2005 or January 2003. However, this might come from lesser mass variations during the autumn months, as the GLDAS-field shows only small patterns as well.

Unfortunately, even if there are clear similarities between the modelled mass variations and the derived fields from GRACE, a clear identification of a signal pattern as mass change might still be difficult. It was already mentioned that a distinction of signal patterns from noise artifacts, which are smaller than  $10^6 \text{ km}^2$ , is not possible. If one regards such an area as maximal radius of half wavelength, this would mean that the GRACE coefficients with  $l > 20$  do not contain reasonable information due to a dominating noise level.

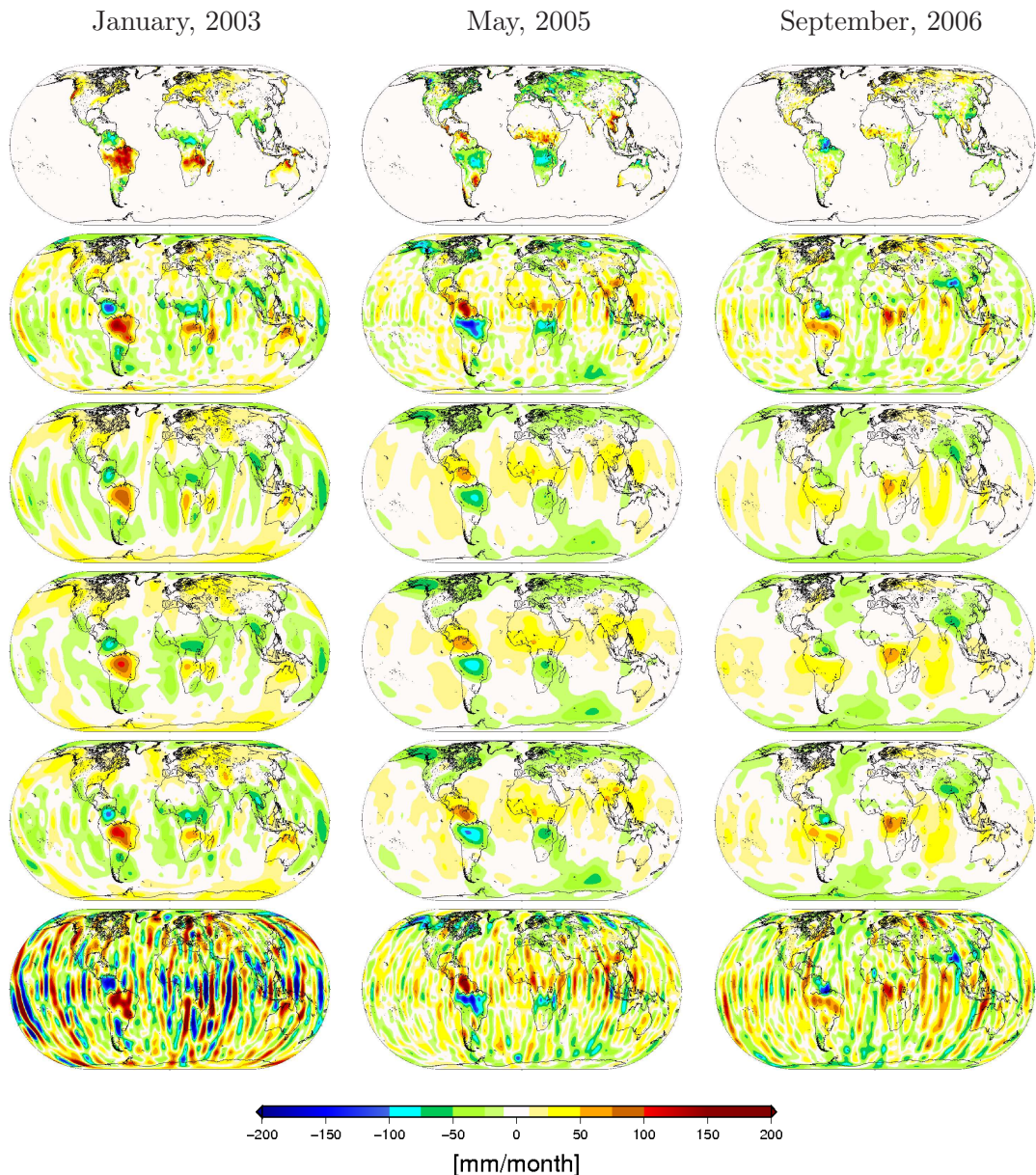


**Figure 5.6:** Mass variations in January 2003, May 2005 and September in [mm/month], derived from (top to bottom) GLDAS hydrology model and GRACE coefficients, filtered with regularization filter, 800 km isotropic Gaussian filter, anisotropic Gaussian filter, decorrelated error filter convolved with a 500 km Gaussian filter and anisotropic vector Wiener filter

The derived statistics from the maps in figure 5.6 are presented in table 5.1. The Gaussian filtered fields generally show the smallest signal amplitudes. This indicates that the Gaussian type operators attenuate the signal strength the most. This holds for the decorrelated error filter as well, as its successfull approach needs the additional convolution with a Gaussian type filter. On the other hand, even if the maps, derived from regularized GRACE coefficients, usually show noise-reduced fields, they possess the largest amplitudes, compared to the other solutions, which is indeed a positive characteristic of the regularization filter.

**Table 5.1:** Statistics of the derived maps from figure 5.6 in [mm/month] for January 2003, May 2005 and September 2006

Field	RMS	mean	min	max
<b>January, 2003</b>				
GLDAS	16.5	2.5	-246.6	216.5
Regularization	26.2	-0.2	-129.6	151.2
Isotropic Gaussian	19.7	2.5	-75.4	90.5
Anisotropic Gaussian	20.9	2.4	-84.0	107.2
Decorrelated error + Gaussian	23.9	2.4	-111.0	123.1
Anisotropic vector Wiener	62.5	1.9	-370.6	424.7
<b>May, 2005</b>				
GLDAS	18.0	-3.4	-261.6	216.2
Regularization	25.4	-1.6	-167.5	158.7
Isotropic Gaussian	16.7	-3.4	-75.9	67.1
Anisotropic Gaussian	18.3	-3.3	-90.5	75.9
Decorrelated error + Gaussian	19.4	-3.3	-106.6	100.5
Anisotropic vector Wiener	34.3	-2.9	-188.2	183.1
<b>September, 2006</b>				
GLDAS	10.4	0.6	-143.7	247.9
Regularization	22.6	-1.2	-163.8	121.6
Isotropic Gaussian	15.9	-3.9	-59.4	63.4
Anisotropic Gaussian	16.8	-4.0	-65.4	68.0
Decorrelated error + Gaussian	17.7	-4.0	-87.7	91.2
Anisotropic vector Wiener	34.5	-3.6	-184.1	154.2

The RMS-values of the fields show another interesting characteristic. It was already mentioned that the RMS-values of the regularized solutions of January 2003, May 2005 and September 2006 are more or less constant, which indicates stationarity of the time-variable gravity field. This holds as well for the other solutions, which were derived from GRACE coefficients. The deviation of the Wiener filtered solution in January 2003 might be caused by the remaining noise content due to a too weak filtering performance. The GLDAS must be neglected in this context, as it does not provide global values and thus neglects e.g. mass variations in the oceans.

A further validation of the presented averaging operators is done by comparing the estimated mass variations with the estimates from the GLDAS on basin scale. Therefore, the averaged mass variations of the Amazon basin, Central Africa and Eastern Australia are computed from the filtered maps and the GLDAS field respectively. The concerning regions are marked in figure 5.7 and the appropriate mass variations are presented in table 5.2. However, this validation is completely based on such observations which are mapped from the GLDAS. This conversely means that there are indeed many other effects, which are not considered by that model and still influence the GRACE solutions. Thus, such a comparison should only be seen as rough validation of the filtered fields.

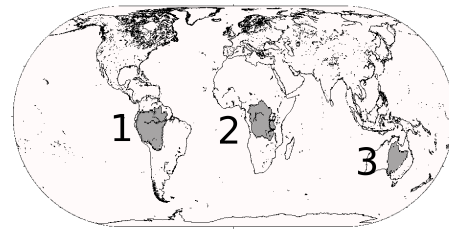


**Figure 5.7:** Catchments for validation of the filtered fields with the GLDAS

**Table 5.2:** Mass variations of January 2003, May 2005 and September 2006 in [mm/month] for Amazon (1), Central Africa (2) and Eastern Australia (3), cf. figure 5.7

If one considers table 5.2 one has to keep in mind that it was expected that GRACE would detect mass variations with an accuracy of about 2 mm in terms of water equivalent heights. Even if this objective is obviously not achieved, most mass variations lie in range of  $\pm 10$  mm/month around the predicted value from the GLDAS. However, the mass estimate for Central Africa in September 2006 shows a huge difference to the GLDAS-value. This was already visible in figure 5.6. If one takes the similarities of the GRACE estimates and the modeled mass variations into account, it could be argued that this signal indeed came from a change in the gravity field, but not due to hydrological effects, as it was not mapped from the GLDAS. Such differences make it even more difficult to use such models on the one hand and the GRACE satellites on the other as reliable source for estimates of mass variations.

Finally, the modeled and filtered fields from GLDAS and GRACE coefficients are compared with observed storage changes. Section 6.1 discusses the method how these values are computed. In this section here, they are assumed to be the most accurate estimates of mass variantions on basin scale. The values are computed in the three regions North China, Western Sahara and Yukon, which is visualized in figure 5.8.

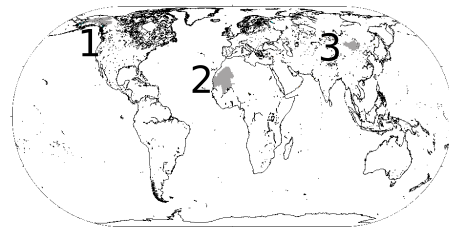


**Figure 5.8:** Catchments for validation of the filtered fields with observed hydrology

**Table 5.3:** Mass variations of January 2003 in [mm/month] for Yukon (1), Western Sahara (2) and North China (3), cf. figure 5.8

Field	1	2	3
Observed hydrology	3.2	2.6	23.7
GLDAS	-0.3	-1.2	11.4
Regularization	-6.1	2.1	28.9
Isotropic Gaussian	0.4	-1.9	19.3
Anisotropic Gaussian	-1.5	-0.6	24.1
Decorrelated error with Gaussian	-2.2	1.5	20.6
Anisotropic vector	-11.3	-12.0	53.1
Wiener			

If the deviations of the estimated from the observed values are considered (cf. table 5.3), it becomes clear that none of the presented methods is able to reach the predicted accuracy of 2 mm. However, there is a good agreement between the estimates in the three catchments, as the maximal deviation from the observed value is about 5 mm (the Wiener filter is not taken into account here due to its insufficient filtering performance). Unfortunately, the GLDAS shows e.g. in Yukon a bigger deviation from the observed value than the derived fields from the GRACE solutions. This emphasizes the assumption that modeled mass variations might be partly inaccurate as well or do not consider all effects which influence such variations. Thus, comparing the filtered GRACE solutions with such a model is not sufficient to provide a reasonable validation.

To summarize the latter results it can be said that all filters successfully attenuate the signal strength of the erroneous north-south stripes. The Gaussian filters simply decrease the spectral power of the spherical harmonic coefficients of short wavelength, whereas the decorrelated error filter impacts especially on the correlations between the coefficients to remove the stripes. The regularization and anisotropic vector Wiener filter use stochastic information and a least squares estimation procedure to build the filter kernel. The Wiener filter has a too weak filtering performance to successfully remove the north-south stripes. Thus, the derived fields still possess unrealistic magnitudes of mass variations. The regularized solution shows similar signal patterns if compared with the GLDAS. However, even if the filtered fields show only little remaining noisy artifacts, there are indeed differences between the mass variations, which were derived from the GLDAS and the GRACE estimates. These differences could come from remaining errors in the GRACE coefficients or even from gravity changes which were not mapped by the GLDAS. Moreover, a comparison with observed hydrology shows that even the GLDAS seems to provide inaccurate mass estimates. If one considers table 5.3 in this context again, it might be said that the mass estimates from filtered GRACE data are at least of similar accuracy.

# Constraining monthly GRACE solutions with hydrological mass estimates

6

The previous sections discussed several methods to decrease the noise-content in time-variable GRACE coefficients. But even if the filters delivered promising results, their appropriate operators are based on either an averaging radius (Gaussian type) or on empirical degree variance models (Wiener type and regularization). Thus, the outcome of the filtering procedure depends on a proper choice of the input parameters. Moreover, this choice is mainly based on theoretical knowledge, but does not take into account true empirical data, e.g. terrestrial observations. Furthermore, the Gaussian averaging operator also showed that the strength of “good signal” is attenuated as well, depending on the halfwidth radius, which is obviously an unwanted secondary effect. On the other side, the Wiener filter and regularization use a degree variance model and simulated error estimates to build the filter kernel. Thus, the filtering performance of such kernels is mainly based on the quality of the input data.

However, it is a matter of common knowledge that a large contribution to the time-variable gravity signal comes from continental hydrological mass relocations, which should be (theoretically) detectable with the GRACE satellites. But the noise level in unfiltered coefficients from GRACE showed a very high noise content in the high frequency part of the signal, which should contain information about short-period and/or small scale mass variations. This high noise-level led to unrealistic estimates of storage changes, which made filtering of the pure GRACE coefficients inevitable.

It was shown in chapter 5 that there are deviations, when one compares mass variations, derived from GRACE solutions, with observed values. Thus, this section describes a method to make both GRACE estimates and observed hydrology consistent by using these hydrological observarions as constraints in a sequential least squares estimation.

## 6.1 Continental hydrology and GRACE

The redistribution of water within the oceans, between the oceans and continents, and over the continental surface, can cause changes in the Earth’s gravity field (Wahr et al., 1998). Such mass variations, caused by hydrological phenomena, mainly happen in the so called *hydrosphere*, which extends about 1 km down into the lithosphere and about

15 km up into the atmosphere. In this area, water assumes different states of aggregation and circulates through manifold paths of the *hydrologic cycle* (cf. figure 6.1). A concise description of this schematic graphic is given in (Chow et al., 1988): Water *evaporates* from the oceans and the land surface to become part of the atmosphere; water vapor is transported and lifted in the atmosphere until it condenses and *precipitates* on the land or the oceans; precipitated water may be *intercepted* by vegetation, become *overland flow* over the ground surface, *infiltrate* into the ground, flow through the soil as *subsurface flow* and discharge into streams as *surface runoff*.

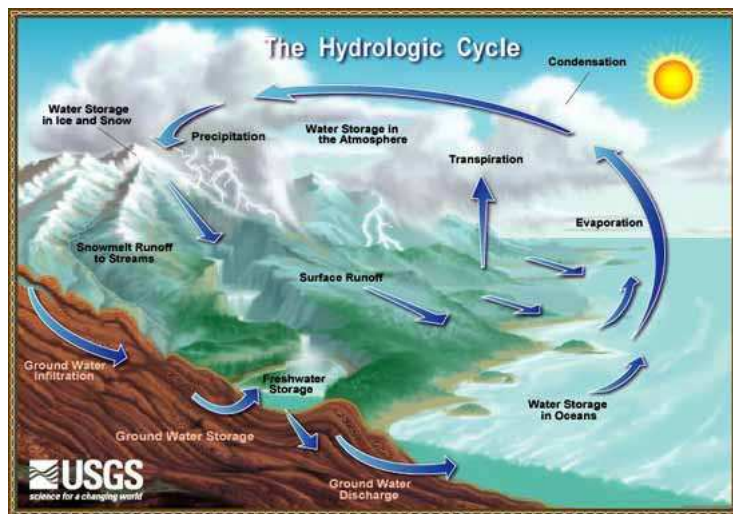


**Figure 6.1:** Hydrologic cycle (source: <http://www.ucmp.berkeley.edu>)

However, even if this concept is rather simple, an accurate acquisition of data for one particular effect is very complex. If one thinks about precipitation, it is obvious that the amount of rainfall is neither constant in time, nor in space. Observing phenomena like groundwater discharge or infiltration is very difficult due to the manifold number of possible flow paths. Additionally, even if the total amount of water in the hydrologic cycle remains constant, the contribution to the different subsystems changes over time and depends on the concerning regional and local characteristics.

Due to these reasons, the observation of hydrological effects is mainly restricted to local or regional areas. On the other hand, large scale hydrological data can only be obtained from models like the GLDAS. Such models are always based on certain parameters, assumptions and input data and thus contain uncertainties and errors (Zenner, 2006). This is actually the point where modern space borne gravity missions come into play. As the impact of the oceans and the atmosphere is usually removed from the satellite data, the provided Stokes coefficients could be directly connected to mass variations due to continental hydrological effects and thus allow accurate estimates of mass variations from large areas down to e.g. river basins. Such measurements would be very helpful to improve existing hydrological models. In (Wahr et al., 1998), it was predicted that GRACE would be able to deliver monthly values with an accuracy of about 2 mm in equivalent water thickness over land. However, this accuracy has not yet been achieved (cf. section 5.3). The reasons are mostly the large errors in spherical harmonic coefficients of short-wavelength, i.e. the coefficients with large degree and order (Han et al., 2005; Klees et al., 2008). But on the other hand, it was shown in many publications that the

Stokes coefficients from GRACE indeed contain hydrological signals (e.g. Wahr et al., 2004; Zenner, 2006) as the monthly solutions from GRACE showed a good agreement with mass variations from hydrological models. The findings in chapter 5 agree with these assumptions, as there are similarities with the GLDAS and observed hydrology, even if the achieved accuracy is less than it was initially predicted.

However, it was already mentioned that the accuracy of these models depends on many factors. Thus, it would be interesting to compare the estimates from GRACE with observed hydrological data. Therefore, the monthly storage change of a particular catchment is given through the *water balance equation*:

$$P - R - ET_a = \frac{\partial S}{\partial t} \quad (6.1.1)$$

where

$P$	Precipitation
$R$	Surface run-off
$ET_a$	actual Evapotranspiration
$\partial S/\partial t$	total water storage change

This is illustrated in figure 6.1, where precipitation either infiltrates into the ground or remains on the surface. The water on the surface might discharge through surface run-off or evapotranspire. At this point, a digression concerning hydrology must be made. The average duration of a water molecule to pass through a subsystem of the hydrologic cycle is given through

$$T_r = \frac{S}{Q} \quad (6.1.2)$$

where

$T$	average residence time
$S$	volume of water
$Q$	flow rate

This actually means that the average residence time of a certain hydrological effect must be smaller than 30 days to seriously impact on monthly GRACE solutions. In (Chow et al., 1988), a few quantities of such effects are listed. It is mentioned that e.g. fresh groundwater has a global volume of about  $10\,530\,000\,\text{km}^3$  and a flow rate of  $2200\,\text{km}^3/\text{year}$ . This means that fresh groundwater remains on average 4786 years under the surface of the earth and thus does not impact on monthly mass variations. On the other hand, the residence time for e.g. atmospheric moisture is 8.2 days until the molecule precipitates, for surface run-off through rivers about 17 days. Thus, precipitation, surface run-off as well as evapotranspiration are those effects, which influence the Earth's gravity field in short periods and thus impact on the GRACE solutions. However, these values are very rough measures and vary in time and space.

From equation (6.1.1) it now becomes obvious that the considered effects actually determine mass variations within a monthly time period. Unfortunately, the observation of large-scale evapotranspiration is very difficult, as it depends on both time and position. However, some catchments have certain geographical and climatical characteristics that

evapotranspiration can be completely neglected. These catchments could be used to determine accurate storage changes, as the water balance equation can be simplified to

$$P - R \approx \frac{\partial S}{\partial t} \quad (6.1.3)$$

If the GRACE solutions are used to compute mass changes in these catchments, both storage changes from hydrological observations, i.e. (6.1.3), and GRACE can be compared as

$$\frac{\partial S}{\partial t} \approx \dot{h}(t) \quad (6.1.4)$$

where  $\dot{h}(t)$  denotes estimates of mass variations, derived from monthly GRACE solutions.

Regions with negligible evapotranspiration are

- arctic and arctic tundra areas with sub-zero temperatures in winters
- dry areas like deserts with very meagre precipitation
- semi-arid regions fed by seasonal rivers which run dry if there is no precipitation

If there occur sub-zero temperatures over a prolonged period of time, the surface is assumed to be frozen. Thus, precipitation would remain as snow or ice. Additionally, some catchments show only very little precipitation in these periods. On the other hand, dry desert regions are suitable as well, as there cannot be evapotranspiration without rain. The third point becomes clear, if large river basins are regarded. There are certain periods, where they completely run dry due to a very meagre precipitation. This holds especially for semi-arid regions with less vegetation.

Data for precipitation and run-off can be obtained from the Global Precipitation Climatology Center (GPCC) and the Global Runoff Data Centre (GRDC) respectively. In this work, the hydrological data contains precipitation and run-off values for 167 catchments since January 1975. In order to select the catchments which met the condition of negligible evapotranspiration, precipitation and run-off of each of these catchments are plotted for a time-series of one year. For desert catchments, precipitation has to be smaller than 15 mm/month, while arctic and arctic tundra catchments exceed this value, when the surface run-off is approximately zero.

About 60 catchments met the requirements for a negligible evapotranspiration for January 2003. However, only 28 of them are usable in the computation process due to data gaps. Figure 6.2 shows the precipitation and run-off values for some of the selected catchments and covers all three criteria for a negligible evapotranspiration:

- The Churchill basin, which is located in Central Canada, shows approximately zero surface run-off, even when there is precipitation. This indicates frozen conditions.
- Western Sahara features only little precipitation and surface run-off, which leads to a negligible evapotranspiration
- Rio Santiago shows very high precipitation values during an annual period, whether surface run off is meagre. However, the period from December to April indicates a drying out of the river basin due to leaking precipitation. If there is no rainfall for a prolonged period of time there is no water to evapotranspire, which holds especially for a semi-arid region like Rio Santiago.

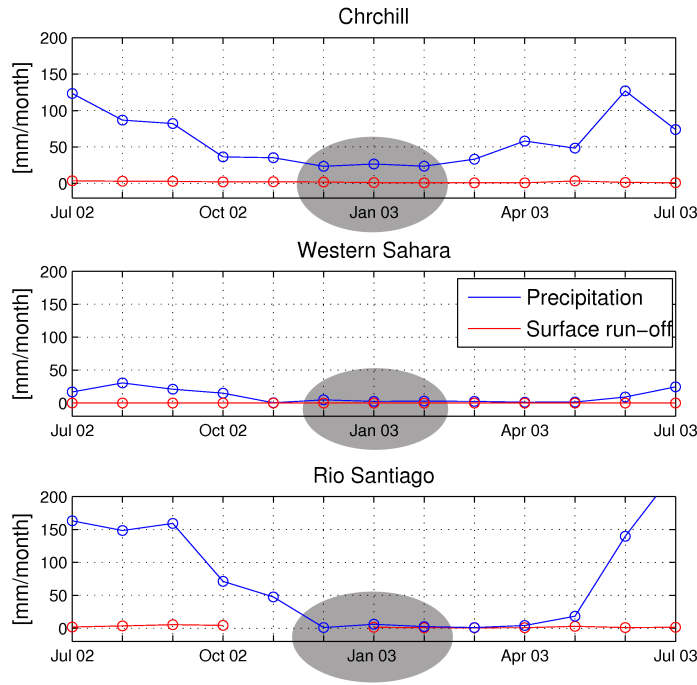


**Figure 6.2:** Precipitation (blue) and surface run-off (red) values for an arctic (top), a desert (middle) and a seasonal river basin (bottom), which met the constraints for a negligible evapotranspiration

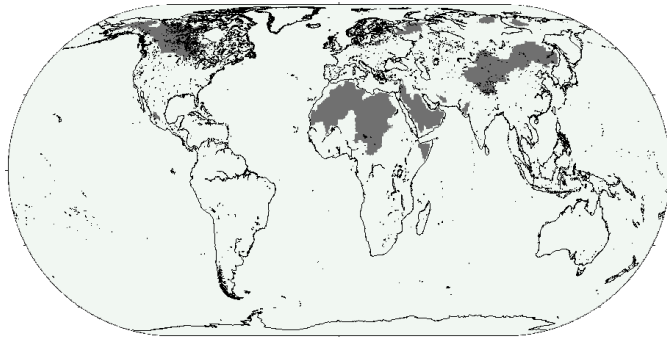


**Figure 6.3:** Catchments with negligible evapotranspiration during January 2003

An overview of the selected catchments is given in fig 6.3, which shows that most regions are located in the vast desert and near polar regions. One has to keep in mind that the selection of catchments with negligible evapotranspiration depend on the climatic conditions over a period of a month. Thus, the data from the mentioned regions has to be evaluated for each single month separately. A further way could be to use a monthly mean instead of the data of a single month, which would reduce the influence of potential errors in precipitation and run-off values.

Catchment	Area [10 <sup>6</sup> km <sup>2</sup> ]	P	R	$\partial S/\partial t$	std( $\partial S/\partial t$ )
				[mm/month]	
Amur	1953841	16.7	2.1	14.6	12.0
Anabar	79964	6.7	0.0	6.7	4.4
Aravalli (India)	180384	2.6	0.0	2.6	1.1
Churchill	300063	26.6	1.1	25.5	3.0
Gobi	2104175	4.9	0.0	4.9	1.7
Highland of Tibet	522766	2.3	0.0	2.3	2.1
Kazan	41037	7.7	9.1	-1.4	5.0
Kemijoki	53883	81.9	17.8	64.1	26.3
Lake Chad	3187889	2.5	0.0	2.5	1.9
Mackenzie	1669813	36.4	6.2	30.2	3.0
Mezen	54246	83.8	5.1	78.7	19.0
Nelson	1129006	16.6	8.0	8.6	10.7
Neman	90007	59.6	9.3	50.3	19.2
North China	62093	3.2	0.0	3.2	1.0
Northern Sahara	3474075	14.3	0.0	14.3	3.6
Olenek	200170	13.6	0.1	13.5	2.5
Pechora	305353	62.9	10.1	52.8	5.5
Rio Santiago	129863	6.0	1.5	4.5	17.7
Saudi Arabia	2403512	10.1	0.0	10.1	10.1
Severnaya Dvina	331450	78.0	8.2	69.8	16.9
Somalia	371005	0.7	0.0	0.7	6.0
South Iran	125039	9.6	0.0	9.6	25.1
Tarim	886074	0.9	0.0	0.9	1.9
Thelon	171730	6.2	8.7	-2.5	11.1
Western Sahara	1809508	2.6	0.0	2.6	0.6
Winisk	84716	17.6	8.7	8.9	19.1
Yana	221444	14.5	0.2	14.4	3.2
Yukon	821474	29.6	5.9	23.7	1.6

**Table 6.1:** Hydrological data for each constraining catchment from January 2003

Table 6.1 shows the storage changes and the residuals as well as the appropriate area of each of the catchments which met the requirements for a negligible evapotranspiration. It is here assumed that mass variations have an annual period. Thus, the variance of the data is defined as the difference of the observed precipitation and run-off value from a certain month and the mean of all available data of a certain catchment:

$$\sigma_H^2(\chi_{\text{Jan} 2003}) = \sigma_P^2(\chi_{\text{Jan} 2003}) + \sigma_R^2(\chi_{\text{Jan} 2003}) \quad (6.1.5)$$

where

$$\begin{aligned}\sigma_P^2(\chi_{\text{Jan} 2003}) &= (\bar{P}(\chi_{\text{Jan}}) - P(\chi_{\text{Jan} 2003}))^2 && \text{standard deviation of precipitation} \\ \sigma_R^2(\chi_{\text{Jan} 2003}) &= (\bar{R}(\chi_{\text{Jan}}) - R(\chi_{\text{Jan} 2003}))^2 && \text{standard deviation of run-off}\end{aligned}$$

The values  $\bar{P}(\chi_{\text{Jan}})$  and  $\bar{R}(\chi_{\text{Jan}})$  are the mean values of precipitation and run-off in January, computed from all available hydrological data.

## 6.2 Assimilating the GRACE solutions with hydrological mass estimates

### 6.2.1 A linear model for the hydrologic constraints

On the one hand, section 2.2 stated that storage changes can be expressed in water equivalent heights, which can be calculated by a set of spherical harmonic coefficients  $\dot{\tilde{K}}_{lm}$ . On the other hand, equation (6.1.3) holds that this deviation is simply the difference between precipitation and run-off and could be computed in terms of Legendre functions as

$$\frac{\partial S}{\partial t}(\chi) \approx \dot{h}(\chi, t) = \sum_{l=0}^{\infty} \Lambda_l \sum_{m=0}^l \tilde{Y}_{lm}(\chi) \dot{\tilde{K}}_{lm}(t) \quad (6.2.1)$$

where

- $\dot{\tilde{K}}_{lm}$  time-variable Stokes coefficients
- $\Lambda_l$  Isotropic spectral transfer coefficients
- $\tilde{Y}_{lm}(\chi)$  Legendre polynomials for the area  $\chi_i$
- $\dot{h}(\chi)$  Difference between precipitation and run-off of the catchment  $i$

As observations for precipitation and run-off are available for 28 catchments  $\chi$ , a linear model can be set up, in which the unknowns are the spherical harmonic coefficients  $\dot{\tilde{K}}_{lm}$  and the observations are the storage changes  $\dot{h}(\chi, t)$ . For the sake of simplicity, the following formulae are written in matrix notation:

$$E \left\{ \dot{h} \right\} = \mathbf{A}x; \quad D \left\{ \dot{h} \right\} = \sigma_H^2 \mathbf{Q}_H = \mathbf{P}_H^{-1} \quad (6.2.2)$$

where

- $E \left\{ \cdot \right\}$  expectation operator
- $D \left\{ \cdot \right\}$  dispersion operator
- $\mathbf{A} = \left[ \Lambda_l \tilde{Y}_{lm}(\chi) \right]$  design matrix
- $\sigma_H^2$  variance component of the hydrologic observations
- $\mathbf{Q}_H$  covariance matrix of the hydrologic observations

As (6.2.2) is overdetermined, the unknown parameters  $\hat{\mathbf{x}}$  can be obtained by minimizing the squared residuals

$$\hat{\mathbf{x}} : \min \left\| \mathbf{A}\mathbf{x} - \dot{\mathbf{h}} \right\|_{\mathbf{P}_H}^2 \quad (6.2.3)$$

This is achieved by the unbiased *least squares estimator*

$$\hat{\mathbf{x}} = \left( \mathbf{A}^\top \mathbf{Q}_H^{-1} \mathbf{A} \right)^{-1} \mathbf{A}^\top \mathbf{Q}_H^{-1} \dot{\mathbf{h}} \quad (6.2.4)$$

However, equation (6.2.15) won't deliver satisfactory solutions due to a very bad condition of the system of normal equations

$$\mathbf{N} = \mathbf{A}^\top \mathbf{Q}_H^{-1} \mathbf{A} \quad (6.2.5)$$

This bad condition can be explained by the fact that the sampling of the available hydrological data is very sparse. It was already mentioned that the data only covers less than 20% of the land mass and leads thus to a very inhomogeneous spatial distribution, which is concentrated in the vast desert and arctic regions. These characteristics of the underlying linear model deny an independent solution, as spherical harmonic analysis would require a data distribution throughout the Earth. However, this linear model can be used as stochastic constraint and thus adds further information to monthly GRACE solutions.

### 6.2.2 Combination of hydrologic storage changes and GRACE solutions

As a next step, the hydrological linear model from the last section needs to be combined with the time variable GRACE coefficients, which is achieved by formulating an equality constrained least squares problem, set up in a sequential estimation scheme. This approach is common in tasks, where one has to combine large scale linear systems in one model or when a linear model needs to be constantly updated with new data. The advantage is that old data needs not to be stored, but the linear model can be updated, as soon as new data flows in. Moreover, the single datasets need not to be processed together, but can be *sequentially* assimilated into the system. Now, one can combine the hydrologic observable model and the GRACE coefficients in one linear model:

$$\begin{aligned} E \left\{ \begin{pmatrix} \dot{\mathbf{h}} \\ \mathbf{x}_G \end{pmatrix} \right\} &= \begin{pmatrix} \mathbf{A} \\ \mathbf{I} \end{pmatrix} \mathbf{x}; \\ D \left\{ \begin{pmatrix} \dot{\mathbf{h}} \\ \mathbf{x}_G \end{pmatrix} \right\} &= \begin{pmatrix} \sigma_H^2 \mathbf{Q}_H & 0 \\ 0 & \sigma_G^2 \mathbf{Q}_G \end{pmatrix} \end{aligned} \quad (6.2.6)$$

where

- $\mathbf{x}$  unknown coefficients
- $\mathbf{A}$  design matrix
- $\mathbf{Q}_H$  covariance matrix of hydrologic observations
- $\dot{\mathbf{h}}$  vector of hydrologic observations
- $\mathbf{x}_G$  vector with GRACE coefficients
- $\mathbf{Q}_G$  covariance matrix of the GRACE coefficients

The unknown coefficients are estimated by minimizing the squared residuals

$$\hat{\mathbf{x}} : \min \left\| \mathbf{A}\mathbf{x} - \dot{\mathbf{h}} \right\|_{\mathbf{P}_H}^2 + \left\| \mathbf{x} - \mathbf{x}_G \right\|_{\mathbf{P}_G}^2 \quad (6.2.7)$$

which is done by the least squares estimator

$$\hat{\mathbf{x}} = \left( \mathbf{A}^T \mathbf{Q}_H^{-1} \mathbf{A} + \mathbf{Q}_G^{-1} \right)^{-1} (\mathbf{A}^T \mathbf{Q}_H^{-1} \dot{\mathbf{h}} + \mathbf{Q}_G^{-1} \mathbf{x}_G) \quad (6.2.8)$$

The appropriate covariance of the estimated coefficients is the inverse normal matrix:

$$\mathbf{Q}_{\hat{\mathbf{x}}} = \left( \mathbf{A}^T \mathbf{Q}_H^{-1} \mathbf{A} + \mathbf{Q}_G^{-1} \right)^{-1} \quad (6.2.9)$$

The solving of (6.2.8) has important advantages in two respects. On the one hand, the condition of the normal matrix (6.2.5) improves by adding further information to the linear model about the unknowns, which makes it possible to invert the system of hydrological normal equations with satisfactory results. On the other hand, the areas, where terrestrial observations are available, constrain the noisy GRACE coefficients in such a way that a series expansion with the estimated parameters will be consistent with the observed values in these regions and thus are assumed to impact on that part of the signal, which is initially contaminated with lots of noise.

### 6.2.3 Sequential estimation and variance component estimation

As most estimation problems in physical geodesy, the solving of (6.2.8) can't be done straightforward due to the huge dimension of the design matrix. Therefore, each catchment, which is used as constraint, is treated separately. This approach equals the so called *Multi-Observable Model* (Sneeuw, 2000), where different kinds of observations can be used for estimating the same parameters.

Usually, the sequential estimation is applied in the estimation process of large-scale geodetic networks, as it allows to constantly add new information or measurements without the necessity to store old data. Thus, the parameters can be re-estimated, every time new data comes in which normally happens in a temporal sense. On the other hand, the process could be regarded in a spatial sense as well. Hence, the mass deviation of each single catchment is treated as an independent observation group. This modifies the linear system (6.2.6) to

$$\begin{aligned} E \left\{ \begin{pmatrix} \dot{\mathbf{h}}_1 \\ \dot{\mathbf{h}}_2 \\ \vdots \\ \dot{\mathbf{h}}_n \\ \mathbf{x}_G \end{pmatrix} \right\} &= \begin{pmatrix} \mathbf{A}_1 \\ \mathbf{A}_2 \\ \vdots \\ \mathbf{A}_n \\ \mathbf{I} \end{pmatrix} \mathbf{x}; \\ D \left\{ \begin{pmatrix} \dot{\mathbf{h}}_1 \\ \dot{\mathbf{h}}_2 \\ \vdots \\ \dot{\mathbf{h}}_n \\ \mathbf{x}_G \end{pmatrix} \right\} &= \begin{pmatrix} \sigma_H^2 \mathbf{Q}_{H,1} & 0 & \dots & 0 \\ 0 & \sigma_H^2 \mathbf{Q}_{H,2} & & 0 \\ \vdots & & \ddots & \vdots \\ & & & \sigma_H^2 \mathbf{Q}_{H,n} & 0 \\ & & \dots & & \sigma_G^2 \mathbf{Q}_G \end{pmatrix} \end{aligned} \quad (6.2.10)$$

As each of the 28 constraining catchments  $\chi$  is represented by a whole set of  $k$  grid-cell centers  $(\theta_j, \lambda_j)$ ;  $j = 1, 2, \dots, k$ , the design matrix for a certain catchment is

$$\mathbf{A}_i = \Lambda_l \begin{pmatrix} \tilde{Y}_{lm}(\theta_1, \lambda_1) \\ \tilde{Y}_{lm}(\theta_2, \lambda_2) \\ \vdots \\ \tilde{Y}_{lm}(\theta_k, \lambda_k) \end{pmatrix}$$

The storage changes from hydrological estimates are area weighted averages. Thus, each computation point in one certain catchment is assumed to possess the same observation value, yielding the observation vector

$$\dot{\mathbf{h}}(\chi) = \dot{h}(\chi) (1 \ 1 \ \dots \ 1)^T \quad (6.2.11)$$

where the unit vector has the size of the number of computation points in the concerning catchment  $\chi$ .

To solve the linear system (6.2.10) it is possible, though, to compute a single normal matrix  $\mathbf{N}_\chi$  for each catchment:

$$\mathbf{N}_\chi = \mathbf{A}_\chi^T \mathbf{Q}_{H,\chi}^{-1} \mathbf{A}_\chi \quad (6.2.12)$$

Furthermore, the normal matrix of the hydrological constraints  $\mathbf{N}_H$  is obtained by adding up all specific normal matrices  $\mathbf{N}_\chi$ :

$$\mathbf{N}_H = \sum_\chi \mathbf{N}_\chi \quad (6.2.13)$$

This modifies the estimator (6.2.8) to the sequential estimator

$$\begin{aligned} \hat{\mathbf{x}} &= \left( \sum_\chi \mathbf{A}_\chi^T \mathbf{Q}_{H,\chi}^{-1} \mathbf{A}_\chi + \mathbf{Q}_G^{-1} \right)^{-1} \left( \sum_\chi \mathbf{A}_\chi^T \mathbf{Q}_{H,\chi}^{-1} \dot{\mathbf{h}}(\chi) + \mathbf{Q}_G^{-1} \mathbf{x}_G \right) \\ &= (\mathbf{N}_H + \mathbf{Q}_G^{-1})^{-1} \left( \sum_\chi \mathbf{A}_\chi^T \mathbf{Q}_{H,\chi}^{-1} \dot{\mathbf{h}}(\chi) + \mathbf{Q}_G^{-1} \mathbf{x}_G \right) \end{aligned} \quad (6.2.14)$$

By keeping in mind that the hydrologic observation group consists of a separate observation group for each of the 28 catchments, the notation from section 6.2.2 will be used for the rest of this thesis:

$$\hat{\mathbf{x}} = \left( \mathbf{A}^T \mathbf{Q}_H^{-1} \mathbf{A} + \mathbf{Q}_G^{-1} \right)^{-1} \left( \mathbf{A}^T \mathbf{Q}_H^{-1} \dot{\mathbf{h}} + \mathbf{Q}_G^{-1} \mathbf{x}_G \right) \quad (6.2.15)$$

In section 3.3.2 a method was discussed to estimate weight factors between different observation groups in one linear model. The same method is used here again to compute weight factors between the hydrological constraints and the GRACE coefficients. In this work, the same variance component is used for all hydrological constraints. A further method would be to estimate a separate variance component for each single catchment in order to increase the contribution of catchments, where the observations are very accurate. But that is not further discussed here.

Again, the VCE is applied by iterating the following four steps until the variance components converge:

1. Estimation of the unknown parameters according to equation (6.2.15)
2. Computation of the residuals in the different observation groups

$$\hat{\mathbf{e}}_H = \mathbf{A}\hat{\mathbf{x}} - \dot{\mathbf{h}}; \quad \hat{\mathbf{e}}_G = \hat{\mathbf{x}} - \mathbf{x}_G \quad (6.2.16)$$

3. Computation of the partial redundancies

$$r_H = n - \text{tr} \left( \frac{1}{\sigma_H^2} \mathbf{P}_H \mathbf{N}^{-1} \right) \quad (6.2.17a)$$

$$r_G = u - \text{tr} \left( \frac{1}{\sigma_G^2} \mathbf{P}_G \mathbf{N}^{-1} \right) \quad (6.2.17b)$$

The parameter  $n$  is the number of available data points of hydrological observations,  $u$  is again the number of Stokes coefficients

4. Computation of the variance components for each observation group

$$\hat{\sigma}_H^2 = \frac{\hat{\mathbf{e}}_H^\top \mathbf{P}_H \hat{\mathbf{e}}_H}{r_H} \quad (6.2.18a)$$

$$\hat{\sigma}_G^2 = \frac{\hat{\mathbf{e}}_G^\top \mathbf{P}_G \hat{\mathbf{e}}_G}{r_G} \quad (6.2.18b)$$

The convergence criterion is again set to

$$\left| 1 - \frac{\sigma^2(i)}{\sigma^2(i-1)} \right| < 10^{-5} \quad (6.2.19)$$

for both the variance components of the hydrological constraints and the GRACE coefficients.

## 6.3 Numerical experiments

### Spectral domain

In the following, the described method is tested with pure GRACE coefficients and regularized coefficients, which are filtered according to the formulae given in chapter 4. Their appropriate errors are taken out of the inverse normal matrix of the regularization procedure.

For both regularized and unregularized coefficients the variance components converge after 12 iterations, yielding a bigger weight for the hydrological constraints (cf. table 6.2). Obviously, if pure GRACE coefficients are used, the weight of their appropriate observation group is drastically decreased. This point is trivial, as the hydrological observations usually consist of values less than 100 mm/month. On the flipside, the GRACE coefficients yield mass variations with a magnitude of about 4500 mm/month. Thus, for a

serious impact of the constraints, the contribution of the GRACE coefficients must be decreased. This agrees with the weight factors, when regularized coefficients are used. As they possess a much lower signal in the spatial domain, they gain more weight through the variance component estimation. This means conversely that the constraints do not need a large weight factor to seriously contribute to the solution.

Coefficients	$1/\sigma_H^2$	$1/\sigma_G^2$	$\lambda = \sigma_G^2/\sigma_H^2$
unregularized	5.180	0.08	0.016
regularized	4.772	2.658	0.557

**Table 6.2:** Estimated variance components of the GRACE coefficients and the hydrological constraints

However, it was already mentioned that the hydrological observations contain not enough information, to invert the appropriate normal matrix in a stable way. Thus, the first question will be whether the combination of hydrological constraints and GRACE coefficients possesses a well-posed system of normal equations. This can be analyzed by looking at the eigenvalues of both observation groups and the resulting condition number.

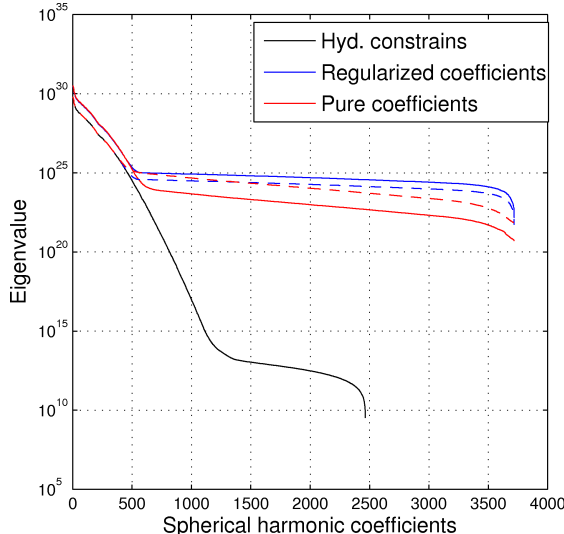


**Figure 6.4:** Eigenvalues of the normal matrix from the hydrological constraints (black) and the constrained GRACE coefficients (red and blue) with (straight lines) and without (dashed lines) estimated variance components

In figure 6.4, the eigenvalues of the hydrological constraints (black) and the constrained normal matrix (red and blue) are presented. The rapid decay towards zero of the eigenvalues of the normal matrix from the hydrological constraints  $N_H = \mathbf{A}^T \mathbf{Q}_H^{-1} \mathbf{A}$  as well as the resulting large condition number agrees with the assumption that  $N_H$  is ill-posed and can not be inverted in a stable way. Moreover, the sudden gap at about 2500 coefficients indicates rank-deficiency, which means that the hydrologic normal matrix does not contain enough information. On the other hand, all constrained normal matrices show

Matrix	Condition number	
	pure GRACE coefficients	regularized GRACE coefficients
$\mathbf{A}^T \mathbf{Q}_H^{-1} \mathbf{A}$	$5.399 \times 10^{20}$	$5.399 \times 10^{20}$
$\mathbf{Q}_G^{-1}$	16042	2856
$\mathbf{A}^T \mathbf{Q}_H^{-1} \mathbf{A} + \mathbf{Q}_G^{-1}$	$1.003 \times 10^5$	$1.189 \times 10^5$
$\frac{1}{\sigma_H^2} \mathbf{A}^T \mathbf{Q}_H^{-1} \mathbf{A} + \frac{1}{\sigma_G^2} \mathbf{Q}_G^{-1}$	$6.245 \times 10^6$	$2.073 \times 10^5$

**Table 6.3:** Condition numbers of the single matrices, which are involved in the linear model

a much smoother decay. Thus, one can assume the constrained least squares problem to be well-posed.

But figure 6.4 and table 6.3 show another interesting effect. If pure GRACE solutions are used, applying estimated variance components actually increases the condition number. This is trivial if the weight factors in table 6.2 are considered again. The GRACE coefficients gain very little weight, compared to the hydrological constraints. If one thinks about the ill-possessness of the appropriate normal matrix, it becomes clear that by increasing the weight of an ill-posed observation group, one introduces some of these uncertainties in the solution. On the other hand, the condition number increases only slightly with estimated variance components, if one uses regularized GRACE solutions. This can be explained with the weight factors of the hydrologic constraints as well. The contribution of the regularized GRACE coefficients is much larger than of pure GRACE coefficients. Thus, the introduced ill-possessness from the hydrologic normal matrix is compensated.

The impact of the constraints in the spectral domain is again roughly analyzed with the signal and error degree variances (cf. figure 6.5). The overall characteristic of the constrained spectrum is similar to the derived spectrum from the pure GRACE coefficients. However, one can see a little attenuation in the high frequency coefficients with  $l > 55$ . It was already mentioned that hydrologic constraints are assumed to have an impact especially on this part of the signal. On the other hand, the error degree variances are larger than before. This actually comes from the drastically increased weight of the hydrologic constraints. According to figure 6.4, the normal matrix of the constraints is ill-posed, yielding large errors after its inversion. Adding the GRACE covariance matrix as prior information stabilizes this system and allows one to invert the regularized normal matrix. However, the large weight of the constraints, compared to the drastically reduced weight of the GRACE coefficients, brings back some of this ill-possessness to the resulting normal matrix, which actually increases the *a posteriori* errors. This is emphasized by figure 6.5b, where the regularized degree variances before and after constraining are presented. It was already mentioned that regularized GRACE coefficients gain more weight in the linear model, when variance components are estimated, than pure GRACE coefficients. This actually means that the hydrologic constraints can improve the solution, while the ill-posedness of their appropriate normal matrix does not impact on

the solution. By keeping in mind that the regularized GRACE coefficients gained about half the weight of the hydrological constraints, the constrained degree variances show an deviation from the power law behavior from degree 40, while the overall noise power is attenuated. This actually is a positive effect, as the constraints obviously added some information, while the ill-possessness of their normal matrix does not impact on the solution. Moreover, the smaller errors in the constraints reduced the errors in the GRACE coefficients.

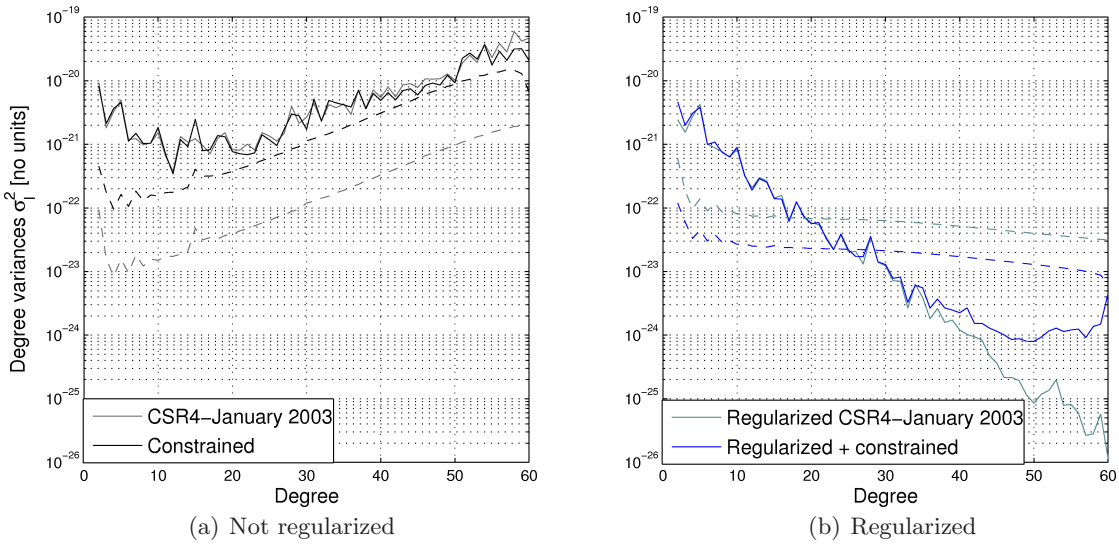


**Figure 6.5:** Degree variances of signal (straight line) and noise (dashed line) before and after constraining with pure GRACE coefficients (left) and regularized coefficients (right)

Unfortunately, the unfiltered and constrained signal and noise spectrum in figure 6.5a still shows a drastic increase with increasing degree. This already indicates that applying hydrological constraints indeed attenuates the signal-power in the high frequency coefficients, but the impact is not strong enough to seriously reduce the signal power amplification in the high frequency part of the GRACE spectrum.

On the flipside, adding constraints to regularized coefficients yields an overall attenuation of the errors, which leads to two conclusions. The hydrological observation group needs a low signal strength of the GRACE coefficients to seriously impact on the solution. The increasing signal strength in the high frequency part comes only from the constraints and is thus assumed to have a very low noise level. Additionally, the relative magnitude of the errors did not change, but the regularized and constrained overall noise power. However, one has to keep in mind that the regularized errors depend on the power law assumption. Nevertheless, the constraints are now strong enough, to reduce this power. These two points indicate that adding hydrological constraints seriously improves the quality of the GRACE coefficients by reducing the errors and adding reliable information in the high frequency part of the spectrum.

The already introduced redundancy contribution clearly indicates which of the estimated coefficients are mainly influenced by the hydrological constraints. Figure 6.6 confirms

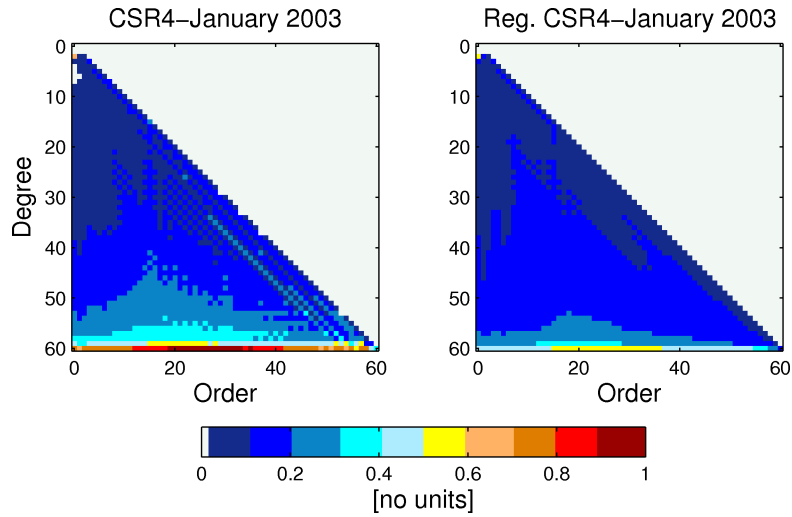


**Figure 6.6:** Spectral redundancy contribution of the hydrologic constraints when using pure GRACE (left) and regularized (right) coefficients

the assumption of an impact on the high frequency part of the signal, as the constraints mostly contribute to those coefficients with their degree being higher than 50 in both cases. Additionally, a closer look shows also a large contribution to the degree 2 coefficients.

However, the pure GRACE coefficients are more influenced than their regularized counterparts, especially in the tesseral part of the spectrum, which is in agreement with the estimated weight components. It was already mentioned that the constraints would need more weight to seriously impact on unfiltered GRACE coefficients. But the slight contribution of the constraints on regularized coefficients is not understood yet, as the degree variances painted a different picture.

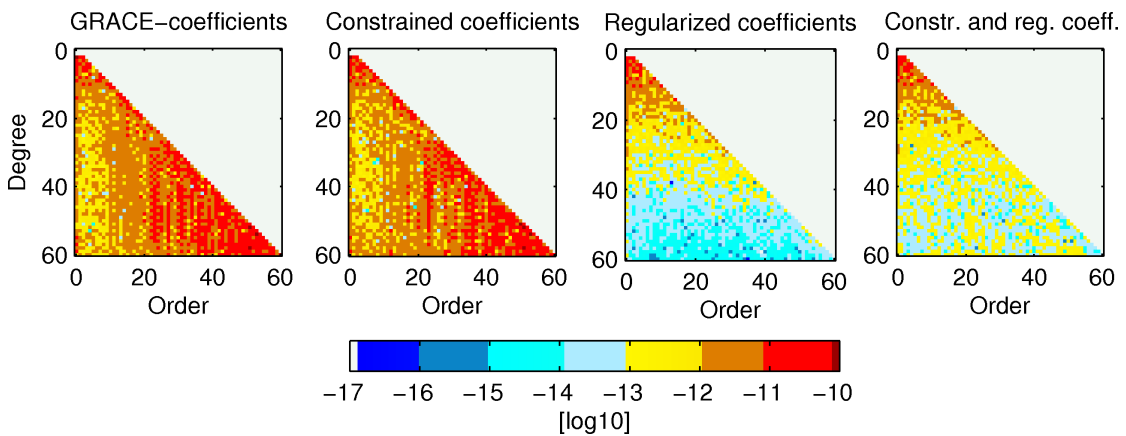


**Figure 6.7:** Constrained and unconstrained spherical harmonic coefficients

Figure 6.7 shows that the constraints amplify the signal strength, when regularized coefficients are used. This was already predicted by the degree variances, as they increased from degree 40. This effect causes the larger coefficients in the constrained and regularized spectrum. Moreover, the unconstrained regularized coefficients possess an almost

isotropic attenuation. Their constrained counterparts show a more or less constant spectral power in coefficients with their degree being larger than 20. On the other side, the constraints reduce the power of unfiltered GRACE coefficients, as the spectral signal strength of the tesseral coefficients with  $m > 10$  is slightly lower after constraining. This leads to the assumption that the true signal strength of the hydrological observations must lie somewhere in between.

### Spatial domain

Propagating the spectral redundancy contribution to the spatial domain yields the appropriate weight for each pixel in space and thus shows the spatial impact of the hydrological observation group. This can be done according to the error propagation formula (B.5) if one normalizes the propagated values in the spatial domain.

Figure 6.8 shows that the constraints mainly impact on their appropriate catchments. As the overall solution in these regions is influenced to nearly 80 - 90 %, it can be assumed that the noisy GRACE signal is nearly replaced. One has to keep in mind that unconstrained GRACE coefficients estimated mass variations with a magnitude of about 4500 mm/month. On the flipside, the hydrological observations mainly consist of rates of change smaller than 100 mm/month. If these values shall be recovered from the derived maps, it becomes obvious that the overall solution yields only little contribution of the GRACE coefficients in these catchments.

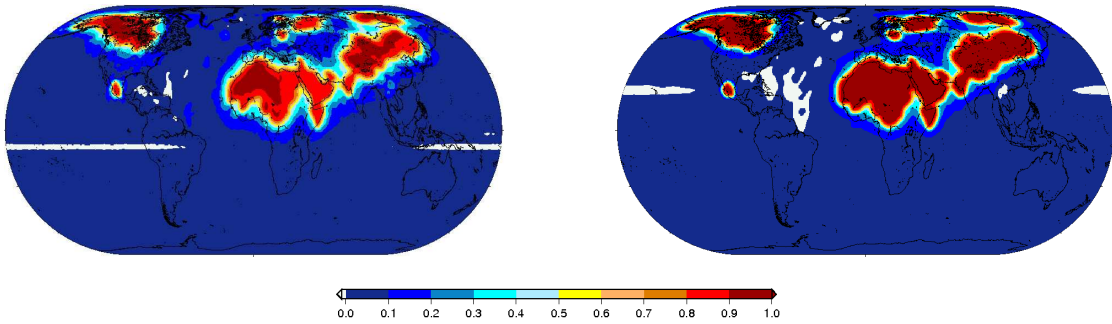


**Figure 6.8:** Propagated redundancy contribution of the hydrological observations for the constrained (left) and regularized and constrained (right) solution

The border regions are influenced as well, but the impact drops rapidly beyond the catchments, yielding a small global contribution of less than 20 %. However, the constraints seem strong enough to dominate in the vast continuous area between Northern Africa and Eastern Asia. This is also noticeable in the Northern American catchments, even if these areas are not completely covered with constraining catchments. Furthermore, using regularized coefficients results in large areas, where the hydrological constraints do not contribute at all.

These observations hold for both regularized and unregularized coefficients. This leads to an important conclusion. Even if the hydrological constraints gained more weight through the VCE, they have only very little influence on the regions beyond the con-

straining catchments. Their rapid attenuation could indicate that the observations can not be properly expanded in terms of Legendre functions, or, on the other hand, better modelling is needed.

The redundancy contribution of the unregularized solution already gave a rough impression that the regions beyond the involved catchments are still dominated with the regularized and unregularized GRACE coefficients. But propagating the estimated parameters to the spatial domain yields a complete recovery of the catchments, which were considered as constraining catchments (cf. figure 6.9). This can be concluded from the large continuous regions with a signal strength lower than 100 mm/month. Thus, the constraints really reduce the massive signal, which is assumed to be highly contaminated with noise.

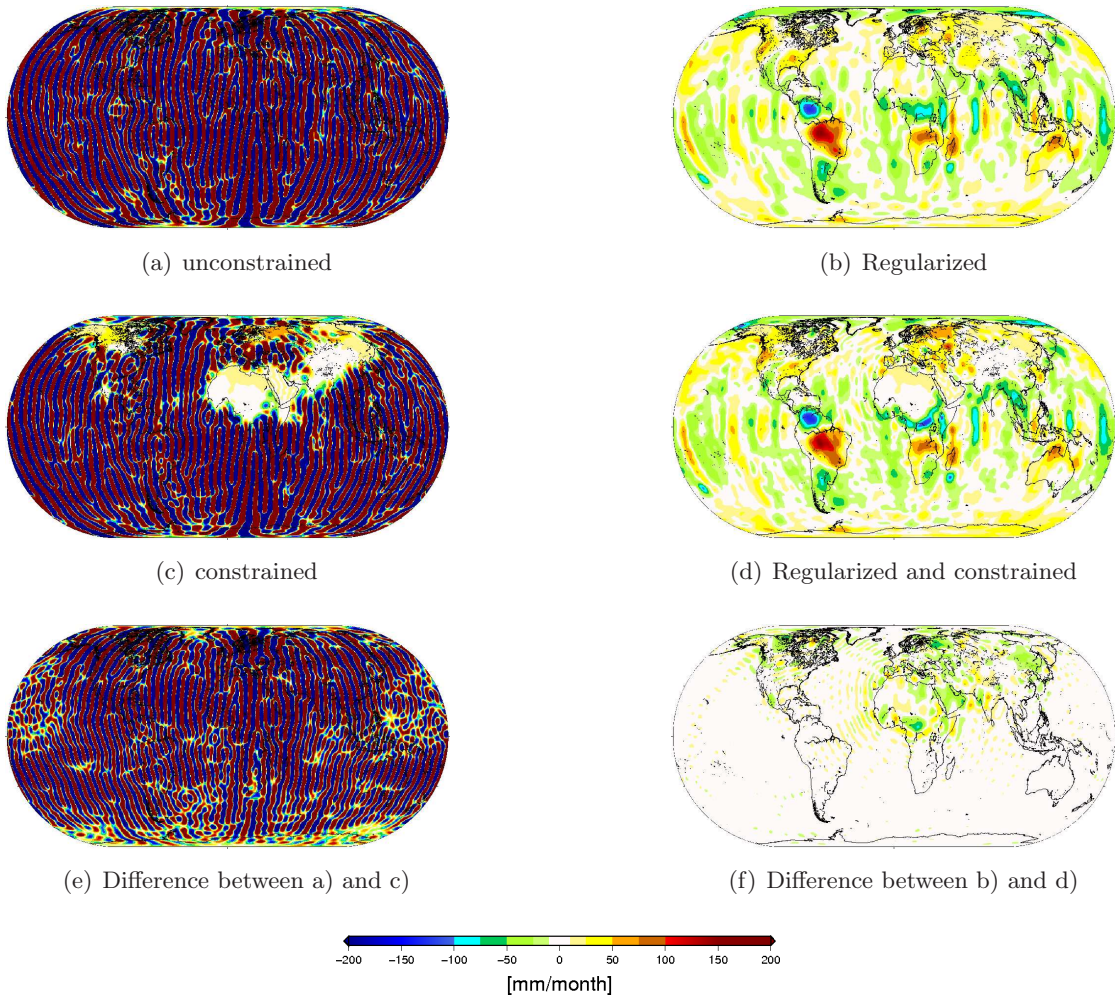


**Figure 6.9:** Derived maps from a) unconstrained, b) regularized, c) constrained and d) regularized and constrained coefficients

This happens actually in the constraining catchments, as well as in their border regions, which is obvious if e.g. the large continuous region from Northern Africa to Eastern Asia is regarded. Even if this area not completely consists of constraining catchments,

**Table 6.4:** Statistics of the derived maps in figure 6.9, in [mm/month]

field	RMS	mean	min	max
unconstrained solution (6.9a)	783.8	2.6	-4982.9	5135.6
constrained (6.9b)	688.7	1.5	-4651.0	4850.6
constrained - unconstrained (6.9c)	446.5	1.1	-3351.4	3099.5
regularized (6.9d)	26.2	-0.2	-129.6	151.2
constrained and regularized(6.9e)	27.6	1.1	-132.3	155.0
constrained - unconstrained (6.9f)	10.2	-1.3	-78.6	73.1

it shows everywhere a signal less than 100 mm/month in terms of water equivalent heights per month, which can be assumed as a realistic estimate. Moreover, the borders of the constraining regions are well identifiable, if e.g. the Northern African catchments are regarded. This effect will be analyzed in a following section. But even if the constrained result still possesses an unrealistic signal strength beyond the involved catchments, the procedure has a global impact, which can be told from 6.9c. This is consistent with the statistical values, given in table 6.4. Thus, the smaller statistics from the constrained solutions do not only come from the low signal in the constraining catchments, but also from a global reduction of the signal strength, which agrees with figure 6.8, as even the constraints slightly influence the regions beyond the involved catchments as well.

Figure 6.9f gives a rough impression about the spatial impact of the constraints. By regarding the Northern African catchments again, the constraints cause obviously circular artifacts, which spread with an oscillating amplitude. This indicates that they could be caused by the Gibbs phenomenon, which can be observed in the neighborhood of a saltus from a function, which is transformed in a finite sum of Legendre functions. If the figures 6.9b and 6.9d are compared, one can see that these deviations even influence the Amazon basin. Further experiments showed that this effect comes from the increased weight of the hydrological constraints through the variance component estimation. Thus, these artifacts should be further investigated, as they could give information about important characteristics of hydrologic constraints.

It was already shown that the spectral redundancy contribution can be propagated to the spatial domain, which yields the percentage contribution in each pixel of the concerning observation group (cf. equation (B.5)). Propagating a full covariance matrix basically allows to consider correlations between different points in space, but in this work, only the variances or rather the standard deviations in each pixel are regarded. The two maps in figure 6.10 show the standard deviations of pure and regularized constrained GRACE coefficients. Unfortunately, these figures can only be hardly compared, as the scales are completely different. However, using the same scale in both graphics would not have been representative.

The errors in the derived fields show similar characteristics, compared with the propagated signal itself. The constraining catchments are completely revealed and show much

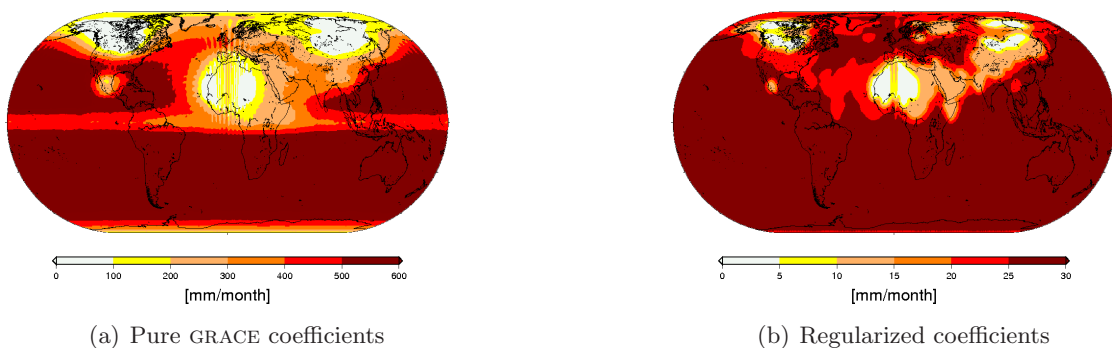


**Figure 6.10:** Propagated errors of the constrained solutions. Attention should be paid to the different color scales.

smaller errors than the regions beyond these catchments. However, using pure GRACE coefficients seems to attenuate the errors beyond the catchments as well. This is obviously not the case for regularized coefficients. It was already discussed that the contribution of hydrologic constraints is even more concentrated in the catchments, when regularized coefficients are used. The standard deviations paint a similar picture. The attenuation of errors happens only locally in the constraining catchments, while the global error level remains at about 30 mm/month. However, figure 6.10 shows a further interesting effect. Both graphics show a clear amplification of the errors in North Africa at zero longitude. This is even more obvious in 6.10a, where a circular continuation of these artifacts is visible near Western Europe. However, the origin of these patterns is not known yet.

The latter observations lead to two general conclusions. The major contribution of the constraints in the involved catchments is needed to seriously reduce the immense, and thus unrealistic, signal strength of unfiltered and unconstrained GRACE coefficients to the level of the hydrological observations. This explains the complete recovery of the involved catchments in the derived maps. But from the viewpoint of parameter estimation, this indicates that the both observation groups do not agree very well, which is trivial if the magnitude of the GRACE derived estimates and the hydrological observations are taken into account. If one uses regularized coefficients, both models should theoretically fit together, as the hydrological observations show similar values like the estimates from GRACE. Unfortunately, the constraints mainly impact on the involved catchments and cause circular artifacts around these regions. This effect and the slight global contribution could indicate that other base functions than the Legendre functions should be used to assimilate the GRACE solutions with hydrological observations.

The computed area weighted storage changes in the constraining catchments (cf. equation 2.2.20) are presented in figure 6.11. The constrained values are consistent with the hydrological observations, no matter if the coefficients are regularized or not. There is only a slight deviation in the Mezen and Thelon catchments due to their geographical position. This effect is explained in more detail in the following. These results are promising as no further filtering was applied to the constrained Stokes coefficients. However, one has to keep in mind that the hydrological constraints have a major contribution in these regions (cf. figure 6.8), and thus almost replace the GRACE coefficients.

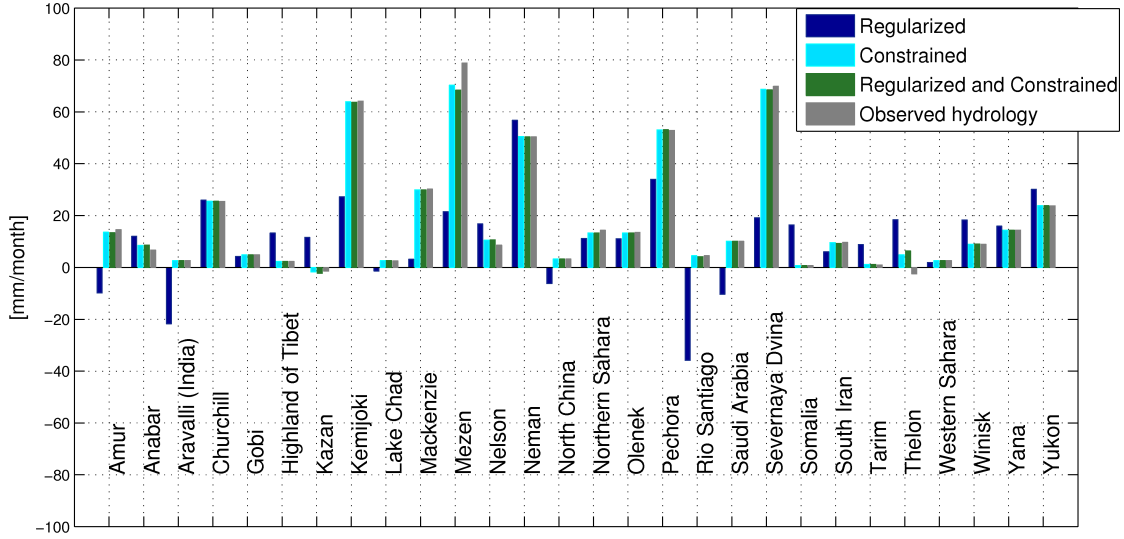


**Figure 6.11:** Estimated storage changes in water equivalent heights per month

Furthermore, it was mentioned in section 5.3 that the regularized mass estimates from GRACE agree with the predicted values from the GLDAS and observed hydrology in three of the catchments. Here, the solutions are validated with observed values from 28 catchments, and even if there are some differences, one recognizes a trend from the GRACE estimates to the observations. The occurring deviations might be caused by the size of the appropriate catchments, as a larger catchment generally has a higher influence on the solution and thus on adjacent catchments. Thus, it is sure to say that GRACE is able to detect mass variations, caused by hydrological phenomena.

### Cross validation of the results

The initial question was whether the hydrological constraints are strong enough to improve the quality of mass estimates from GRACE globally. It was already shown that the constraints mainly impact on their appropriate catchments and the adjacent regions. Thus, the involved catchments were completely recovered. The comparison of the estimated mass variations in figure 6.11 indeed showed consistency of the observations and the estimates. But there was an uncommon deviation from the observed value in some of the regions, i.e. Mezen and Thelon. Thus, some of the catchments, including these two, are removed from the observation vector. Afterwards, the estimated mass variations are compared with the observed hydrological data. If the discussed method should succeed, the values should be at least roughly consistent. It is obvious that this is not true for unfiltered GRACE coefficients, if e.g. the geographical location of the Rio Santiago basin is regarded. Thus, this experiment is only done with the regularized solution.

The catchments are now successively removed from the observation vector of the hydrological constraints. Therefore, they are selected in such a way that in each step one region of every large continuous constraining areas is removed, i.e. a North American catchment, a Central African Catchment, a catchment in Northern Europe and a catchment in Central Eurasia. A total of 11 catchments were removed in 3 steps, which are visualized in figure 6.3. First, Rio Santiago, Thelon, Northern Sahara and Mezen were

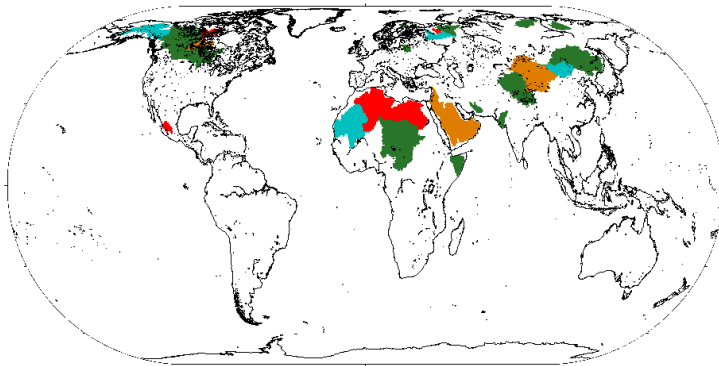


**Figure 6.12:** Catchments which are removed for cross validation

removed (red areas), followed by Yukon, Western Sahara, Northern China and Severnaya Dvina (blue areas). Finally, Saudi Arabia, Gobi and the Churchill basin were removed (orange areas). The remaining catchments are printed as green areas. Now, the whole procedure, which was discussed in section 6.2.2, is repeated with the modified observation vectors.

The constrained solutions are now used to derive maps of rates of change of water equivalent heights. These maps are presented in figure 6.13 and their differences in 6.14. Primarily, there are only slight differences between the single fields. However, especially the difference plots show again circular artifacts around the removed catchments (e.g. around North Africa), which might be caused by the already mentioned Gibbs phenomenon due to their oscillating signal and circular spread. These artifacts reach regions, which are located far beyond the constraining catchments. Thus, there is e.g. a little difference in the Amazon basin visible, if one compares the four maps in figure 6.13.

However, it can be assumed that this influence does not come from an improvement of the GRACE solution. It is rather a logical consequence of the way the constraints are applied. The catchments are represented through observed mass variations in very distinct regions. If such regions are transformed into terms of Legendre functions, the Gibbs pheonemon causes the signal in the derived field to oscillate. The amplitude increases with decreasing distance from the constraining region. This effect is visible around each large continuous area of constraining catchments, even if the amplitude differs. The maximum and minimum is visible in Saudi Arabia and Northern Europe, where the GRACE solution predicts a completely different mass variation than the observed values.

The derived statistics in table 6.5 show another interesting effect. There is obviously no trend towards the unconstrained solution visible, when the constraining catchments are successively removed, even if the deviations between the different constrained solutions increase, the more catchments are removed. This actually means that the global solution is independent from the amount, i.e. the area, of constraining catchments. If one constraints the GRACE solution, one recovers the used catchment and the regions beyond the catchments are influenced by the Gibbs phenomenon, which was caused by the transformation of this distinct area into terms of Legendre functions.

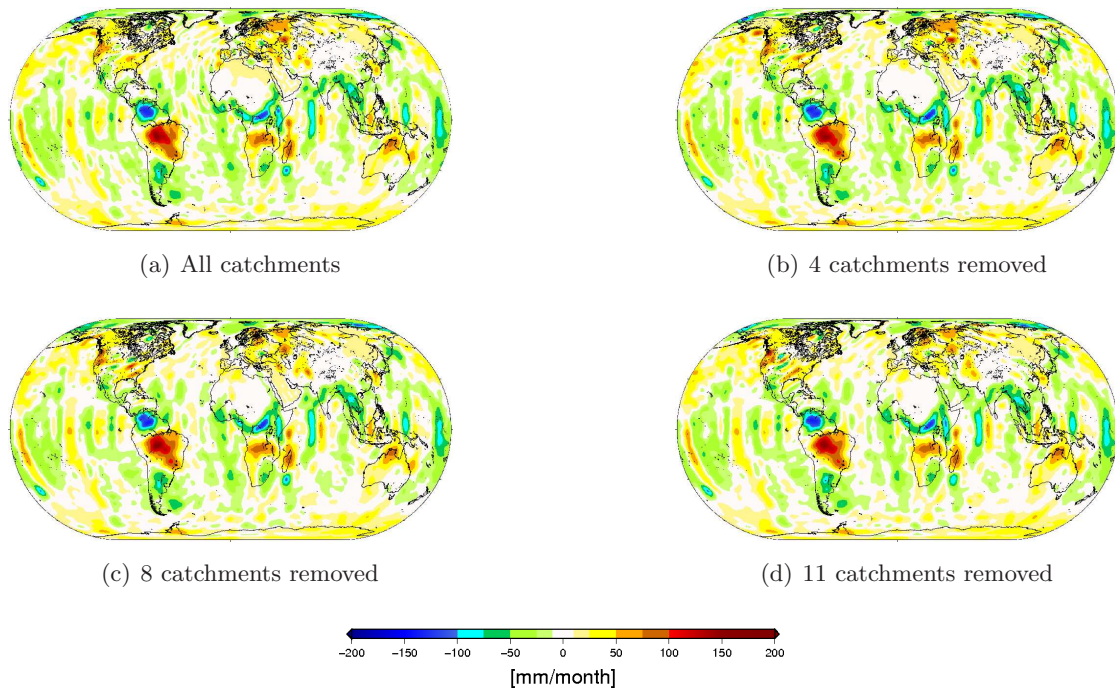


**Figure 6.13:** Derived maps from constrained monthly GRACE solutions with varying constraining catchments.

**Table 6.5:** Statistics of the derived maps in figure 6.13 and 6.14

field	RMS	mean	min	max
[mm/month]				
Regularized	26.2	-0.2	-129.6	151.2
All catchments	27.6	1.1	-132.3	155.0
4 catchments removed	27.9	1.6	-136.5	149.1
8 catchments removed	27.2	0.7	-138.1	156.7
11 catchments removed	27.5	1.4	137.2	148.6
Difference between a) and b)	6.9	-0.5	-101.6	62.6
Difference between a) and c)	8.3	0.3	-70.5	84.1
Difference between a) and d)	9.5	-0.3	-105.2	110.6

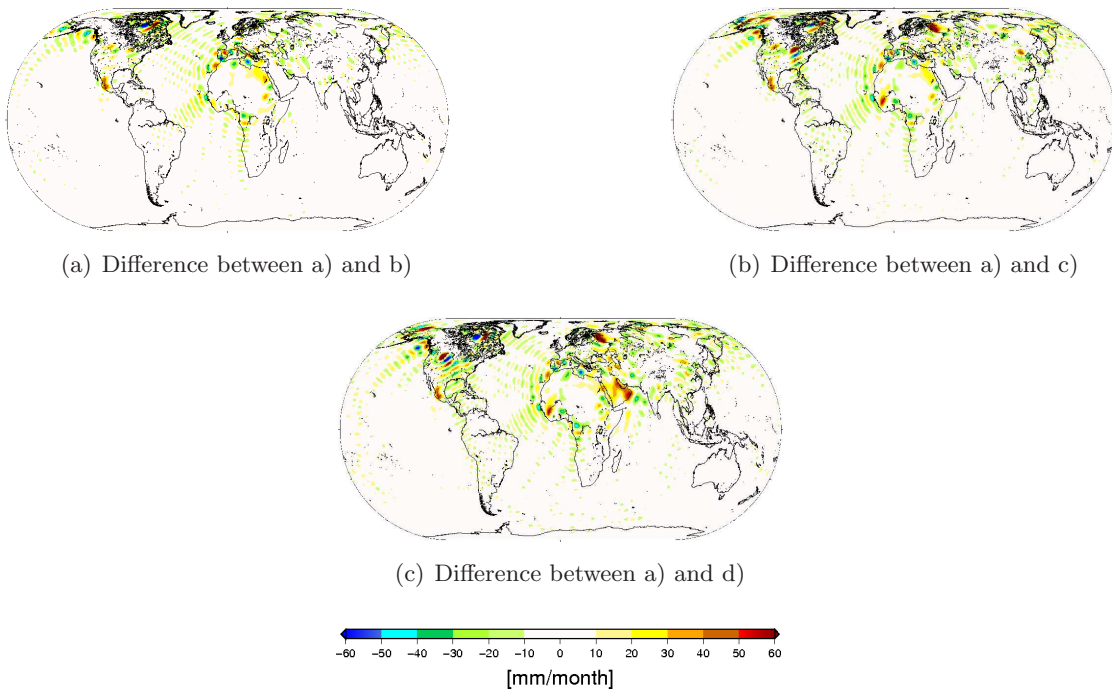


**Figure 6.14:** Differences between the derived maps in figure 6.13. Attention should be paid to the different color scales

A better look at the mentioned effects is given in figure 6.15, where the different solutions are again used to derive area averaged storage changes of the 28 catchments, which were used as constraints.

Figure 6.15 primarily shows a positive aspect of the discussed method. It seems as if the mass estimates in the remaining catchments are not influenced by the removal of some of them. This actually means that it does not matter how many catchments are used as hydrological constraints, but the observed mass estimates are always recovered. However, the estimate in Rio Santiago extremely differs if the catchment is used as constraint or not. This effect is visible in other catchments as well, e.g. Saudi Arabia or Severnaya Dvina. On the other hand, e.g. Churchill, Gobi and even Mezen show only little differences. This can be explained with the geographical position of these catchments. It was already mentioned that the hydrological constraints influence not only the appropriate catchments, but adjacent regions as well, even if the global impact is rather small. Those catchments which show only little differences if they are used as constraints or not are located near other constraining catchments, whereas e.g. Saudi Arabia or Rio Santiago are more or less separated regions. In other words, the mass estimate of a region tends to the observed value, if a constraining catchment is located nearby, otherwise it tends to the unconstrained solution.

This becomes even clearer if the three adjacent catchments Severnaya Dvina, Mezen and Pechora are considered. The observed value of Mezen is not reached, even if the catchment is used as constraint. It rather shows a mass estimate, which would agree with the observed value from Severnaya Dvina. After removing Mezen, the solution pre-

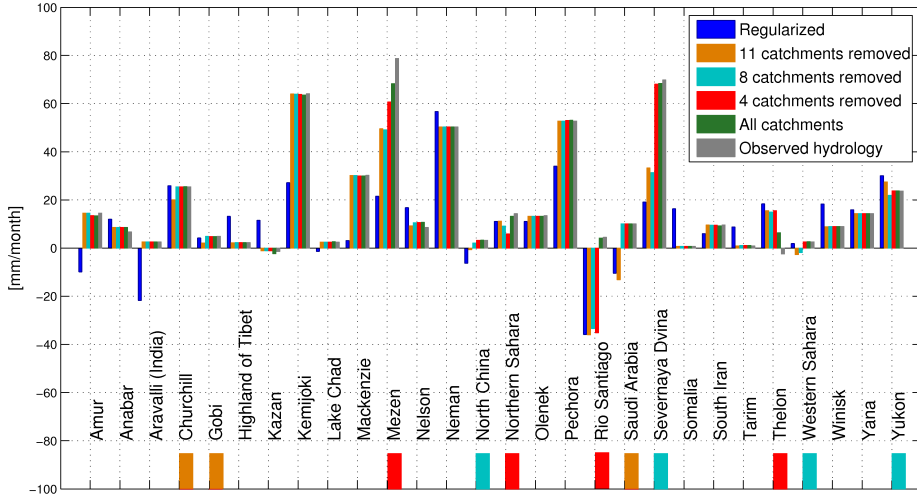


**Figure 6.15:** Estimated storage changes in water equivalent heights per month, the color at the bottom shows the step, in which the appropriate catchment was removed

dicts a mass variation of about 60 mm/month, which can be seen as a compromise between the value of Severnaya Dvina and Pechora. This can be assumed as both catchments are about the same size. In the next step, Severnaya Dvina is removed. Thus, the value of Mezen further reduces approximately to the observed storage change of Pechora (50 mm/month) but not to the unconstrained estimate (20 mm/month).

This effect clearly indicates that the hydrological constraints do not improve the GRACE solutions globally, but replace the mass estimate from GRACE in constraining catchments and adjacent regions with the observed value. Even if the storage changes of adjacent catchments are in some way correlated, one can not assume that this leads to realistic mass estimates, which agree with observed values. This leads to the general conclusion that adding constraints influences the regional estimates in such way that the signal beyond the involved catchments attenuates very rapidly, if no further constraining catchments are adjacent, yielding a negligible influence on far-off regions. In the border regions of two constraining catchments the resulting signal power is a superimpose of the observed hydrological storage changes from the concerning catchments, where vast regions generally dominate the results.

In this thesis, two methods of adding stochastic constraints to time-variable GRACE coefficients are discussed. The first method uses a degree variance model, which was computed according to the power-law theory of Kaula, to constrain the signal degree variances of monthly GRACE solutions to attenuate with increasing degree. The second approach constrains the GRACE solutions with hydrological observations in catchments with negligible evapotransporations. As both methods need prior error information about the GRACE coefficients, a method is presented to simulate a fully populated error covariance matrix.

Furthermore, a compilation of modern averaging functions is presented. Since the launch of the space gravimetry mission GRACE in the year 2002, some efficient tailor-made filters for smoothing the signal from such missions were invented. Thus, three of the most commonly used filters are discussed which basically use very different functional principles:

- The isotropic and anisotropic Gaussian filter
- The Wiener filter
- The decorrelated error filter

In section 3.3, a method is presented which is usually applied if one needs to invert an ill-posed system of normal equations, the regularization. It is shown that this approach can be used as a spectral filter, based on an equality constrained least squares estimation. However, the regularization and the Wiener filter need *a priori* knowledge about a desired output signal. The Wiener filter minimizes the deviations between the desired and the filtered signal whereas the regularization gives the variances of the Stokes coefficients an upper bound through such a desired signal. In this work, a method is discussed to estimate the desired signal, based on Kaula's rule. This means that the spectral signal power attenuates linearly with increasing degree in the logarithmic scale, according to a simple power law. Thus, one speaks of a degree variance model, as it depends only on the spherical harmonic degree. Such a power law is usually estimated by approximating the signal degree variances of a given spherical harmonic spectrum in a well defined band until the point, where the degree variances stop to attenuate and amplify again. It is shown that this approach results in very similar power law parameters, no matter which time series is chosen. This actually means that, according to the power law behavior,

even if the monthly signal degree variances from GRACE show varying characteristics, their theoretical power, given by the estimated degree variance model, i.e. the power law, remains more or less constant.

Thus, the following section concentrates on the impact of different power laws, which approximate the same time-series, but different maximal degrees. It is shown that especially the maximal degree of approximation is a similar parameter like e.g. the Gaussian averaging radius, even if it is less demonstrative. Approximating in a narrow low frequency band constrains the GRACE coefficients with a very steep power law, which gives lesser influence to higher frequency coefficients than a power law, which was approximated until a higher degree. However, it is shown that such a regularization indeed reduces the signal strength of the north-south stripes, but is not strong enough to produce a field, which possesses realistic amplitudes of mass variations.

As this whole approach assumes a weight between the GRACE coefficients themselves and the regularization term, which only depends on the appropriate *a priori* covariances, proper weight factors are estimated through a variance component estimation. These factors are defined as ratio between the *a posteriori* errors of a certain observation group and its contribution to the solution, represented through its redundancy number.

This technique is tested with different power laws as constraints, different GRACE covariance matrix structures as well as different monthly solutions. If one applies estimated variance components, the impact of different maximal degrees of approximation of the regularizing power law becomes of second order, as the remaining differences between the regularized solutions usually occur in the high frequency part of the spectrum and are thus negligible when propagated to the spatial domain.

However, the structure of the used GRACE covariance matrix indeed influences the solution. The approach is tested with a full, block diagonal and diagonal covariance matrix, which is obtained through the already mentioned energy balance approach. It is shown that using a full or block diagonal matrix shows nearly no differences neither in the spectral nor in the spatial domain. If one uses only variances, i.e. a diagonal covariance-variance matrix, the spectral quantities show only slight deviations to the other two versions but the derived fields are smoother in the equatorial regions, whereas using full and block diagonal covariance information yields smoother polar regions.

However, the regularized signal and error variances do not show such positive results, when the initially assumed accuracy of the GRACE mission is considered. According to the discussed approach, GRACE does not deliver useful time-variable information in coefficients with  $l > 20$ , as the rest of the spectrum is dominated with errors, yielding a maximal spatial resolution of about 1000 km of half wavelength. These findings agree with e.g. (Klees et al., 2008), where it was stated that an unambiguous distinction between signal and errors in areas with less than  $10^6 \text{ km}^2$  is not possible.

In chapter 5, the latter results of the regularization technique are compared with other already mentioned tailor-made filters. Furthermore, a reference model is taken from the GLDAS to validate the filtered fields. It is shown that the smoothed maps show similar

large scale signal characteristics and agree with the modelled mass variations from the GLDAS. However, the regularization filtered field shows signal amplitudes in very small areas as well, which agree with the GLDAS, which actually means that using this filter yields a better spatial resolution and a lesser soft-focussing effect than e.g. the Gaussian averaging operators. Unfortunately, it is also shown that there are some differences between the modelled and filtered mass variations. This means that it is still not possible, to use time-variable mass estimates from GRACE as reliable base observation. However, one has to keep in mind that GRACE is able to detect mass variations, which are not mapped by e.g. the GLDAS, due to their origin. Furthermore, one can assume that the models, which are used to remove the influence of the atmosphere and the oceans contain errors and uncertainties, yielding remaining contribution of these phenomena to the GRACE solutions. From that point of view, it is difficult to compare the time-variable estimates from GRACE with any other values. This problem is avoided in many other publications by validating the GRACE estimates with modelled quantities. However, it was initially assumed that GRACE would deliver data, which can be used to improve these models. Thus, such a validation must be handled with care, as the reliability of GRACE estimates is evaluated with quantities, which are modelled from partly inaccurate or disparate sources. It is shown that even the widely used GLDAS hydrology model shows differences to observed storage changes, given by hydrological data.

In the sixth chapter, a method is discussed which aims exactly at these problems. The monthly GRACE estimates are combined with observed hydrological data in an equally constrained least squares estimation procedure. Therefore, precipitation and run-off values from about 167 catchments are analyzed. 28 of these catchments met the characteristics of a negligible evapotranspiration for January 2003. Thus, the actual storage change of a certain catchment is given through the difference between precipitation and surface run-off. These regions are used to constrain monthly GRACE solutions. Again, the weight factors between the GRACE coefficients and the hydrological constraints are estimated by the already discussed variance component estimation.

It is shown that using unfiltered GRACE coefficients yields a field, in which the constraining catchments are clearly recoverable. Furthermore, the border regions are smoothed as well, but the unconstrained regions still show erroneous north-south stripes. However, the overall signal strength is indeed attenuated. In a further experiment, the method is tested with regularized coefficients. The result is very similar, as the constraining catchments are clearly recoverable. Analyzing the spatial redundancy contribution shows that the hydrologic constraints replace the GRACE signal in the constraining catchments, whereas their contribution drops suddenly beyond the borders. In the spectral domain, these constraints impact mainly on the higher frequency part of the spectrum, i.e. on coefficients with  $l > 50$ . These findings agree with a comparison of storage changes from the constrained GRACE solutions and observed hydrology. There are only very slight differences, when such constraints are used.

In a next step, the constraining catchments are successively removed. The constrained solutions are still consistent in the remaining catchments, but the removed catchments show a signal which tends to the unconstrained solution, if no further constraining region is adjacent. Otherwise, the signal in the removed regions is strongly influenced by the observed storage changes of the adjactend constraining catchments in such a way that

the observed storage change is assumed in the removed catchments as well. Moreover, it is shown that adding such constraints causes strong Gibbs phenomena around these catchments, which is obviously an unwanted effect.

Thus, it can be said that even if the first results looked quite promising, the method of adding hydrological constraints to monthly GRACE solutions does not yet seriously improve the quality of the GRACE estimates. However, it must be said that the basic principles of this method can be transposed to all kinds of different constraints. Thus, it is proposed to further investigate this method and use such constraints in cases, where observed quantities are of superior accuracy compared to the GRACE estimates. Additionally, the Gibbs phenomena around the constraining catchments could indicate that the discussed method should be tested with other base functions than the Legendre functions as well.

As a conclusion of this thesis it can be said that the time-variable GRACE solutions still do not meet the predicted accuracy, due to an unknown noise content in the provided data. Using averaging operators indeed improve the spatial characteristics of derived fields of e.g. a rate of change of water equivalent heights and show consistency with modelled mass variations and observed hydrological data. Unfortunately, a reasonable validation of mass variations, derived from the GRACE satellites, is still hardly realizable due to lacking global reference values. However, adding stochastic constraints is a promising method to improve the monthly GRACE solutions as it allows to add reliable information in such cases, where more accurate data is available.

## Bibliography

- Becker S (2004) *Smoothed spatial averaging in the interpolation of the time variable global gravity field*. Master's thesis, Institut für Theoretische Geodäsie, Rheinische Friedrich-Wilhelms-Universität Bonn.
- Bettadpur S (2007) *Level-2 Gravity Field Product User Handbook, The GRACE Project*.
- Bouman I, Koop R (1998) Regularization in gradiometric analysis. *Physics and Chemistry of the Earth* **23**:41–46.
- Bouman J (2000) *Quality assessment of satellite-based global gravity field models*. Tech. Rep. 48, Publications on Geodesy, Netherlands Geodetic Commission.
- Chen J, Wilson C, Famiglietti J, Rodell M (2005) Spatial sensitivity of the Gravity Recovery and Climate Experiment (GRACE) time-variable gravity observations. *Journal of Geophysical Research* **110**:B08408.
- Chow V, Maidment D, Mays L (1988) *Applied hydrology*. McGraw-Hill, New York.
- Devaraju B, Sneeuw N (2007) Stochastic averaging of GRACE data. In: *Geodätische Woche 2007*, 25–27 September 2007, DVW, Leipzig, Germany. Poster presentation.
- Devaraju B, Sneeuw N, Kindt H, et al. (2008) Constraining monthly GRACE-solutions with hydrological mass estimates. In: *Geophysical Research Abstracts*, vol. 10, pp. EGU2008-A-00761, EGU General Assembly 2008, Wien, Austria.
- Dziewonski A, Anderson D (1981) Preliminary reference Earth model. *Physics of the Earth and Planetary Interiors* **25**(4):297–356.
- Flury J, Rummel R (2004) Mass transport and mass distribution in the Earth system. In: *"GOCE, The Geoid and Oceanography", Proceedings of second international GOCE workshop*, ESA SP-569, Lacoste, H. (eds), Frascati, Italy.
- Fotopoulos G (2003) *An analysis on the optimal combination of geoid, orthometric and ellipsoidal height data*. Ph.D. thesis, Department of Geomatics Engineering, University of Calgary.
- Haagmans R, Van Gelderen M (1991) Error Variances-Covariances of GEM-T1: Their Characteristics and Implications in Geoid Computation. *Journal of Geophysical Research* **96**:11–22.

- Han D, Wahr J (1995) The viscoelastic relaxation of a realistically stratified earth, and a further analysis of postglacial rebound. *Geophysical Journal International* **120**(2):287–311.
- Han SC (2003) *Efficient global gravity determination from satellite-to-satellite tracking*. Ph.D. thesis, Department of Civil and Environmental Engineering and Geodetic Science, Ohio State University.
- Han SC, Shum CK, Jekeli C, et al. (2005) Non-isotropic filtering of GRACE temporal gravity for geophysical signal enhancement. *Geophysical Journal International* **163**:18–25.
- Jekeli C (1981) *Alternative methods to smooth the Earth's gravity field*. Tech. Rep. 327, Department of Geodetic Science and Surveying, The Ohio State University.
- Kaula WM (1966) *Theory of Satellite Geodesy: Applications of Satellites to Geodesy*. Blaisdell Publishing Company.
- Klees R, Revtova EA, Gunter BC, et al. (2008) The design of an optimal filter for monthly GRACE gravity models. *Geophysical Journal International* **175**:417–432.
- Koch KR, Kusche J (2002) Regularization of geopotential determination from satellite data by varaince components. *Journal of Geodesy* **76**:259–268.
- Kusche J (2007) Approximate decorrelation and non-isotropic smoothing of time-variable GRACE-type gravity field models. *Journal of Geodesy* **81**:733–749.
- Mayer-Gurr T (2007) ITG-Grace03s: The latest GRACE gravity field solution computed in Bonn. In: *Joint International GSTM and DFG SPP Symposium*, 15–17 October 2007, GFZ, Potsdam, Germany.
- Reigber C, Flechtner F, König R Meyer U, et al. (2002) GRACE - Eine Schwerefeld- und Klimamission. *Zweijahresbericht GeoForschungsZentrum Potsdam* pp. 109–118.
- Sasgen I, Martinec Z, Fleming K (2006) Wiener optimal filtering of GRACE data. *Studia Geoph et Geod* **50**:499–508.
- Seo K, Wilson C, Famiglietti J, et al. (2006) Terrestrial water mass load changes from Gravity Recovery and Climate Experiment (GRACE). *Water Resource Research* **42**:W05417.
- Sneeuw N (2000) *A semi-analytical approach to gravity field analysis from satellite observations*. Dissertationen, Technische Universität München, bei der Bayerischen Akademie der Wissenschaften.
- Sneeuw N (2005) Physical geodesy. Geodätisches Institut, Universität Stuttgart, Germany. Lecture notes.
- Swenson S, Wahr J (2006) Post-processing removal of correlated errors in GRACE data. *Geophysical Research Letters* **33**:L08402.
- Tikhonov A, Arsenin V (1977) *Methods for Solving Ill-Posed Problems*. Wiley, New York.
- Torge W (2001) *Geodäsie*. 2 edn., Walter de Gruyter. Berlin–New York.

- Wahr J, Molenaar M, Bryan F (1998) Time variability of the Earth's gravity field: Hydrological and oceanic effects and their possible detection using GRACE. *Journal of Geophysical Research* **103**(B12):30 205–30 229.
- Wahr J, Swenson S, Zlotnicki V, Velicogna I (2004) Time-variable gravity from GRACE: First results. *Geophysical Research Letters* **31**:L11 501.
- Xu P (1992) The value of minimum norm estimation of geopotential fields. *Geophysical Journal International* **111**:170–178.
- Zenner L (2006) *Zeitliche Schwerefeldvariationen aus GRACE und Hydrologiemodellen*. Diploma thesis, Institut für Astronomische und Physikalische Geodäsie, Technische Universität München.
- Zenner L, Gruber T (2008) Impact of Atmospheric & Oceanic Uncertainties on GRACE De-Aliasing Products. 23–27 June 2008, IAG International Symposium - Gravity, Geoid and Earth Observation, Chania, Greece.



# Mathematical description of the geoid | A

The gravity potential  $W$  of an arbitrary point defined in the Cartesian coordinate system  $P(x, y, z)$  can be described as the sum of the gravitational potential  $V$  and the centrifugal potential  $V_c$  (Torge, 2001)

$$\begin{aligned} W(x, y, z) &= V(x, y, z) + V_c(x, y, z) \\ &= G \int \int \int_{\Omega} \frac{\rho(x, y, z)}{r} dx dy dz + \frac{1}{2} \omega^2 (x^2 + y^2) \end{aligned} \quad (\text{A.1})$$

with

$x, y, z$	cartesian coordinates of the computation point
$G$	gravitational constant $G = 6.672 \cdot 10^{-11} m^3 s^{-2} kg^{-1}$
$\rho(x, y, z)$	local density
$r$	distance between the computation point and the center of the mass, i.e. the radius of the earth
$\omega$	angular velocity of the rotation of the earth.

Although the centrifugal acceleration, and thus the centrifugal potential, is determinable with high accuracy, the density is, if at all, known only at the surface of the earth. Additionally, the density distribution inside the earth is not homogeneous. This makes the determination of this parameter very difficult.

For a point  $(x, y, z)$  outside the earth, the Laplace equation must hold:

$$\Delta V(x, y, z) = 0 \quad (\text{A.2})$$

If this equation is written in spherical coordinates, it reads as

$$\Delta V(r, \theta, \lambda) = r^2 \frac{\partial^2 V}{\partial r^2} + 2r \frac{\partial V}{\partial r} + \cot \theta \frac{\partial V}{\partial \theta} + \frac{1}{\sin^2 \theta} \frac{\partial^2 V}{\partial \lambda^2} = 0 \quad (\text{A.3})$$

The set of base-functions which satisfy equation A.2 are called *Surface spherical harmonics*

$$\tilde{Y}_{lm}(\theta, \lambda) = \tilde{P}_{lm}(\cos \theta) \begin{Bmatrix} \cos m\lambda \\ \sin m\lambda \end{Bmatrix}$$

with

$\theta, \lambda$	spherical coordinates of the computation point
$\tilde{P}_{lm}(\cos \theta)$	associated normalized Legendre functions of the 1 <sup>st</sup> kind (see below)
$l, m$	spherical harmonic degree and order

These functions can be divided into three categories (Sneeuw, 2005):

- $m = 0$ : *zonal* spherical harmonics: the sine-part vanishes, and the cos-part becomes  $\cos 0\lambda = 1$ . This means that no variation occurs in longitude. The earth is divided into *zones*
- $l = m$ : *sectorial* spherical harmonics: there are  $2l$  sign-changes in longitude direction and zero in latitude direction; the earth is divided into *sectors*
- $l \neq m$ : *tesseral* spherical harmonics: they result in a pattern of *tiles* with alternating sign.

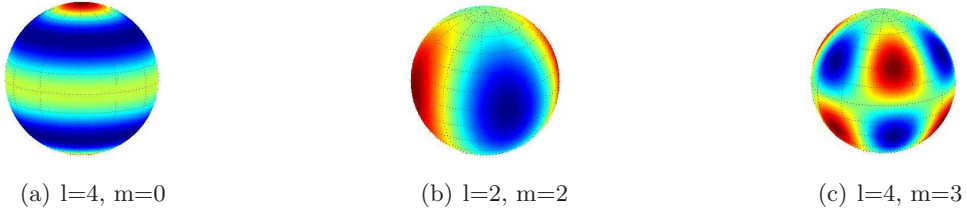


**Figure A.1:** zonal, sectorial and tesseral surface spherical harmonics

The Legendre functions  $\tilde{P}_{lm}(\cos \theta)$  can be calculated in different ways. In this work, only a numerical, recursive method is explained, which delivers a stable solution and is easily implementable into computer-algebra-systems.

The strategy to calculate a certain  $\tilde{P}_{lm}(\cos \theta)$  is to use the sectorial recursion to arrive at  $\tilde{P}_{mm}(\cos \theta)$ . Then use the second recursion to increase the the degree (Sneeuw, 2005):

$$\begin{aligned}\tilde{P}_{00}(\cos \theta) &= 1 \\ \tilde{P}_{mm}(\cos \theta) &= W_{mm} \sin(\theta) \overline{P}_{m-1,m-1}(\cos \theta) \\ \tilde{P}_{lm}(\cos \theta) &= W_{lm} \left[ \cos \theta \overline{P}_{l-1,m}(\cos \theta) - W_{l-1,m}^{-1} \overline{P}_{l-2,m}(\cos \theta) \right]\end{aligned}\tag{A.4}$$

with

$$W_{11} = \sqrt{3}, \quad W_{mm} = \sqrt{\frac{2m+1}{2m}}, \quad W_{lm} = \sqrt{\frac{(2l+1)(2l-1)}{(l+m)(l-m)}}\tag{A.5}$$

These functions can be divided into odd and even functions, depending on the parity of  $(l - m)$  :  $P_{lm}(-t) = (-1)^{l-m} P_{lm}(t)$ . The odd functions are equal to zero at the equator ( $\theta = 90^\circ$ ). A further important feature of the surface spherical harmonics is their orthonormality:

$$\frac{1}{4\pi} \iint_{\sigma} \overline{Y}_{lm}(\theta, \lambda) \overline{Y}_{nk}(\theta, \lambda) = \delta_{ln} \delta_{mk}\tag{A.6}$$

The  $\delta_{ij}$  is called *Kronecker delta function* which is defined as

$$\delta_{ij} = \begin{cases} 1 & \text{if } i = j \\ 0 & \text{if } i \neq j \end{cases} \quad (\text{A.7})$$

With these properties, it is possible, to express every function, which is defined on the surface of a sphere, as a combination of their spectral coefficients  $\tilde{C}_{lm}$  and  $\tilde{S}_{lm}$ . The relation between the coefficients and the function itself is given through the synthesis and analysis formulae:

$$\begin{aligned} \text{synthesis: } f(\theta, \lambda) &= \sum_{l=0}^{\infty} \sum_{m=0}^l \tilde{P}_{lm}(\cos \theta) (\tilde{C}_{lm} \cos m\lambda + \tilde{S}_{lm} \sin m\lambda) \\ \text{analysis: } \left\{ \begin{array}{c} \tilde{C}_{lm} \\ \tilde{S}_{lm} \end{array} \right\} &= \frac{1}{4\pi} \int \int f(\theta, \lambda) \tilde{Y}_{lm}(\theta, \lambda) d\sigma \end{aligned} \quad (\text{A.8})$$

As the gravity potential can be regarded as a two-dimensional function on the surface of a sphere, i.e. the earth, as well, it can be expressed in terms of the surface spherical harmonics. In this case, one speaks of spherical harmonic Stokes coefficients  $\tilde{C}_{lm}$  and  $\tilde{S}_{lm}$ .

$$V(r, \theta, \lambda) = \frac{GM}{R} \sum_{l=0}^{\infty} \left( \frac{R}{r} \right)^{l+1} \sum_{m=0}^l \tilde{P}_{lm}(\cos \theta) (\tilde{C}_{lm} \cos m\lambda + \tilde{S}_{lm} \sin m\lambda) \quad (\text{A.9})$$

where

$r, \theta, \lambda$	Spherical coordinates of the computation point
$G$	Gravitational constant
$M$	Mass of the earth
$R$	Radius of the earth
$\tilde{P}_{lm}(\cos \theta)$	Associated, normalized Legendre functions
$\tilde{C}_{lm}, \tilde{S}_{lm}$	Dimensionless spectral coefficients

Normally, the spectral coefficients have the same dimension as the function, i.e. the potential, itself. It is customary, though, to use dimensionless coefficients, which is achieved by the constant factor  $GM/R$  (Sneeuw, 2005).

### Normal potential and geoid heights

**The Geoid** The geoid is defined as equipotential surface of the earth's gravity field, which coincides with the mean sea level of the oceans (Torge, 2001). This definition assumes the water masses to be temporally invariant and only affected by the gravity. Thus it can be imagined as surface of the idealized oceans which is continued underneath the continents. According to Gauss-Listing, it is defined as the equipotential surface of the Earth's gravity field which best fits, in a least squares sense, global mean sea level. This is actually the adopted definition of the National Geodetic Survey (NGS).

**The normal field** It is obvious, that this definition makes an exact analytical mathematical description of the geoid nearly impossible. Therefore, a new surface is invented, the so called *normal field*. This field is an ellipsoidal approximation to the real gravity field (Sneeuw, 2005). It is usually described through 4 parameters:

- Semi major axis  $a$
- Flattening  $f = \frac{a-b}{a}$
- Potential at the surface of the field  $U_0$
- Angular velocity  $\omega$

Depending on the application, there are many different realizations of such a normal field. For global tasks, one would choose an ellipsoid which approximates the real geoid best, whereas for local applications, an ellipsoid is chosen which optimally approximates the geoid in a local area.

The potential that deviates from the normal potential is called *disturbing potential*. In other words, the gravity potential can be described using the normal potential with potential deviations from  $W$  treated as disturbances:

$$W = U + T \quad (\text{A.10})$$

where

- |     |                        |
|-----|------------------------|
| $W$ | full gravity potential |
| $U$ | normal potential       |
| $T$ | disturbing potential   |

As the normal potential is known, the next step is to describe the disturbing potential, which can be formulated in terms of the spherical harmonics as well:

$$T = \frac{GM}{r} \sum_{l=0}^{\infty} \left(\frac{R}{r}\right)^{l+1} \sum_{m=0}^l \tilde{P}_{lm}(\cos \theta) (\Delta \tilde{C}_{lm} \cos m\lambda + \Delta \tilde{S}_{lm} \sin m\lambda) \quad (\text{A.11})$$

Here,  $\Delta \tilde{C}_{lm}$  and  $\Delta \tilde{S}_{lm}$  are defined as the difference between the coefficients of the real potential  $\tilde{C}_{lm}, \tilde{S}_{lm}$ , which can be obtained by measuring the orbit perturbations of satellites, and the coefficients of the normal potential  $\tilde{c}_{lm}, \tilde{s}_{lm}$ .

The connection between this disturbing potential and the geoid heights is given through the equation of Bruns:

$$N = \frac{T}{\gamma} \quad (\text{A.12})$$

This means that the normal-height, i.e. the metric distance between the geoid and the normal-ellipsoid, is given through the quotient of the disturbing potential and the normal potential at the computation point. A formula for the normal-heights in terms of spherical harmonics is easily found if equation A.11 is inserted into equation A.12:

$$N = \frac{GM}{\gamma r} \sum_{l=0}^{\infty} \left(\frac{R}{r}\right)^{l+1} \sum_{m=0}^l \tilde{P}_{lm}(\cos \theta) (\Delta \tilde{C}_{lm} \cos m\lambda + \Delta \tilde{S}_{lm} \sin m\lambda) \quad (\text{A.13})$$

By knowing that  $\gamma = \frac{GM}{r^2}$ , and assuming that the computation point is on the surface of the earth, equation A.13 becomes

$$N = R \sum_{l=0}^{\infty} \sum_{m=0}^l \tilde{P}_{lm}(\cos \theta) (\Delta \tilde{C}_{lm} \cos m\lambda + \Delta \tilde{S}_{lm} \sin m\lambda) \quad (\text{A.14})$$

With this equation we have the possibility to compute a complete geoid model only from the spherical harmonic coefficients  $\tilde{C}_{lm}$  and  $\tilde{S}_{lm}$ .

There are further methods available for the computation of a geoid, e.g. the so called *Stokes integration*. For a detailed illustration of this approach, see (Sneeuw, 2005).



## Error propagation | B

The errors in monthly GRACE solutions are usually provided as standard deviations of the Stokes coefficients. However, section 4.2 deal with a method to simulate a fully populated error matrix for GRACE coefficients. As it is evident to regard the noise level in the spatial domain as well, the spectral error covariance needs to be propagated to the spatial domain, yielding the variance in each grid point of a derived field. This theory is mainly based on (Haagmans & Van Gelderen, 1991), where such a propagation was done to derive the spatial errors in geoid computations.

A function  $\mathbf{f}$ , which is defined in the spectral domain, i.e.  $\mathbf{f} = [f_{lm}]$  is usually propagated through

$$\mathbf{f}(\theta, \lambda) = \tilde{\mathbf{Y}}(\theta, \lambda) \mathbf{f} \quad (\text{B.1})$$

which actually reads as

$$f(\theta, \lambda) = \sum_{l,m} \beta_{lm} \tilde{P}_{lm}(\cos \theta) \left( \tilde{C}_{lm} \cos m\lambda + \tilde{S}_{lm} \sin m\lambda \right) \quad (\text{B.2})$$

where

$b_{lm}$	eigenvalues, e.g. isotropic transfer coefficients
$f(\theta, \lambda)$	functional in the spatial domain
$\tilde{P}_{lm}(\cos \theta)$	normalized associated Legendre functions
$\tilde{C}_{lm}, \tilde{S}_{lm}$	spherical harmonic coefficients

The error covariance of the functional  $f_{lm}$  is defined as  $\mathbf{Q}_f = [Q_{lml'm'}]$ . Thus, it contains not only the errors of one particular spherical harmonic coefficients, but the appropriate correlations between coefficients as well. The propagation to the spatial domain can be written as

$$\mathbf{Q}_{f(\theta, \lambda, \theta', \lambda')} = \tilde{\mathbf{Y}}(\theta, \lambda) \mathbf{Q}_f \tilde{\mathbf{Y}}(\theta, \lambda')^\top \quad (\text{B.3})$$

According to equation B.2, the two-dimensionsal Fourier expansion for the error covariances (Bouman, 2000; Haagmans & Van Gelderen, 1991) one may write

$$\begin{aligned} \text{cov}(\theta, \lambda, \theta', \lambda') &= \sum_{m=0}^L \sum_{k=0}^L [A_{mk} \cos m\lambda \cos k\lambda + B_{mk} \sin m\lambda \cos k\lambda' \\ &\quad + C_{mk} \cos m\lambda \sin k\lambda' + D_{mk} \sin m\lambda \sin k\lambda'] \end{aligned} \quad (\text{B.4})$$

with the Fourier coefficients of the Fourier expansion of the error covariances

$$\begin{aligned} A_{mk} &= \sum_{l=m}^L \sum_{n=k}^L \beta_l \beta_n \text{cov} \left( \tilde{C}_{lm}, \tilde{C}_{nk} \tilde{P}_{lm}(\cos \theta) \tilde{P}_{nk}(\cos \theta') \right) \\ B_{mk} &= \sum_{l=m}^L \sum_{n=k}^L \beta_l \beta_n \text{cov} \left( \tilde{S}_{lm}, \tilde{C}_{nk} \tilde{P}_{lm}(\cos \theta) \tilde{P}_{nk}(\cos \theta') \right) \\ C_{mk} &= \sum_{l=m}^L \sum_{n=k}^L \beta_l \beta_n \text{cov} \left( \tilde{C}_{lm}, \tilde{S}_{nk} \tilde{P}_{lm}(\cos \theta) \tilde{P}_{nk}(\cos \theta') \right) \\ D_{mk} &= \sum_{l=m}^L \sum_{n=k}^L \beta_l \beta_n \text{cov} \left( \tilde{C}_{lm}, \tilde{S}_{nk} \tilde{P}_{lm}(\cos \theta) \tilde{P}_{nk}(\cos \theta') \right) \end{aligned} \quad (\text{B.5})$$

Depending on the structure of the covariance matrix, these equations can be simplified. If one neglects correlations between coefficients with different order, one obtains a block diagonal covariance matrix and thus  $B_{mk} = C_{mk} = 0$  and  $m = k$ . The propagated error is now denoted as  $\text{var}(\theta, \lambda)$ , since it is a function of one point only (Bouman, 2000):

$$\text{var}(\theta, \lambda) = \sum_{m=0}^L [A_m \cos^2 m\lambda + D_m \sin^2 m\lambda] \quad (\text{B.6})$$

with

$$\begin{aligned} A_m &= \sum_{l=m}^L \sum_{n=m}^L \beta_l \beta_n \text{var} \left( \tilde{C}_{lm}, \tilde{C}_{nm} \tilde{P}_{lm}(\cos \theta) \tilde{P}_{nm}(\cos \theta) \right) \\ D_m &= \sum_{l=m}^L \sum_{n=m}^L \beta_l \beta_n \text{var} \left( \tilde{C}_{lm}, \tilde{S}_{nm} \tilde{P}_{lm}(\cos \theta) \tilde{P}_{nm}(\cos \theta) \right) \end{aligned} \quad (\text{B.7})$$

The errors can be reduced down to the level of error degree variances, which simplifies indeed the computational effort, but neglects all correlations between the coefficients and is thus not proposed.

# Methods for a spherical harmonic error analysis

C

## C.1 Eigenvalue analysis for measuring ill-conditioning

One problem of solving least squares problems is the inversion of the normal matrix with stable solutions due to its bad condition. It would be helpful, though, if one could be able to "measure" the ill-conditioning of such a matrix. This can be done by an eigenvalue analysis.

First, it must be decided, if the matrix is really ill-conditioned, or rank deficient. There are two criteria which must be met, if a least squares problem is ill-posed:

- the eigenvalues of the normal matrix gradually decay towards zero,
- the normal matrix has a large *condition number*
- the normal matrix must be of full rank

This condition number is the ratio between largest and smallest eigenvalue and gives information about the maximal amplification of an error in the input-data, i.e. a large condition number means that a small error in the input-data can result in a large error in the output-data. Its logarithm determines the loss of valid digits due to noise amplification.

Its computation is based on the singular value decomposition of a matrix  $\mathbf{A}$ , which is usually defined as

$$\mathbf{A} = \mathbf{U}\Sigma\mathbf{V}^* \quad (\text{C.1})$$

where

- $\mathbf{A}$  complex  $m \times n$  matrix  
 $\mathbf{U}$  unitary  $m \times m$  matrix  
 $\mathbf{V}^*$  adjoint  $n \times n$  matrix of the unitary matrix  $\mathbf{V}$   
 $\Sigma$  real valued  $m \times n$  matrix with the singular values  $\sigma_i$  of  $\mathbf{A}$

Then, the condition number is given through

$$\kappa = \frac{\max \sigma_i}{\min \sigma_i} \quad (\text{C.2})$$

## C.2 Spectral error analysis

### C.2.1 Absolute Error Measures

The inverse of the normal matrix  $\mathbf{Q}_{\hat{x}} = \mathbf{N}^{-1}$  allows conclusions, if and to what extend the equalization brought improvements to the accuracy of the estimated parameters. As this matrix is the variance-covariance matrix of the unknown parameters, its main diagonal contains the variances per coefficient:

$$\text{diag} \mathbf{Q}_{\hat{x}} = \sigma_{lm}^2 \quad (\text{C.1})$$

An adequate way to display this spectrum is the spherical harmonic triangluar schmeme, which will be used in the analysis of the results.

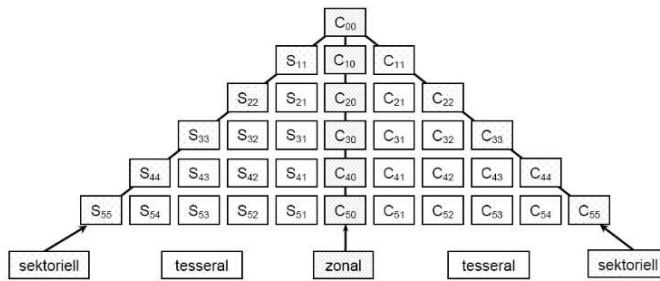


**Figure C.1:** Triangular scheme of spherical harmonic coefficients

But it is obvious, though, that such a visualization only allows a rough analysis. Thus, further measurements are intended for the purpose of comparison. As we assume the error spectrum to be isotropic, i.e. the spectrum is independent from the order  $m$ , there are two one-dimensional, degree-dependand error measures:

- The degree variances

$$\sigma_l^2 = \sum_{m=-l}^l \sigma_{lm}^2 \quad (\text{C.2})$$

This value is the total error power of a certain degree  $l$ . It is simply the sum of all elements in one row in the spherical harmonic triangular scheme.

- root-mean-square per degree (RMS $_l$ )

$$\text{RMS}_l = \sqrt{\frac{1}{2l+1} \sigma_l^2} = \sqrt{\frac{1}{2l+1} \sum_{m=-l}^l \sigma_{lm}^2} \quad (\text{C.3})$$

The RMS can be seen as average standard deviation, which is expected for each single coefficient. Its square would be the mean variance per degree.

### C.2.2 Relative Error Measures

The upper two error measures are both absolute values as they represent the absolute error in the coefficients. But in many cases, it is useful to regard the error as a relative value. Thus, two further measures are often applied to evaluate the quality of estimated

parameters, which can either be computed as one-dimensional, i. e. isotropic, or two-dimensional error measures:

- Signal-to-noise-ratio (SNR)

$$\text{1D : } \text{SNR}_l = \frac{c_l}{\sigma_l} \quad \text{2D : } \text{SNR}_{lm} = \frac{|K_{lm}|}{\sigma_{lm}} \quad (\text{C.4})$$

- Gain

$$\text{1D : } g_l = \frac{\sigma_l^{\text{old}}}{\sigma_l^{\text{new}}} \quad \text{2D : } g_{lm} = \frac{\sigma_{lm}^{\text{old}}}{\sigma_{lm}^{\text{new}}} \quad (\text{C.5})$$

Gain gives information about the amplification of an error spectrum relative to another spectrum, e.g. an a priori spectrum.

These error measures allow the determination of the part of a given spectrum, which delivers useful information and the part, which is dominated by noise. In fact, a signal is assumed to be dominated with noise if  $\text{SNR}_l < 1$ .

### C.2.3 Redundancy Contribution

In a multi-observables-model, it would be interesting, to what extend each of the observables contribute to the final solution and which parameters were affected the most. This comes from the fact, that, depending on the *a priori* covariance, the observation groups in one linear model might gain too much or not enough contribution. Therefore, one can compute the so called *redundancy contribution* of the different observables. In this case, it is even possible to compare the influence of the hydrological mass constraints, the prior information, i.e. the GRACE-coefficients and the Kaula rule.

To be distinguished from the already discussed redundancy numbers, which give information about the contribution to the effective dimension of parameter space, for each each subset  $y_n$  a contribution matrix is defined (Sneeuw, 2000; Bouman, 2000)

$$R_n = N^{-1}N_n \quad (\text{C.6})$$

The diagonal of  $R_n$  with  $\text{diag}(R_n) = r_{lm}^n$  gives information about the partial contribution of each subset to the resulting parameters  $K_{lm}$ . Thus, each  $r_{lm}^n$  is the procentual contribution of the subset  $R_n$  to a single spherical harmonic coefficient  $K_{lm}$ .

If one assumes estimated variance components  $\sigma_n^2$  between the single observation groups, the equation reads as

$$R_n = \frac{1}{\sigma_n^2} N^{-1}N_n \quad (\text{C.7})$$

These quantities can be propagated in the spatial domain, according to the formulae of chapter B. Then, the result shows the contribution of a observation group to each point in space.



# List of MATLAB programs and output data | D

## Simulation of an error covariance matrix

blddsgn.m	Builds a design matrix for given satellite positions (B. Devaraju)
blockinv.m	Computes the block inverse of a matrix (B. Devaraju)
cart2spher.m	Transformation of cartesian into spherical coordinates
covar_scale.m	Scales a simulated covariance matrix with formal or calibrated errors, which were provided by the CSR
grcnrml.m	Simulates the GRACE covariance matrix based on the position of the two satellites (B. Devaraju)
readpos.m	Reads position data from the GRACE files, which was converted by the GRACE read software

## Validation functions

area.m	Computation of the area of a pixel
diagdmdt.m	Creates a bar diagram of mass estimates where the hydrological observations are plotted as reference
error_spectrum.m	Computes degree variances and degree RMS of a signal or error matrix
stats.m	Calculates the RMS, mean, minimal and maximal value of a given field
spherdist.m	Calculates the spherical distance between two points on a sphere

## Filter functions

dstrpngmtrx	Filters spherical harmonic coefficients with a decorrelated error filter (B. Devaraju)
gaussfilter.m	Computes the filter coefficients of an isotropic Gaussian filter, depending on the halfwidth radius
hannoniso.m	Computes the filter coefficients of an anisotropic Gaussian filter (B. Devaraju)
Wiener.m	Computes the filter coefficients of an isotropic, anisotropic scalar or anisotropic vector Wiener filter

### Data modification functions

coeff_remove.m	Removes the degree 0 and 1 coefficients from any given input
coeff_restore.m	Adds zeros as degree 0 and 1 coefficients to any given input
colomboQ.m	Orders a variance-covariance matrix, ordered in degree ordering, in Colombo/order-wise ordering (B. Devaraju)
cs2sc.m	Converts spherical harmonic coefficients in c\s format into the rectangular /s c\format (B. Devaraju)
sc2cs.m	Converts spherical harmonic coefficients in rectangular /s c\format into the c\s format (B. Devaraju)
grid2gmt.m	Transforms a coordinate grid into a format, which is readable by GMT
mat2vec	Transforms a matrix in c\s format with spherical harmonic coefficients in a Colombo/order-wise ordered column-vector
mssvr.m	Calculates the area-averaged mass change of a field in a certain catchment, depending on the catchment id
sh_sort.m	Arranges a vector with spherical harmonic coefficients in either c\s or /s c\format

### Signal- and error-propagation

gshscov.m	Propagates the covariance information of a spherical harmonic field to the spatial domain (B. Devaraju)
gshscovfn.m	Computes the covariance function in the spatial domain for a given point in space (B. Devaraju)
itc.m	Computes isotropic transfer coefficients of a selectable gravitational quantity
lovenr.m	Computes degree-dependant Love numbers
plm.m	Computes the fully normalized associated Legendre functions (N. Sneeuw)
synth_fld.m	Spherical harmonic synthesis function which computes a field of a selectable gravitational quantity
synth_ctch.m	The function computes the storage change of a certain catchment from spherical harmonic coefficients
spec2spat.m	Propagates an isotropic filter operator from the spectral to the spatial domain

### Regularization filter

mn_pwr.m	Computes the average logarithmic power of a selectable period of the CSR-4 coefficients
plfit.m kaulamatrix.m	This function computes the parameters of a power law Fits a power law into the signal degree variances of given spherical harmonic coefficients and arranges them as a diagonal weight matrix
reg_filt.m	Constrains the GRACE solutions with an estimated degree variance model

### Hydrological constraining functions

hydconst.m	Constrains the GRACE-solutions with hydrological observations
ctch_crd.m	Computes coordinates of the pixel centers of the data points with the catchment id

### Input and output data

Folder	Filename	Description
GLDAS	tws*.nc	GLDAS-data for different months
GRACE data	csr4matJul08.mat	Structure variable containing a modified CSR-4-GRACE-dataset with spherical harmonic coefficients and their errors (B. Devaraju)
	QJan.mat	Simulated and scaled full covariance matrix of the GRACE-data from January 2003
Hydrological data	hyddata.mat	Structure variable containing the hydrological data with precipitation and runoff values (B. Devaraju)
Position data	pos*.tar.gz	Position data of the GRACE satellites for different months
Regularization	regotpt.mat	Structure variable containing the regularized dataset of January 2003 with spherical harmonic coefficients, their full covariance matrix, variance components, weight matrices and the filter kernel
Hyd. Const.	hydconstotpt.mat	Structure variable containing the hydrological constrained dataset of January 2003 with spherical harmonic coefficients, their full covariance matrix, the normal matrix of hydrological observations, variance components, degree variances and RMS values